

The Pennsylvania State University

The Graduate School

Department of Chemistry

**Investigations of Phospholipid Membrane Properties Using An  
Artificial Cell Model for Exocytosis and Membrane Disruption**

A Thesis in

Chemistry

by

Daniel J. Eves

© 2007 Daniel J. Eves

Submitted in Partial Fulfillment  
of the Requirements  
for the Degree of

Doctor of Philosophy

December 2007

The thesis of Daniel J. Eves was reviewed and approved\* by the following:

Andrew G. Ewing  
Professor of Chemistry  
Professor of Neural and Behavioral Sciences  
J. Lloyd Huck Chair in Natural Science  
Thesis Advisor  
Chair of Committee

Christine D. Keating  
Associate Professor of Chemistry

Erin D. Sheets  
Assistant Professor of Chemistry

Ryan S. Clement  
Assistant Professor of Bioengineering

Ayusmen Sen  
Professor of Chemistry  
Head of the Department of Chemistry

\*Signatures are on file in the Graduate School

## ABSTRACT

Exocytosis is a fundamental cellular process that propagates neurochemical signals as well as delivers new lipid material to cellular membranes. Exocytosis is comprised of multiple stages, which include initial membrane fusion, fusion pore formation and membrane distention or incorporation. This study seeks to shed light on the later stages of exocytosis namely fusion pore expansion and full membrane incorporation. The introductory chapter seeks to supply a basic framework with which to interpret the experimental results presented in the subsequent chapters. The information covers the basic properties of biomembranes components, interactions and shape considerations consistent with specific interactions as well as a general explanation of the current knowledge about exocytosis and electrochemical means of measuring exocytosis.

Chapter 2 deals with a quantitative explanation of catechol release from an artificial model of exocytosis. Catechol release is measured by a carbon fiber electrode placed at the opening of the model, the electrode oxidizing the catechol molecules. The membrane-electrode interface in this model system is similar to a synapse, the liposome as the presynaptic terminal and the electrode acts as the postsynaptic side when it detects the released molecules. A mathematical model of the release from the system allows for predictions of electrode coulometric efficiency in exocytosis *in vitro* from a variety of cell types.

The third chapter investigates the role of lipid headgroups in exocytosis. Various headgroups are added to soy polar extract, the basis of the liposome model and the release characteristics for each lipid additive are determined and compared. This study

endeavors to understand the importance of lipid headgroup composition in the cell membrane from an exocytosis point of view. Also this study looks toward understanding microdomains in a purely lipidic sense, able to disregard the protein interactions that would be present in a cellular system.

To further characterize our lipid model system, in Chapter 4 the diameter of a lipid nanotube that connects the components of the liposome model is measured using steady state electrochemistry. In a steady state, the amount of material that reaches the electrode should be due to the amount diffusion through the nanotube, which allows for the calculation of the tube diameter. Additionally, the nanotube has been a fundamental part of the liposome model as it approximates the fusion pore. By measuring the diameter, a better understanding of the forces exerted upon the membrane can be gained.

Chapter 5 contains the fabrication of a new microelectrode array that can be used to add spatial resolution to the excellent temporal resolution afforded by amperometry. This electrode array allows for the identification of “hot zones” of exocytosis from a single cell. The characterization of the electrode shows the versatility of this method of detection.

In order to further understand membrane dynamics, Chapter 6 investigates the membrane disruption by antibacterial polymers. Based on the antibacterial agents used to kill *e-coli*, multiple polymers were synthesized to access their relative potency. Then the polymers were applied to the exterior of a giant unilamellar liposome to ascertain their effectiveness in rupturing the membrane. This study gives insight into the relationship between membrane rupture and antibacterial activity.

Chapter 7 outlines future directions in modeling exocytosis. This chapter includes preliminary data as well as suggested experiments.

**TABLE OF CONTENTS**

LIST OF FIGURES .....	xi
LIST OF TABLES .....	xiv
LIST OF EQUATIONS.....	xv
ACKNOWLEDGEMENTS .....	xvi
Chapter 1 Exocytosis, Lipids and Electrochemistry .....	1
1.1 Introduction .....	1
1.2 Exocytosis.....	1
1.3 Lipids.....	5
1.4 Artificial Liposome Cell Model of Exocytosis.....	7
1.5 Electrochemistry.....	11
1.5.1 Amperometry.....	12
1.5.2 Fast Scan Cyclic Voltammetry.....	14
1.5.3 Patch Amperometry.....	15
1.6 Goals of the Thesis.....	18
1.7 Literature Cited.....	20
Chapter 2 Amperometric Detection of Exocytosis in an Artificial Synapse.....	23
2.1 Introduction.....	23
2.2 Materials and Methods.....	25

2.2.1 Liposome-Lipid Nanotube Preparation.....	25
2.2.2 Fluorescence Microscopy.....	26
2.2.3 Amperometric Measurements.....	26
2.3 Results and Discussion.....	27
2.3.1 Quantitative Measurements of Exocytosis in Model Systems.....	27
2.3.2 Mass Transport in to and out of Artificial Synapses: A Simple Model Based on Coulometric Efficiency.....	33
2.3.3 Electrochemical Measurements during Distinct States of Exocytotic Release.....	36
2.3.4 Relevance of the Model to Electrochemical Measurements at Cells with Different Vesicle Sizes.....	42
2.3.5 Mass Transport in Small Places: Relevance to Transmission in the Synapse.....	45
2.4 Literature Cited .....	45
Chapter 3. Amperometric Detection of Exocytosis in an Artificial Synapse.....	47
3.1. Introduction.....	47
3.2. Materials and Methods.....	51
3.2.1. Liposome Preparation.....	52
3.2.2. Electrochemical Detection .....	54
3.2.3. Confocal Imaging of Liposomes.....	54
3.3. Results and Discussion.....	54
3.3.1. Increasing Phosphatidylserine.....	56
3.3.2. Increasing Phosphatidylcholine.....	57

3.3.3. Increasing Phosphatidylethanolamine.....	57
3.3.4. Increasing Phosphatidylinositol.....	59
3.4.5. Quantitative Comparison of the Effect of Lipid Additives on Release Transients.....	59
3.4. Summary of Lipid Additive's Effect on Exocytosis .....	63
3.5 Literature Cited .....	64

#### Chapter 4 Steady State Electrochemical Determination of a Lipid Nanotube

Diameter.....	66
4.1 Introduction.....	66
4.2 Materials and Methods.....	68
4.2.1 Liposome-Lipid Nanotube Preparation.....	68
4.2.2 Electrochemical Recording.....	69
4.2.3 Microscopy and Digital Video Recording.....	70
4.3 Results and Discussion.....	71
4.3.1 Initial Nanotube Measurements.....	71
4.3.2 Liposome Composition Changes.....	74
4.4 Conclusions about Lipid Nanotube Measurements.....	76
4.5 Literature Cited.....	76

#### Chapter 5 Fabrication and Characterization of Carbon Fiber Microelectrode

Arrays.....	78
5.1 Introduction.....	78
5.2 Materials and Methods.....	80

5.2.1 Chemicals .....	80
5.2.2 Fabrication of Carbon Fiber MEAs.....	81
5.2.3 Electrochemical Apparatus.....	82
5.2.4 Scanning Electron Microscopy .....	82
5.2.5 Finite-Element Simulations.....	82
5.3 Results and Discussion.....	83
5.3.1 Fabrication of Carbon Fiber MEAs .....	83
5.3.2 Scanning Electron Microscopy.....	84
5.3.3 Steady-State Voltammetric Response of the Two-Fiber MEAs .....	85
5.3.4 Finite-Element Simulation of Steady-State Limiting Current at a Two-Fiber MEA.....	88
5.3.5 Voltammetric Response of the Seven-Fiber MEAs.....	91
5.3.6 Flow-Cell Characterization of the Triple MEA.....	93
5.4 Summary for Carbon Fiber Multi Electrode Arrays.....	96
5. 5 Literature Cited.....	96
Chapter 6 Modeling Membrane Disruption by Pyridinium Polymers in Artificial Lipid Vesicle Systems.....	99
6.1 Introduction.....	99
6.2 Materials and Methods .....	101
6.2.1 Materials and Instrumentation.....	101
6.2.2 Synthesis of Pyridinium Polymers.....	101

6.2.3 Preparation of Surface Bound Liposomes and Polymer Injection.....	102
6.2.4 Antibacterial Testing.....	104
6.3 Results and Discussion.....	105
6.3.1 Synthesis of Pyridinium Polymer Library.....	105
6.3.2 Antibacterial Activity of Pyridinium Polymers.....	106
6.3.3 GUV Formation and Polymer Injection Protocol.....	107
6.3.4 Effect of Tail Length on the Time of Vesicle Rupture.....	108
6.3.5 Morphological Changes in GUV Membrane Structure.....	110
6.3.6 Effect of Polymer Molecular Weight on Vesicle Rupture.....	115
6.3.7 Effect of Intra-Vesicular Polyanion on Vesicle Rupture.....	116
6.4 Conclusions.....	117
6.5 Literature Cited.....	118
Chapter 7 Future Directions of Modeling Exocytosis.....	119
7.1 Introduction.....	119
7.2 Free Fusion.....	120
7.3 Cholesterol.....	121
7.4 Protein Additives.....	122
7.5 Changing Acyl Chain Composition.....	124
7.6 Conclusion.....	126
7.7 Works Cited.....	127

## LIST OF FIGURES

Figure 1.1. Illustration of the Four Stages of Exocytosis.....	3
Figure 1.2. Illustration of the SNARE Complex.....	4
Figure 1.3. Chemical Structure of a Phospholipid.....	5
Figure 1.4. Diagram of the Various Shapes of Lipids.....	7
Figure 1.5. Liposomes Connected by Lipid Nanotubes.....	8
Figure 1.6. Formation of the Liposome Model of Exocytosis.....	9
Figure 1.7. Basic Introduction to Amperometry.....	13
Figure 1.8. Example of Fast Scan Voltammetry.....	15
Figure 1.9. Explanation of Patch Clamp Amperometry.....	17
Figure 2.1. Formation and Release of a Vesicle in an Artificial Synapse.....	29
Figure 2.2. Fluorescence Images of Release in an Artificial Cell.....	31
Figure 2.3. Amperometric Data for Vesicle Fusion.....	32
Figure 2.4. Simple Coulometric Efficiency Model of Artificial Exocytosis.....	34
Figure 2.5. Coulometric Efficiency at a 33 $\mu\text{m}$ diameter Electrode.....	35
Figure 2.6. Schematic of the Distinct Stages of Artificial Exocytosis.....	37
Figure 2.7. Comparison of Coulometric Efficiency with 5 and 33 $\mu\text{m}$ Diameter Electrodes.....	38
Figure 3.1. Lipid Packing in a Fusion Pore Type High Curvature Membrane.....	53
Figure 3.2. A Schematic Illustration of the Formation of the Artificial Exocytosis Model.....	50
Figure 3.3. Overlays of Amperometric Peaks for Different Lipid Compositions.....	55

Figure 3.4. Plot of Amperometric Halfwidths vs. Vesicle Diameter for Different Lipid Compositions.....	58
Figure 3.5. Line Scan for Confocal Imaging to Determine Amount of Fluorophore.....	63
Figure 4.1. Experimental Setup for Steady State Electrochemical Measurement of a Lipid Nanotube.....	70
Figure 4.2. A Plot of the Measured Nanotube Diameter vs. Nanotube Length.....	73
Figure 4.3. A Plot of Nanotube Diameter vs. Nanotube Length for Varied Lipid Composition.....	75
Figure 5.1. A Schematic Drawing of Carbon Fiber Multi-electrode Arrays.....	78
Figure 5.2. Scanning Electron Microscopy of Carbon Fiber Multi-electrode Arrays.....	84
Figure 5.3. Steady-state Voltammetric Response of a Two-fiber Multi-electrode Array.....	85
Figure 5.4. Ratio of Steady-state Limiting Current for Two Electrode Array.....	90
Figure 5.5. Simulated Distribution of Steady-state Diffusive Flux for a Two Electrode Array.....	91
Figure 5.6. Steady-state Voltammetric Response of a Seven-fiber Electrode Array.....	92
Figure 5.7. Fast-scan Voltammetric Response of Seven-fiber Electrode Array.....	93
Figure 5.8. Schematic Depiction of Flow-cell Characterization of a Three-fiber Electrode Array.....	94
Figure 5.9. Amperometric Response for a Three-fiber Electrode Array in a Flow-cell.....	95

Figure 6.1. $^1\text{H}$ NMR spectrum of $\text{C}_3$ polymer.....	102
Figure 6.2. Giant Unilamellar Liposome Formation by Electroporation/Inflation Technique.....	104
Figure 6.3. Synthesis of Poly (4-vinyl-N-alkylpyridinium iodide) Polymers with Different Tail Lengths.....	106
Figure 6.4. Schematic of Direct Real-time Observation of Membrane-Polymer Interaction in Giant Unilamellar Vesicles.....	108
Figure 6.5. Differential Interference Contrast Snapshots of Membrane Disruption by $\text{C}_1$ Polymer.....	111
Figure 6.6. Differential Interference Contrast Snapshots of Membrane Disruption by $\text{C}_3$ Polymer .....	112
Figure 6.7. Morphological Changes Observed in the Vesicle Membrane Structure for $\text{C}_3$ and $\text{C}_5$ Polymers.....	114
Figure 7.1. A Plot of Vesicle Radius vs. Halfwidth for Control and Free Fusion Liposomes.....	121
Figure 7.2. Schematic of Shibire Form of Dynamin.....	124
Figure 7.3. Analysis of Two Acyl Chain Additives Compared with Soy Polar Extract.....	126

**LIST OF TABLES**

Table 2.1. Summary of Different Cells Types and the Expected Coulometric Efficiency for Amperometric Detection.....	43
Table 3.1. Percentage of Phospholipid Headgroups in Each Sample for Analysis.....	56
Table 5.1. Steady-State Limiting Current at a Two-Fiber Electrode Array as a Function of Inter-Electrode Spacing.....	88
Table 6.1. Antibacterial Activity of Synthesized Pyridinium Polymers Towards <i>E. coli</i> Bacteria.....	107
Table 6.2. Average Rupture Time and Number of Injections Needed to Completely Disrupt a Vesicle.....	109
Table 6.3. Average Rupture Time of Higher Molecular Weight Polymers.....	115
Table 6.4. Average Rupture Time for C <sub>1</sub> and C <sub>3</sub> Polymers on Vesicles Filled with Polyacrylic Acid.....	116

**LIST OF EQUATIONS**

Equation 2-1. Integrated Cottrell equation.....	39
Equation 2-2. Charge passed due to catechol in the membrane-electrode space.....	39
Equation 2-3. Concentration of catechol in the membrane-electrode space.....	40
Equation 2-4. Maximum charge passed during a release event.....	40
Equation 2-5. Percent coulometric efficiency.....	41
Equation 4-1 Fick's first law of diffusion.....	71
Equation 4-2 Adjusted Fick's first law for linear diffusion.....	71
Equation 4-3 Simplified Fick's first law for linear diffusion.....	72
Equation 4-4 Rearranged linear diffusion equation solving for radius.....	72
Equation 5-1 Steady State diffusion at a disk electrode surface.....	85
Equation 5-2 Steady State diffusion at a hemispherical electrode surface.....	86

## ACKNOWLEDGEMENTS

So many people have aided me in my journey that it will be difficult to mention them all. First and foremost I need to thank my Advisor, Andy Ewing. It has been truly wonderful to work in an environment where I can make my own mistakes but have someone there to cheer me on to my next success. Thank you to my Ph.D. Committee Erin Sheets, Chris Keating and Ryan Clement for useful suggestions in directing my research. I need to also thank Erin for allowing me to use her equipment while I pursued a promising but eventually disappointing project using fluorescence correlation spectroscopy.

It is also important for me to acknowledge all the members of the Ewing group both past and present who have give invaluable advice to me over the years. I can't do justice to them all but would like to mention a few. Thank you to Paula Powell, Tracy Paxon and Leslie Sombers for helping me get acclimatized to the Ewing group and making lab a pleasant place to work. Thank you to Nate Wittenberg for teaching me the ins and outs of liposomes and being a great research companion. Thank you to Edward "Junior" Phillip for helping me develop hidden talents. Also, thank you to Kelly Adams for her help in navigating the tricky world of lipid headgroup additives and department politics. I would also be remiss if I didn't thank Marc Maxson, who kept me busy trying to understand his fashion sense and his scientific queries. Thank you to Mike Kurczy for sticking with this whole education thing. A special thank you to Bo Zhang for his help in understanding electrochemistry and the English language.

I also need to thank my family for their support of me as I have been here in Pennsylvania. Thank you to my parents for being that constant reminder that there is

something waiting for me when I visit them. I appreciate the encouragement that they have given me and have always been there to give that extra bit of advice that got me on to the next stage of my education. Also thank you to my wife, Rosalyn for her support as I spent long hours away from home in pursuit of my research. I hope to reciprocate the favor as she continues her education. And thank you to my son Andrew for making coming home such a delight. Finally thanks to God for the wonders of this world and the pursuit of science to try and explain it all.

## **Chapter 1**

### **Exocytosis, Lipids and Electrochemistry**

#### **1.1 Introduction**

The processes of the brain have been of scientific interest for generations. Understanding the inner workings of the brain has presented a great challenge due to the fact that the brain consists of a complex network of cells. This complexity limits our ability to parse out the individual parts and stimuli involved in neurocommunication, an important part of the process by which the brain communicates with the rest of the body.

This chapter will cover some of the information necessary to understand the basic processes of neurocommunication and how those processes have come to be understood. First, an explanation of exocytosis and the cellular machinery involved in this process. Next, a section covering the role of lipids in exocytosis and ways in which liposomes can be used to mimic the exocytotic processes. Finally, an overview of the use of electrochemistry as it has been employed in elucidating key aspects of exocytosis in single cell analysis.

#### **1.2 Exocytosis**

Exocytosis is a principle part of neurocommunication and it is regulated by the speed in which vesicles fuse to the cellular membrane. There are many contributing factors to exocytosis, including SNARE [SNAP receptor, where SNAP is soluble N-

ethylmaleimide-sensitive factor-attachment protein] complex and lipid composition of fusing vesicles.<sup>1-5</sup> In order to investigate this vital process, it becomes necessary to try to simplify measurements by reducing the system to its component parts. By doing this it is possible to determine the effect of one part of the system in relation to another and to determine how it is best to regulate the system to help improve the overall effect.

Exocytosis has been identified to have four distinct stages. First a vesicle travels from the golgi apparatus in the cell to the plasma membrane, once the vesicle comes in contact with the membrane (Figure 1.1 A), it is said to have “docked.” Once a vesicle has docked, the release process is initiated by the lipid membranes starting to intertwine themselves. When the two lipid monolayers closest to each other join and are seamlessly connected, the second stage (Figure 1.1 B), “hemifusion,” is said to have taken place. From the hemifusion state, the lipids continue to mix until a small hole or “fusion pore” forms in the plasma membrane and the inner contents of the vesicle and the extracellular area are brought into contact (Figure 1.1 C). After fusion pore formation, the vesicle membrane is then incorporated or distended into the plasma membrane, sending its contents into the extracellular area or synapse. This last step is referred to as complete fusion (Figure 1.1 D). The first two steps of exocytosis are almost completely regulated by proteins on the two lipid bilayer surfaces but the last two are regulated by lipids.<sup>6</sup>

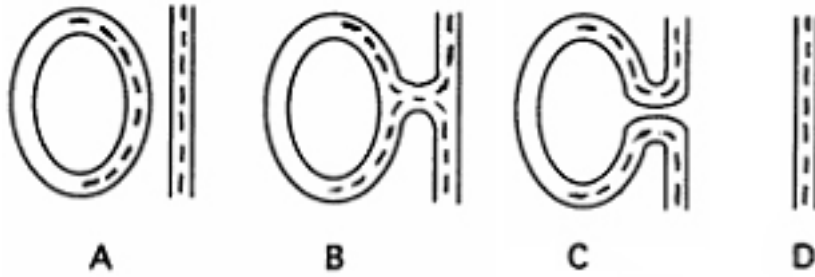


**Figure 1.1** Illustration of the four stages of exocytosis. (A) docking: where the vesicle is brought into contact with the plasma membrane (B) hemifusion: intermixing of lipid in the adjacent monolayers (C) fusion pore: a small hole forms in between the vesicle and the extracellular matrix and (D) complete fusion: incorporation of the vesicle into the membrane. Adapted from reference 6.<sup>6</sup>

In the process of vesicle docking, the SNARE complex plays a major role. The SNARE complex is made up of three distinct proteins, (synaptobrevin, SNAP 25 and syntaxin) that entwine together to tether the vesicle to the plasma membrane surface (Figure 1.2).<sup>7</sup> These proteins bring the lipid bilayer into close proximity with each other to allow the intermixing of the distal layers. Furthermore, it is thought by some<sup>7</sup> that once the vesicle has docked and hemifusion has occurred, the SNARE complex can pull open a fusion pore to allow the vesicular contents into the extracellular area or synapse.

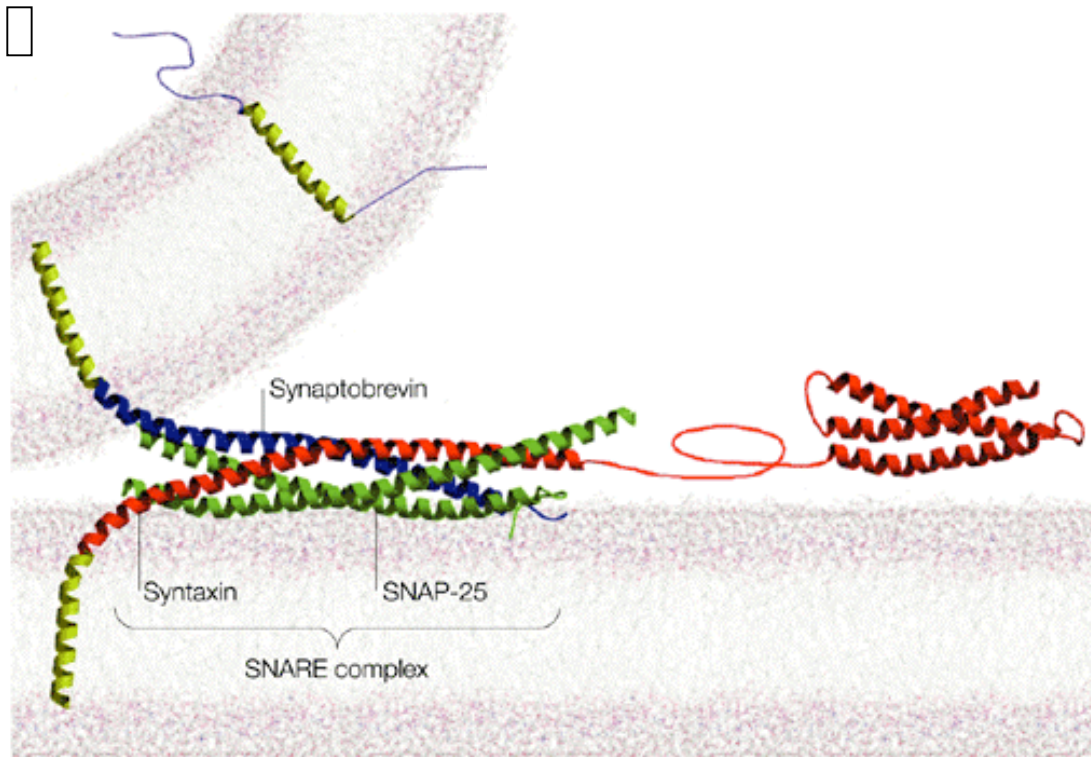


**Figure 1.2** Illustration of the SNARE complex. Synaptobrevin is attached to the vesicle while SNAP-25 and syntaxin are membrane bound proteins. When the vesicle comes into close proximity of plasma membrane, the three proteins intertwine to bring the vesicle closer to the membrane surface. This structure was obtained from X-ray crystallography data. (Adapted from reference 7)

In summary, exocytosis plays a major role in cellular communication. Cells package neurotransmitters into vesicles that are released at the plasma membrane upon stimulus. There are four stages of exocytosis: docking, hemifusion, fusion pore formation and complete fusion. After fusion, neurotransmitters cross the synapse and bind to related receptors on the post synaptic terminal, thus propagating chemical signals. In order to investigate this vital process, it becomes necessary to try and simplify the system to its component parts. By doing this it is possible to determine the effect of one part in relation to another and to determine how it is best to regulate the system to help improve the overall effect.

### 1.3 Lipids

Lipids can play a role in the exocytosis process in many different ways.

Phospholipids, those lipids with a phosphate based headgroup, have been shown to act as secondary messengers in signaling cascades for cellular functions. Phospholipids are comprised of a glycerol backbone and have a range of head and tail groups that differentiate them from each other (Figure 1.3).

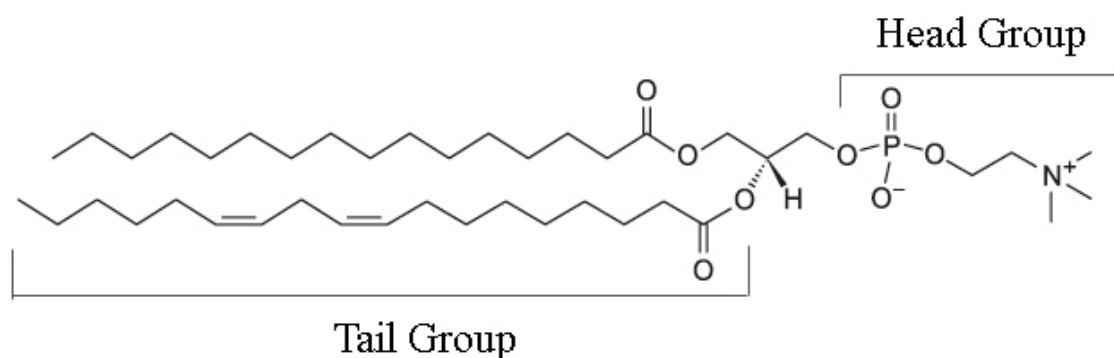


**Figure 1.3** An example of a phospholipid noting the head group and the tail group.

The head groups for phospholipids are varied; they are comprised of choline, ethanolamine, glycerol, hydrogen, inositol and serine. Each of these head groups have unique properties that add to the overall bilayers structure and function. Tail groups are fatty acid chains of varying lengths and saturation levels. These acyl chains range from 3 to 26 carbons and can have as many as six double bonds in each chain. Head groups and tail groups combine in various ways to give three different geometries for the lipid (Figure 1.4). When the size of the head and tail groups are relatively the same, a lipid is classified as cylindrical. These lipids, usually with choline, glycerol, inositol and serine head groups, prefer to assemble in a bilayer conformation and are equally likely to be found in both leaflets of a bilayer. When the headgroup is smaller than the acyl chains, the lipid is said to have a conical shape and favors a micellular conformation.<sup>8</sup> These

lipids tend to reside in the inner leaflets of vesicles due to the increased curvature of the bilayer in small structures. Conical lipids have an ethanolamine or hydrogen headgroup. The third geometrical shape, when the tail groups are smaller than the headgroup, is called an inverted cone or hexagonal II lipid.<sup>8</sup> This lipid shape also manifests itself when one of the two fatty acid chains is absent. These lipids are called lyso lipids and favor the outer bilayer of a vesicle.

These three lipid shapes are found in most membranes in differing concentrations, the amounts found are based on specific membrane function. By changing the composition of the membrane, it is possible to attract different types of proteins to the surface and therefore change the functionality of the membrane. Also the overall curvature of the membrane is affected by the amount of certain shaped lipids. An increase in conical lipids will increase the positive curvature of a membrane, while an influx in lyso lipids increases the negative curvature (Figure 1.4B).<sup>9</sup> In this way the lipids play a role in the structure-function relationship of the membrane.

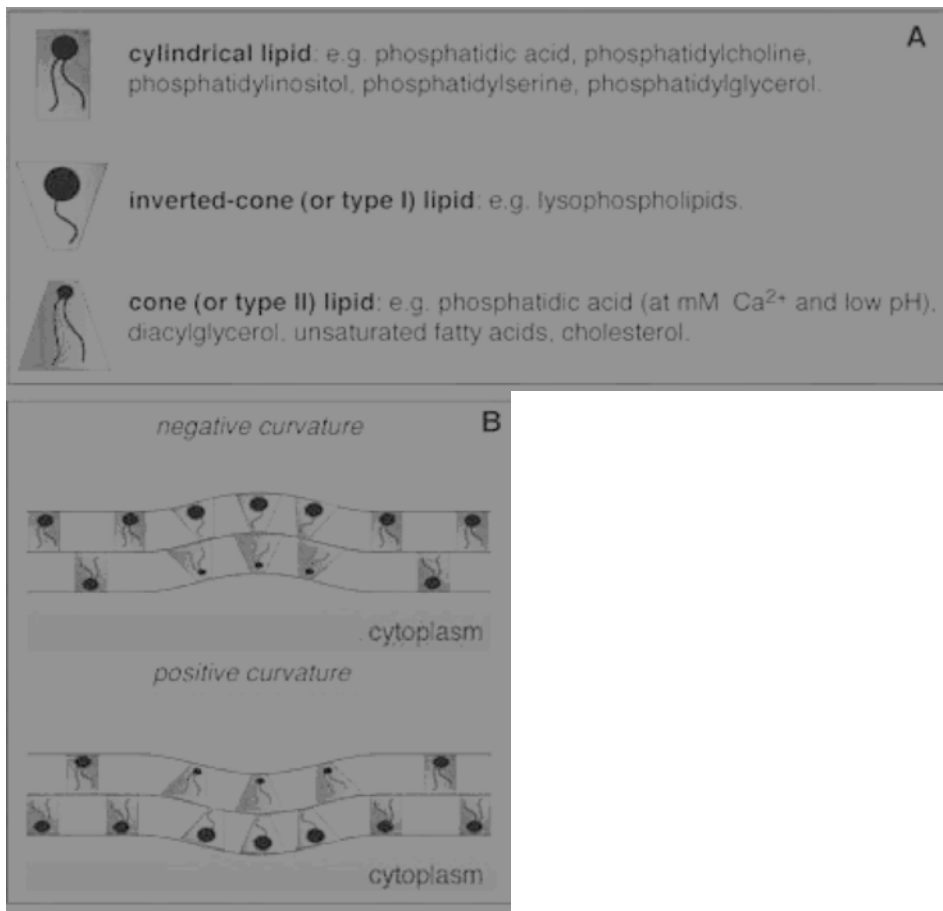


**Figure 1.4** Diagram of the various shapes of lipids. (A) three geometric shapes of lipids and examples. (B) An illustration of how lipids shape effects overall membrane curvature. (Adapted from ref 8)

### 1.4 Artificial Liposome Cell Model of Exocytosis

In order to more fully explore the forces that regulate exocytosis, a lipid model system has been devised to explore the role of membranes in neurotransmitter release. This system utilizes liposomes to mimic exocytosis. A liposome is a spherical configuration for a lipid bilayer that can approximate the environment inside a cell or cellular compartment.<sup>10</sup> Zare's laboratory and later Orwar's laboratory pioneered the use of liposomes as microcontainers for reactions on the nanoscale.<sup>11-14</sup> To introduce reagents

into the liposomes a micropipette system can be used with electroporation of the membrane. Proof of injection was verified optically by injecting fluorescein into a giant unilamellar liposome.<sup>15</sup> These liposomes have been manipulated into forming networks of vesicles all connected by lipid nanotubes (Figure 1.5).<sup>12, 13</sup>

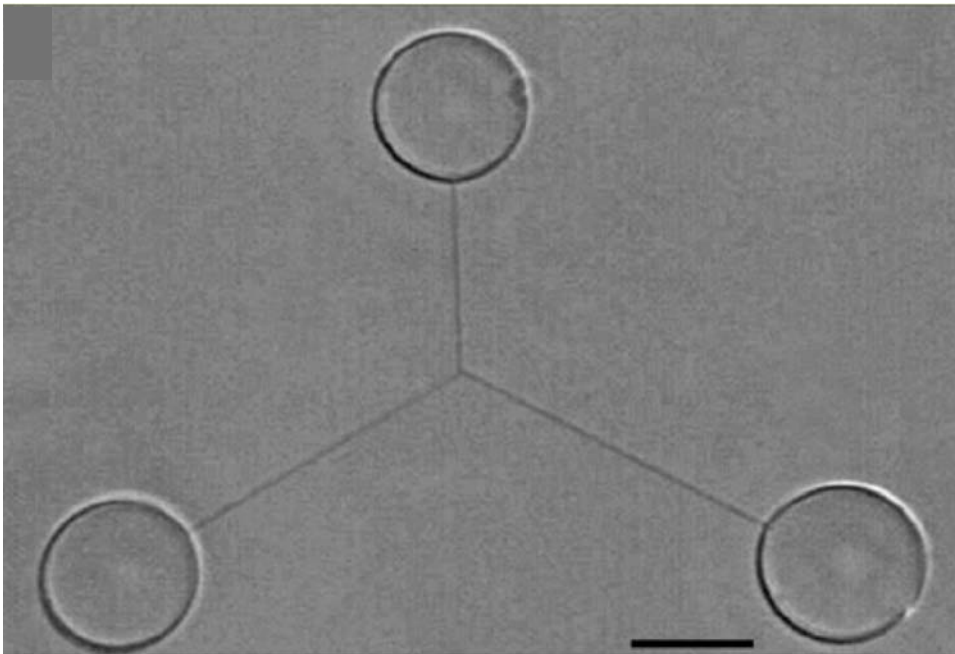


**Figure 1.5** Liposomes connected by lipid nanotubes. Scale bar is 10  $\mu\text{m}$ . (Adapted from reference 13)

A liposome model for exocytosis has been devised that examines the final stages of vesicle fusion. This model mimics the transition from fusion pore formation to full fusion (Fig. 1.6F-I). Release of molecules loaded into the vesicle can be monitored by amperometry and fusion kinetics can be extrapolated from these measurements. In the liposome model, all protein is removed to eliminate its role in the fusion event. Fusion proteins have been identified to play a central role in fusion pore formation; thus, formation of the fusion pore is not measured here.

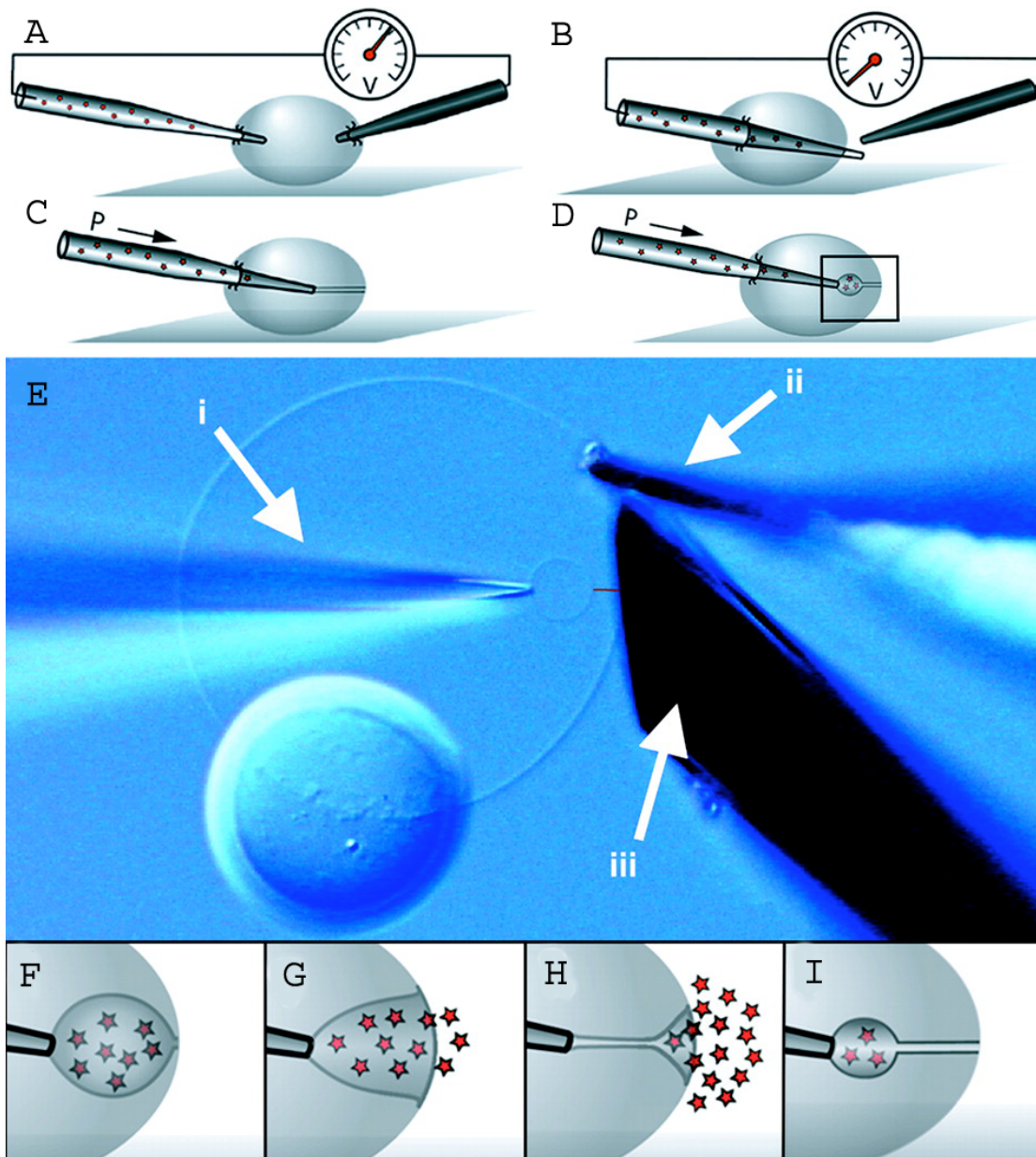


**Figure 1.6** (A) A potential is applied between the injection pipette and counter electrode which allows the pipette to enter into the liposome. (B) The pipette continues through the liposome and exits on the other side, a voltage was applied for this exit as well. (C) The pipette is drawn back inside of the liposome and part of the lipid bilayer adheres to the tip and forms a nanotube. (D) The pressure exuding from the pipette causes a vesicle to form on the end. (E) an experimental view of an artificial cell, the smaller liposome (vesicle) is attached to the pipette (i) on end and to the larger liposome by a nanotube. The nanotube location is marked by black line since it is not visible by microscopy. Also pictured are the counter electrode for electroporation (ii) and the detection electrode beveled at  $45^\circ$  (iii). (F-I) Illustration of constant flow from injection pipette. As the vesicle grows the nanotube shortens and then spontaneous fusion takes place. After full fusion a vesicle forms again and continues the process. (Adapted from reference 16)

In order to create the liposome model for exocytosis, a unilamellar liposome attached to a multilamellar liposome is used. The multilamellar liposome acts as a source of lipid for the unilamellar liposome when it is manipulated. Manipulation of the liposomal system including inflation, nanotube extrusion and deflation is accomplished with a pulled glass pipette having a tip diameter that is less than a micrometer. A potential is applied across the liposome to disrupt the membrane and allow the pipette to enter into the liposome (Fig. 1.6A). To mimic the latter stage of exocytosis, the pipette is pushed through the opposite side of the liposome (Fig. 1.6B) and then drawn back inside. The lipid material of the bilayer adheres to the tip and continues inside the liposome in the form of a lipid nanotube (Fig. 1.6C). Inflation of an inner liposome at the end of the nanotube (Fig. 1.6D&E) eventually leads to an unstable pore-like structure between the inner and outer liposomes. This resembles a cell about to undergo the final stage of exocytosis and opening results in release into the outer solution. The larger liposome acts as a plasma membrane to which the smaller liposome (vesicle) fuses (Fig. 1.6F-H). Easily oxidized substances that are released by this process are then detected at an electrode placed right outside the liposome. A useful aspect of this system is that the distention repeats almost indefinitely (Fig. 1.6F-I). Thus it is straightforward to vary experimental conditions such as vesicle size, temperature, lipid composition with consistent controls without the variability inherent in biological systems.<sup>16</sup>

Data from the liposome model has been compared with that obtained from PC12 cells. The liposome model exhibited similar amperometric peak attributes. The pre-spike foot was visible and though the liposomes were larger in size than the PC12 cell vesicles, the release was proportional allowing direct comparison. The added advantage of the

liposome model is that it allows analysis of neurotransmitters that are released via the nanotube prior to full release. In this way, the lipid nanotube at its shortest length approximates the fusion pore that occurs at the beginning of exocytosis in cells. With the absence of fusion proteins, it has been shown that the energetics inherent in lipid structures are sufficient to drive the opening of the fusion pore for full exocytosis.<sup>16</sup> Cans et al. were able to show that the absence of proteins does not hinder the expansion of a fusion pore in exocytosis.<sup>16</sup> In fact, for vesicles of like sizes, the time required for full fusion is faster in the liposome model than that for vesicle opening in live cells. This leads to speculation that proteins involved in creating the fusion pore might actually limit opening during the final stage of exocytosis.

### **1.5 Electrochemistry**

In order to remove some of this complexity inherent in the brain, single cells are frequently studied as a model system.<sup>17-21</sup> When single cells are examined, the environment can be closely controlled and direct correlations between treatment with a pharmacological agent and its effect can be determined. This closely controlled environment facilitates the study of important cellular processes, like exocytosis, which can be monitored by electrochemistry.

Electrochemical methods can be used to identify and/or quantify neurotransmitters as they are released from single vesicles. The electrochemical techniques frequently used for this purpose include amperometry, fast scan cyclic voltammetry and amperometry combined with the electrophysiological technique, patch clamp. In amperometry, electroactive species are oxidized at constant potential thus

generating a current that is measured by a potentiostat.<sup>17, 18</sup> Fast scan cyclic voltammetry can be used to provide information about the identity of the molecule in the solution by examining characteristic oxidation-reduction peaks.<sup>19</sup> Another important technique for measuring exocytosis is patch clamp. Here a small glass capillary adheres to the cellular membrane to monitor changes in capacitance. Patch clamp has been coupled with amperometry to correlate the amount of release with capacitance.<sup>3, 20, 21</sup>

### 1.5.1 Amperometry

Amperometry is well suited to measuring secretion from cells because of its ability to quantify release from vesicles on a millisecond time scale<sup>19</sup> (Fig. 1.7). In amperometry, a small electrode is placed near the cell and held at a potential where oxidation is diffusion limited. Stimulant is applied with a small pipette (Fig. 1.7A) resulting in current transients for each exocytosis event. The general oxidation reaction for catechol is shown in figure 1.7B and a typical current-time trace is figure 1.7C. The number of molecules detected from a release event can be calculated using Faraday's law (Fig. 1.7D). Experimental determination of charge allows calculation of the number of moles of molecules detected by rearranging the Faraday equation.

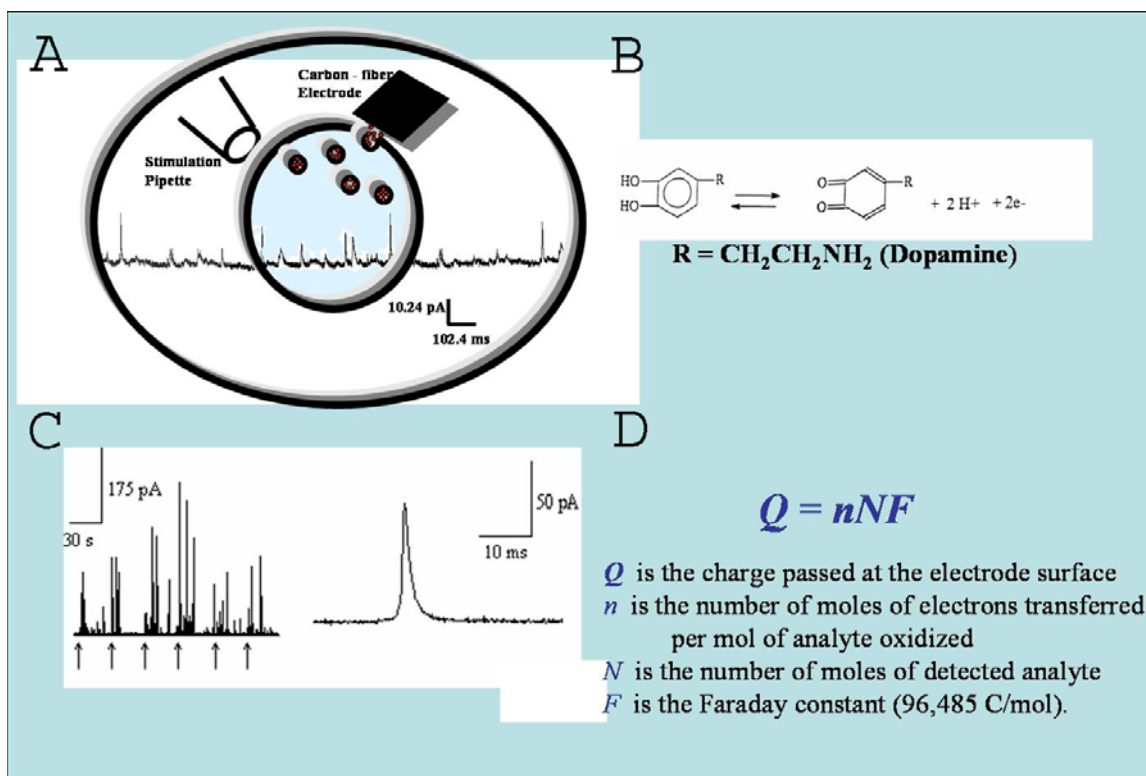


**Figure 1.7** Basic introduction to amperometry. (A) Foreground image is the typical setup for amperometry for single cell. The exocytosis is stimulated by a pipette containing a stimulant and the release is monitored by a carbon fiber electrode. The background image shows typical amperometric data. (B) Shows the oxidation reaction for catecholamines. The catecholamine is oxidized to the ortho-quinone form, losing two electrons. (C) Left spectra shows a series of stimulations, denoted by the arrows, and the electrochemical responses detected after each stimulation. The right hand spectra show a single amperometric spike. (D) Faraday's equation, which is used to determine the amount of material released during exocytosis.

For amperometry in biological systems, a carbon fiber electrode is used. In most cases the electrode is constructed in house, this construction is carried out by aspirating a carbon fiber into a glass capillary, heating and pulling the capillary to a small tip around the fiber, sealing the fiber in the capillary with epoxy, cutting the electrode and beveling at a 45° angle. The electrode is typically tested by a single sweep in dopamine and used for analysis.<sup>17</sup> The electrode is positioned near a cell where exuded neurotransmitter can

be detected (Fig. 1.7A). When the electrode is placed flush against the cell there is a small amount of space, about 300 nm, between the cell and the electrode.<sup>26, 27</sup>

The characteristic shape of amperometric peaks aids in understanding the various aspects of the exocytosis event. The peak shape is dictated by the flow of electroactive agents to the surface of the electrode. Since the electrode is held at a constant potential, (700 mV vs. SSCE), the oxidation of molecules released generates a current that is measured by a potentiostat.<sup>17, 18</sup> This current vs. time trace can be analyzed to provide information about exocytosis (Fig. 1.7C). Specifically, the half-width of the peak (full width at half maximum) measures the duration of the exocytotic event. The rise time, typically taken as the time it takes to go from ten percent to ninety percent of the peak height, is considered equivalent to the time it takes the fusion pore to open. Thus, the basic amperometric measurement provides data on the amount of transmitter released, the duration of each event, and the rate of opening of the fusion pore.

### **1.5.2 Fast Scan Cyclic Voltammetry**

Cyclic voltammetry has also been adopted in order to measure release from single cells. In contrast to amperometry where the signal is proportional to the total mass of messenger released, in cyclic voltammetry the signal is proportional to the local concentration of electroactive molecules and this technique has been shown to have nanomolar detection limits. The advent of microelectrodes has led to the ability to scan at much higher scan rates than with conventional electrodes. High scan rates provide a means to obtain voltammograms in 10 ms or less thus providing the time resolution necessary to monitor exocytosis events. To detect catecholamines, the voltage sweep

typically begins at -0.4 V (vs. a sodium-saturated calomel reference electrode), ramps to +1.1 V and then back to -0.4 V. A typical scan rate is in the range of 800 V/s.<sup>19</sup> The rapid sweep rate creates a high background current and therefore what is typically observed is a very small signal in a large background, which must be subtracted to quantify the signal (Fig. 1.8).<sup>22</sup>

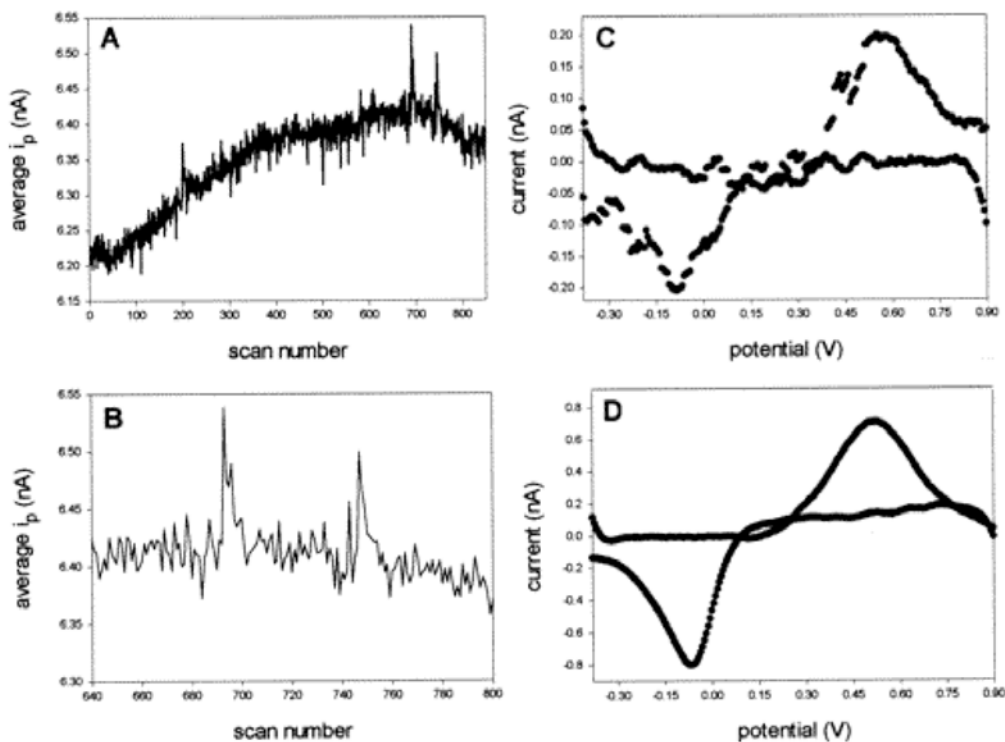


**Figure 1.8** (A) Average current within a 60-mV window of the peak oxidation potential of dopamine. Individual current spikes represent faradaic current. (B) Enlargement of the region between scans 600 and 800 showing two current transients used to generate voltammograms. (C) Background-subtracted voltammogram generated by subtracting the average signal of scans 687-690 from the signal of scan 693. (D) Background-subtracted voltammograms of a standard 25  $\mu\text{M}$  dopamine solution. (Adapted from reference 22)

### 1.5.3 Patch Amperometry

Amperometry and patch clamp techniques have been combined to provide a powerful method for the study of exocytosis in single cells called patch amperometry

(Fig. 1.9). The patch clamp technique records capacitance of the cell as a function of time. Developed by Erwin Neher and Bert Sakmann it can be used to measure changes in the capacitance and thus area of the cell plasma membrane and can therefore be used to examine both the opening of ion channels and changes in total membrane area such as those related to vesicle fusion and recapture.<sup>23</sup> During exocytosis, the capacitance of the cell increases because the membrane of fusing vesicles becomes incorporated in the plasma membrane increasing the surface area and thus the membrane capacitance. This is measured by placing a glass capillary with a small opening, typically about 1  $\mu\text{m}$  on the membrane, forming a seal with greater than gigaohm resistance. Loss of membrane area during endocytosis leads to a decrease in membrane capacitance and this can be measured with the patch technique as well.<sup>23</sup>

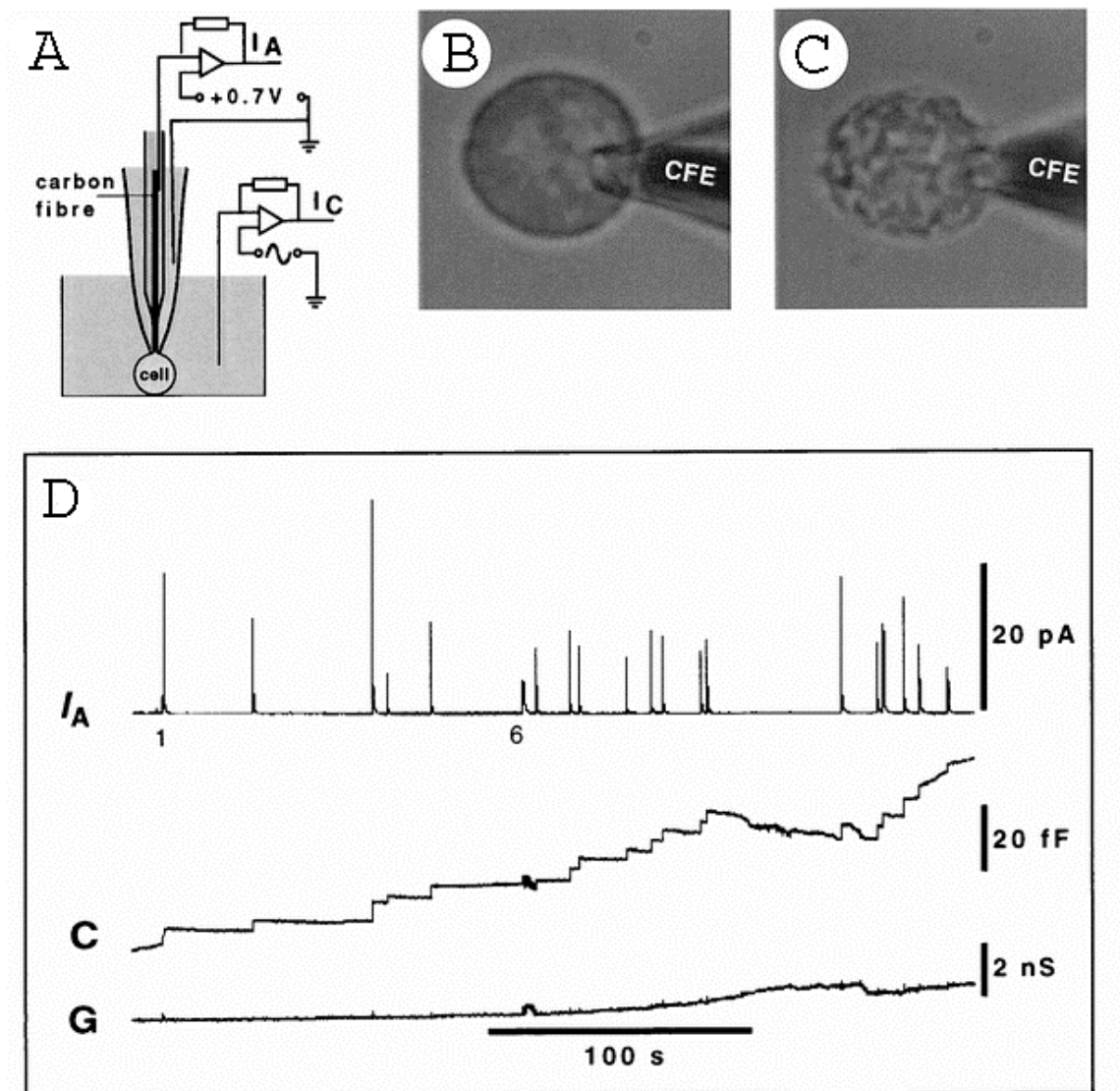


**Figure 1.9** (A) Electrical configuration of a patch amperometry electrode/pipette.  $I_A$  is the amperometric current, (0.7 V vs. a Ag/AgCl reference electrode) and  $I_C$  is the sine wave current used to measure capacitance. (B) A pipette attached to a chromaffin cell before the experiment. (C) A chromaffin cell after an experiment. (D) The top current trace ( $I_A$ ) corresponds to the amperometric data. The middle trace  $C$  is the capacitance trace. The bottom trace  $G$  is the conductance trace. (Adapted from reference 20)

Combining the patch clamp technique with amperometry provides a method to correlate the changes in membrane area with transmitter release measured at a microelectrode. This is done by placing a carbon fiber inside the patch pipette. Thus capacitance and amperometric data are simultaneously recorded in the same location.

This has an added advantage in that the patch pipette affords a more controlled environment for the patched portion of the membrane. Variation of the pipette solution can be used to apply specific conditions to the section of patched membrane. Single cells have been analyzed separately by patch clamp and amperometry, but by placing a carbon fiber electrode in the patch pipette it makes it possible to study the pore opening and closing at the same area of membrane. Amperometric spikes can be correlated to capacitance so the amount of messenger released is synchronized to the opening of the pore, and by use of the area change upon vesicular release and simultaneous quantification of transmitter the vesicular concentration of neurotransmitter can be estimated.<sup>20, 24</sup> Patch amperometry has also been used to measure the cytoplasmic concentration of messenger molecules.<sup>25</sup>

### **1.6 Goals of the Thesis**

Exocytosis is an important cellular process that is fundamental to cell-to-cell communication in the brain. Lipids play a vital role in exocytosis both in basic function and in variation of the process with different lipid structures, thus they are important in understanding how vesicle fusion is regulated. The SNARE hypothesis is the best explanation of how exocytosis is initiated that is currently available. Thus far most of the research has been devoted to the role that proteins play in exocytosis but this only nominally considers how lipids aid in neurotransmitter release. Much of the work presented in this thesis is aimed at developing a better understanding the role of lipids in neurocommunication and eventually of how lipids and proteins work together to facilitate it. The following is a summary of the work presented in the chapters of this thesis.

In chapter 2, an investigation of amperometric detection in the liposome model of exocytosis takes place. The geometry of the electrode next to the liposome is defined to better explain amperometric data. It is shown that even when an electrode is adjacent to a liposome there is a space in between electrode and lipid surface. An investigation of liposome size vs. electrode size shows how to improve coulometric efficiency of the electrode so that 100% of a neurotransmitter can be detected.

Chapter 3 explores the role that lipid headgroups play in catechol release from the liposome model of exocytosis. Addition of phosphatidylcholine causes an increase in release time for liposomes. This same trend is seen for phosphatidylinositol and phosphatidylserine. The increase in release time can be attributed to an increase in bilayer forming headgroups. Also, an increase in phosphatidylethanolamine, a micelle forming lipid, causes a decrease in release time.

Chapter 4 looks to define the diameter of the lipid nanotube that forms between the two liposomes in the exocytosis model. Steady state amperometry is employed to measure catechol diffusion out of the nanotube, which can be used to determine the nanotube size. Two different lipid compositions are also investigated to see if headgroup composition can affect nanotube diameter. The changes in lipid composition did not show a significant difference in nanotube size but the overall finding suggests that the nanotube diameter is smaller than initially measured.

Chapter 5 details a new electrode that allows for spatial resolution of exocytosis from cells. This electrode is actually an array of multiple electrodes that are constructed next to each other to allow for differentiation of amperometric signal propagating from a cell. This electrode array is characterized for use in further experiments. This new

electrode will give more information about the release of neurotransmitters in single cell experiments.

Chapter 6 shows how liposomes can be used as cell membrane mimics for determining membrane disruption by antibacterial agents. Various antibacterial agents are applied to the surface of a liposome to determine the mode of entrance into the cell. Antibacterial polymers were synthesized and applied as well, to determine which monomer type was most effective in rupturing the membrane. It was shown that increased antibacterial activity does not increase the ability of the polymer to disrupt the liposome membrane.

Finally, Chapter 7 discusses future applications of the liposome model and how it can be used to understand fundamental aspects of exocytosis. Some examples are the incorporation of proteins into the liposome as well as investigating acyl chain concentrations and how they affect exocytosis. Electrochemistry is one of many techniques used to study biological systems and is well suited based on its sensitivity and its temporal resolution. Armed with this information, it is possible to reach a better understanding of how lipids can regulate exocytosis.

### 1. 7 Literature Cited

- (1) Burgoyne, R. D.; Fisher, R. J.; Graham, M. E.; Haynes, L. P.; Morgan, A. *Biochem. Soc. Trans.* **2001**, *29*, 467–472.
- (2) Osborne, S. L.; Wen, P. J.; Meunier, F. A. *Journal of Neurochemistry* **2006**, *98*, 336-342.
- (3) Tabares, L.; Lindau, M.; Alvarez de Toledo, G. *Biochem. Soc. Trans.* **2003**, *31*, 837–841.
- (4) Graham, M. E.; Washbourne, P.; Wilson, M. C.; Burgoyne, R. D. *Ann NY Acad Sci* **2002**, *971*, 210-221.

- (5) Wang, C.-T.; Grishanin, R.; Earles, C. A.; Chang, P. Y.; Martin, T. F. J.; Chapman, E. R.; Jackson, M. B. *Science* **2001**, *294*, 1111-1115.
- (6) Chernomordik, L.; Chanturiya, A.; Green, J.; Zimmerberg, J. *Biophys. J.* **1995**, *69*, 922-929.
- (7) Chapman, E. R. *Nature Reviews Molecular Cell Biology* **2002**, *3*, 498.
- (8) Chernomordik, L.; Kozlov, M. M.; Zimmerberg, J. *Journal of Membrane Biology* **1995**, *146*, 1-17.
- (9) Corda, D.; Hidalgo Carcedo, C.; Bonazzi, M.; Luini, A.; Spano, S. *Cellular and Molecular Life Sciences* **2002**, *59*, 1819-1832.
- (10) Chiu, D. T.; Wilson, C. F.; Karlsson, A.; Danielsson, A.; Lundqvist, A.; Stromberg, A.; Ryttsen, F.; Davidson, M.; Nordholm, S.; Orwar, O.; Zare, R. N. *Chemical Physics* **1999**, *247*, 133-139.
- (11) Moscho, A.; Orwar, O.; Chiu, D. T.; Modi, B. P.; Zare, R. N. *PNAS* **1996**, *93*, 11443-11447.
- (12) Karlsson, A.; Karlsson, R.; Karlsson, M.; Cans, A.-S.; Stromberg, A.; Ryttsen, F.; Orwar, O. *Nature* **2001**, *409*, 150-152.
- (13) Karlsson, A.; Karlsson, M.; Karlsson, R.; Sott, K.; Lundqvist, A.; Tokarz, M.; Orwar, O. *Anal. Chem.* **2003**, *75*, 2529-2537.
- (14) Davidson, M.; Karlsson, M.; Sinclair, J.; Sott, K.; Orwar, O. *J. Am. Chem. Soc.* **2003**, *125*, 374-378.
- (15) Karlsson, M.; Nolkranz, K.; Davidson, M. J.; Strömberg, A.; Ryttsén, F.; Åkerman, B.; Orwar, O. *Anal. Chem.* **2000**, *72*, 5857-5862.
- (16) Cans, A.-S.; Wittenberg, N.; Karlsson, R.; Sombers, L.; Karlsson, M.; Orwar, O.; Ewing, A. *PNAS* **2003**, *100*, 400-404.
- (17) Wightman, R.; Jankowski, J.; Kennedy, R.; Kawagoe, K.; Schroeder, T.; Leszczyszyn, D.; Near, J.; Diliberto, E., Jr; Viveros, O. *PNAS* **1991**, *88*, 10754-10758.
- (18) Finnegan, J. M.; Pihel, K.; Cahill, P. S.; Huang, L.; Zerby, S. E.; Ewing, A. G.; Kennedy, R. T.; Wightman, R. M. *Journal of Neurochemistry* **1996**, *66*, 1914-1923.
- (19) Travis, E. R.; Wightman, R. M. *Annual Review of Biophysics and Biomolecular Structure* **1998**, *27*, 77-103.
- (20) Albillos, A.; Dernick, G.; Horstmann, H.; Almers, W.; de Toledo, G. A.; Lindau, M. *Nature* **1997**, *389*, 509.
- (21) Alés, E.; Tabares, L.; Poyato, J. M.; Valero, V.; Lindau, M.; Alvarez de Toledo, G. *Nature Cell Biology* **1999**, *1*, 40 - 44.
- (22) Kozminski, K. D.; Gutman, D. A.; Davila, V.; Sulzer, D.; Ewing, A. G. *Anal. Chem.* **1998**, *70*, 3123-3130.
- (23) Sakmann, B.; Neher, E. *Annual Review of Physiology* **1984**, *46*, 455-472.
- (24) Gong, L.-W.; Hafez, I.; Alvarez de Toledo, G.; Lindau, M. *J. Neurosci.* **2003**, *23*, 7917-7921.
- (25) Mosharov, E. V.; Gong, L.-W.; Khanna, B.; Sulzer, D.; Lindau, M. *J. Neurosci.* **2003**, *23*, 5835-5845.
- (26) Anderson, B. B.; Chen, G.; Gutman, D. A.; Ewing, A. G. *Journal of Neuroscience Methods* **1999**, *88*, 153.

- (27) Cans, A.-S.; Wittenberg, N.; Eves, D.; Karlsson, R.; Karlsson, A.; Orwar, O.; Ewing, A. *Anal. Chem.* **2003**, *75*, 4168-4175.

## Chapter 2

### Amperometric Detection of Exocytosis in an Artificial Synapse

#### 2.1 Introduction

In neurons and neuroendocrine cells intracellular compartments called vesicles contain neurotransmitters or neuropeptides and these transmitters are released to the extracellular space via exocytosis. Exocytosis begins with the fusion of a transmitter containing vesicle with the plasma membrane of a cell to form a fusion pore or lipid nanotube. This is followed by expansion of the fusion pore and transmitter release while the vesicle membrane is integrated into the plasma membrane. Upon their release to the extracellular space, neurotransmitters are thought to diffuse across the synaptic cleft (a distance of ~20 nm) where they subsequently bind to postsynaptic receptors or escape from the confined synapse to the larger extracellular space. Exocytosis at model cell systems has been characterized with a variety of techniques including amperometry,<sup>1</sup> voltammetry,<sup>2</sup> patch clamp methods,<sup>3,4</sup> fluorescence,<sup>5</sup> and evanescent field fluorescence microscopy.<sup>6-8</sup>

Amperometry has been widely used in the study of cellular secretion because of the high temporal resolution offered, as well as the presence of easily oxidizable neurotransmitters in neurons and neuroendocrine cells. Wightman et al. showed that individual amperometric current transients correspond to the oxidation of the contents of individual secretory vesicles.<sup>1</sup> Amperometric measurements rely on placing an ultrasmall electrode in extremely close proximity to the cell surface (a geometry that might be

considered an “artificial synapse”), and the assumption is made that quantitative oxidation of released transmitter occurs at the electrode surface. The cell membrane-electrode distance also affects the current transient associated with single-vesicle release.<sup>9</sup>

Computer simulations and models of amperometric detection of exocytosis events have treated the release as originating from a point source with mass transport occurring primarily by diffusion.<sup>9</sup> Although diffusional effects arising from differences in spacing between the electrode and the cell membrane have been characterized for relatively large distances, there has been little attention to the size of the vesicle relative to the electrode, except for a few theoretical treatments by Anderson et al.<sup>10,11</sup> The assumption of quantitative oxidation appears completely valid for cases in which the average vesicle dimensions are orders of magnitude smaller than those of the electrode and vesicle fusion is not in close proximity to the electrode edge. However, this is not necessarily accurate when release is measured from vesicles with volumetric dimensions approaching the volume of the membrane-electrode space.

An important issue in these measurements is the volume of the space between the membrane and the electrode. When the vesicle diameter is nearly the same as that for the electrode, there will not be enough volume between the cell and the electrode, thereby forcing solution out of the membrane-electrode space. In addition, understanding the dynamics of transmitter escaping the membrane-electrode space provides an effective model of what is now known to occur *in vivo* where dopamine and serotonin have been shown to escape the synapse following stimulated release.<sup>12-14</sup>

An artificial system based on liposomes and lipid nanotubes that can be manipulated to undergo exocytosis-like behavior has been developed.<sup>15</sup> This liposome-based system is

advantageous because it provides an easily controlled system to electrochemically and optically quantify release and to measure dynamics. In this chapter, experiments are presented to characterize the amperometric response observed for release of catechol during artificial exocytosis. Amperometry at electrodes of 5- and 33- $\mu\text{m}$  diameter has been compared to determine the effect of electrode size on coulometric efficiency as vesicle diameter is varied in the micrometer range. These data provide a framework to evaluate the quantitative ability of amperometric experiments to measure exocytosis from different size vesicles and a model for quantification of the response observed for larger vesicles. In addition, the model suggests that the rate of opening of the vesicle during exocytosis regulates, in part, the coulometric efficiency and therefore the magnitude of the amperometric response observed for large vesicles. We also present the hypothesis that liquid flow is a significant driving force for mass transport in these measurement paradigms and that this is likely to be significant in the operation of real synapses.

## **2.2 Materials and Methods**

### **2.2.1 Liposome-Lipid Nanotube Preparation**

Surface-immobilized, unilamellar liposomes and nanotube networks were prepared from soybean lecithin as described previously.<sup>16</sup> Briefly, a small glass micropipet is inserted into the unilamellar liposome assisted by transiently disrupting the membrane using an electric field.<sup>17</sup> Lipid adhesion to the tip during withdrawal results in a lipid tube that has dimensions up to tens of micrometers in length and 10-300 nm in

diameter. For fluorescence measurements, fluorescein sodium salt (Sigma, St. Louis, MO) solution (5  $\mu$ M) was loaded in the micropipette. For amperometric measurements, 1 mM catechol (Sigma) in phosphate buffer (5 mM Trizma Base, 30 mM  $K_3PO_4$ , 30 mM  $KH_2PO_4$ , 1 mM  $MgSO_4$ , 0.5 mM EDTA adjusted to pH 7.4 with  $H_2SO_4$ ) was placed in the vesicles via the microinjection pipette as vesicles were formed.

### **2.2.2 Fluorescence Microscopy**

Fluorescence was monitored with a Sony Exwave HAD CCD camera (Sony Medical Systems, Park Ridge, NJ) or a Sony DFW-SX900 camera with VideoAgent software by MIS (Franklin Park, IL) on an Olympus IX-70 DIC microscope (Olympus America, Inc., Melville, NY) and was collected with Studio DV software (Pinnacle Systems, Inc., Mountain View CA) on a PC at 30- or 133-ms intervals with the HAD and DFW-SX900 cameras, respectively.

### **2.2.3 Amperometric Measurements**

Carbon fibers were sealed in pulled glass capillaries with epoxy (Epoxy Technology, Billerica, MA). After beveling on a micropipet beveler (model BV-10, Sutter Instrument Co, Novato, CA) at 85 or 45 deg, testing in 0.1 mM catechol, electrodes were placed against the artificial cell with a micromanipulator (MP-85 Huxley wall-type micromanipulator on a MT-70-9 micromanipulator stand, Sutter) and current was monitored at 0.70 V versus a Ag/AgCl reference electrode with an Ensmann Instruments EI-400 potentiostat (filter frequency, 1 kHz). Data were collected at 20 kHz

with a Digidata model 1322A interface and recorded with Axoscope 8.1 software (Axon Instruments, Foster City, CA).

## **2.3 Results and Discussion**

Membrane fusion during exocytosis takes place in several distinct stages beginning with formation of a fusion pore and ending with the final full incorporation of the vesicle membrane into the cell plasma membrane.<sup>18</sup> Between these stages, the vesicle membrane itself must change its basic geometry from a sphere to a nearly planar disk going through several distinct geometrical shape changes. The physiological result of these events is the expulsion of transmitter contained in the vesicle into the extracellular space. If this space is the connection between two nerve cells, then this release could be the basis for synaptic communication.

### **2.3.1 Quantitative Measurements of Exocytosis in Model Systems**

Methods to monitor exocytosis involve measurements in the extremely small space between an electrode and the membrane and require detailed characterization to understand the abilities and pitfalls of the technique for different vesicle sizes. Figure 2.1 presents a schematic of the liposomal system used to mimic vesicular release. First, a small glass pipette is inserted into a surface-immobilized liposome using a microinjection technique.<sup>17</sup> The pipette is then pushed to the membrane on the opposite side and is then pushed through the membrane, exiting the liposome again using the microinjection technique.<sup>15</sup> A lipid nanotube connecting the pipette to the outer membrane is formed

when the pipette is pulled back into the center of the liposome. Liquid flow into the lipid nanotube results in formation of an expanding vesicle (Figure 2.1A). As this vesicle grows, the nanotube shrinks, eventually reaching a critical length where expansion of the nanotube and vesicle opening becomes spontaneous (Figure 2.1B-D). The nanotube is continually connected to the pipette tip; thus, fluid flow into the nanotube results in repeated vesicle formation and release of material contained in these vesicles as shown in Figure 2.1C. In these experiments, the pipette is loaded with catechol as the artificial neurotransmitter. An electrode placed at the site of release is used to dynamically monitor catechol ejected into the extraliposomal space, as shown in Figure 2.1. The insets in Figure 2.1 show traces of the amperometric current expected for each stage of vesicle opening.

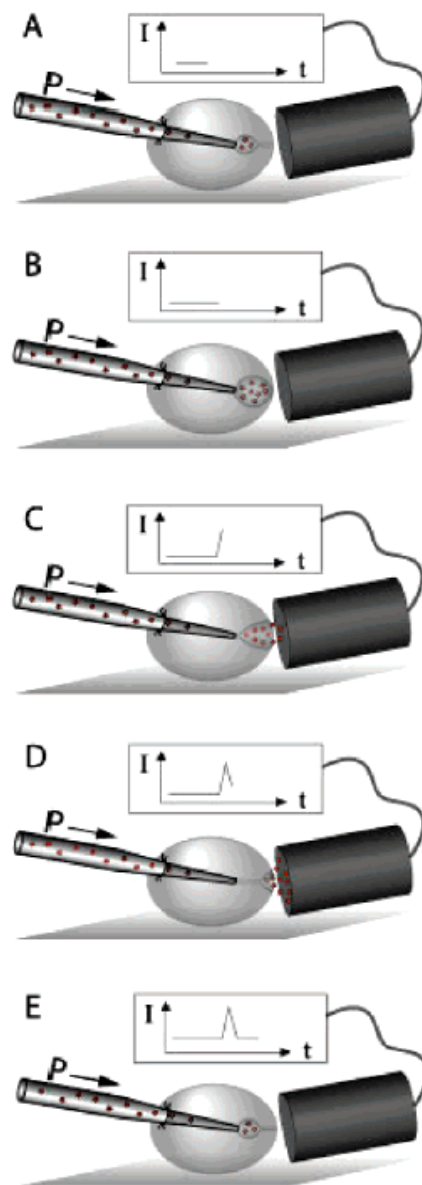


**Figure 2.1.** Formation and release of vesicles in the system to amperometrically measure release at an artificial synapse. The micropipette was inserted into and through a surface-immobilized liposome and pulled back to the interior to form a nanotube connection between the pipette tip and the wall of the liposome. Pressure from the pipette forms and expands an inner vesicle with 1 mM catechol (or 5  $\mu$ M fluorescein) solution (A, B) until spontaneous opening of the vesicle in an event resembling the final stage of exocytosis (C, D). Continued pressure leads to formation of consecutive vesicles (E). A carbon fiber electrode placed at the point of the nanotube exit/release site is used to oxidize released catechol. Each frame has a hypothetical current vs. time trace for the amperometric response to release at each stage of the exocytosis process. Artwork by Ann-Sofie Cans.

As the vesicle membrane is incorporated into the cell membrane, transmitter is forced out of the vesicle under pressure-based flow. Immediately after release, the transmitter can diffuse from the site of release as shown in Figure 2.2 (left side). In this image, all the vesicles have been loaded via the injection pipette with fluorescein and monitored with fluorescence microscopy. A fluorescent spherical vesicle is observed immediately prior to release (top left). Following the initial expansion of the nanotube, the vesicle undergoes several stages of deformation and the transmitter is released by flow and diffusion into the space outside the liposome. Released transmitter appears to diffuse away from the site of release and dilute with a hemispherical geometry. This hemispherical profile of mass transport changes dramatically, as observed in Figure 2.2 (right side), when an electrode is placed at the site of release. In this case, a 33- $\mu\text{m}$  diameter electrode has been used and it effectively blocks material transport in the axial direction. Instead, the material has to move radially in the confined space defined on one side by the membrane area and on the other side by the electrode area. Mass transport in this system is dependent on the size of the vesicle, the rate at which it opens (i.e., flow velocity profile), the size of the electrode, the height of the membrane-electrode gap, diffusion coefficient of the electroactive species, and several physical parameters such as viscosity and temperature.

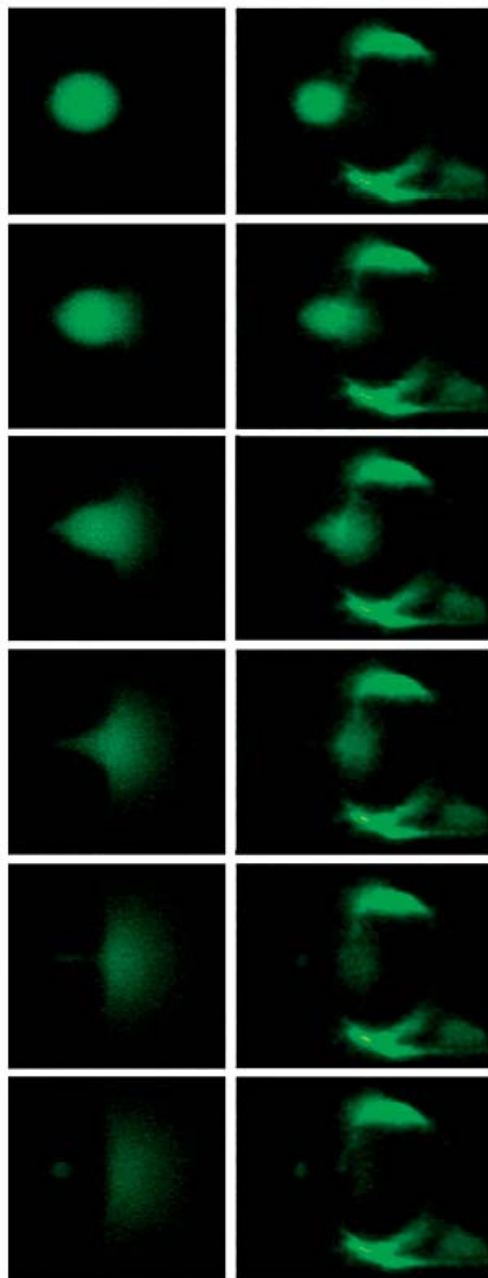


**Figure 2.2.** Two series of fluorescence images tracking exocytosis of vesicles filled with 5  $\mu\text{M}$  fluorescein without (left side) and with (right side) a beveled 33- $\mu\text{m}$  carbon fiber electrode. The electrode is observed to the right as the glass frame of the electrode has impurities that fluoresce. The vesicles on the left reach a diameter of 18.4  $\mu\text{m}$  before fusing, and those on the right reach a diameter of 10.5  $\mu\text{m}$ . As smaller vesicles undergo exocytosis faster than larger ones, the time between frames beginning at the top is 60 ms for those on the left and 30 ms between frames for those on the right with the electrode present. Artwork by Ann-Sofie Cans.

We measured release of vesicles having varied diameters in the artificial cell system with 5- and 33- $\mu\text{m}$  carbon fiber electrodes. Figure 2.3 examines the number of moles of catechol detected, the amplitude of the amperometric current, and the half-width of the oxidative current transient. As expected, the area of the oxidation peak increases with vesicle size (Figure 2.3A). However, the peak area is larger for the 33- $\mu\text{m}$  electrode than for the 5- $\mu\text{m}$  electrode, and the rate of the change in area with vesicle size is larger for the 33- $\mu\text{m}$  electrode. It appears the larger electrode surface results in a greater efficiency of catechol oxidation. The fact that catechol is not completely oxidized suggests that a great deal of the released catechol escapes the gap between the membrane and the electrode and this is modeled further below. The amplitude of the signal also behaves in a similar manner (Figure 2.3B), although it is approximately linear with vesicle radius over the larger range of vesicle sizes used here.

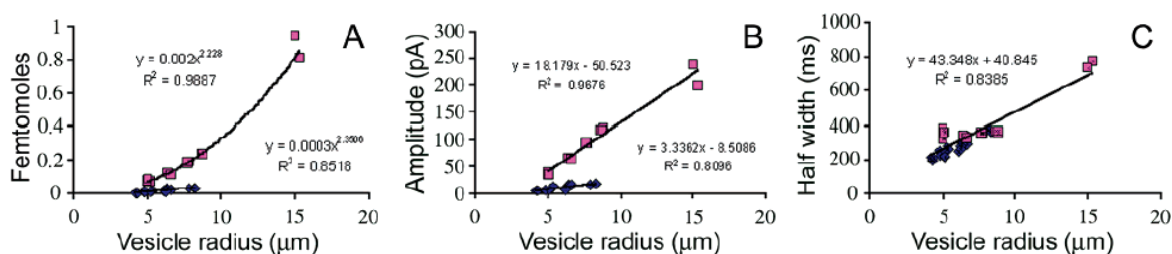


**Figure 2.3.** Amperometric data for fusion of vesicles of varying size at beveled 5- ( $\blacklozenge$ ) and 33- $\mu\text{m}$  ( $\blacksquare$ ) electrodes: (A) the amount of catechol observed at each electrode, (B) the amplitude of each current transient, and (C) the half-width of each transient vs the radius of vesicles undergoing exocytosis. Each data set has been curve fit to observe the trend in the data as indicated. Data collected by Ann-Sofie Cans.

The half-width of the peaks represents the time it takes for release to occur and for mass transport of catechol (or transmitter) to the electrode surface. This parameter does not change when 33- versus 5- $\mu\text{m}$  electrodes are used, although the half-width does

increase with vesicle size. As we suggested in our earlier work,<sup>15</sup> it appears that the dynamics of measured release are dependent on the rate of vesicle expansion for the dimensions used and not the electrode size. Although the time of amperometric events is invariant with electrode size, the differences in magnitude of the number of molecules oxidized and the current are important. When the vesicle diameter approaches that of the electrode used for measurement, oxidation of released transmitter is not complete and quantification of the signal can no longer be simply carried out using Faraday's law. This might also have implications for understanding release of transmitter in and subsequent escape or transport of the transmitter from real synapses, which can be modeled with this system as well (vide infra).

### **2.3.2 Mass Transport in to and out of Artificial Synapses: A Simple Model Based on Coulometric Efficiency**

To understand the events occurring following transmitter release into the gap between the membrane and the electrode, a simple model can be examined (Figure 2.4). In this model, we begin with the hypothesis that the space between the membrane and electrode has a cylindrical geometry and that the ratio of this volume to the vesicle volume prior to release determines the efficiency of the oxidation of released transmitter. Thus, if the volume of the space is larger than that of the vesicle and the height of the gap is sufficiently short that a released species can diffuse to the electrode during the time it is trapped in the confined geometry, then 100% coulometric efficiency is expected. In this model, coulometric efficiency is predicted simply as the ratio of the volume of the membrane-electrode space over the volume of the vesicle. If the vesicle volume is

smaller than the volume of the space, the coulometric efficiency is 100%. If the volume of the vesicle is greater than the volume of the space, then the efficiency is less than 100%. This is, of course, a simplistic model and it assumes that the site of release is the center of the electrode, that both the electrode and membrane are rigid immediately following release, and that diffusion out of the membrane-electrode space is negligible.

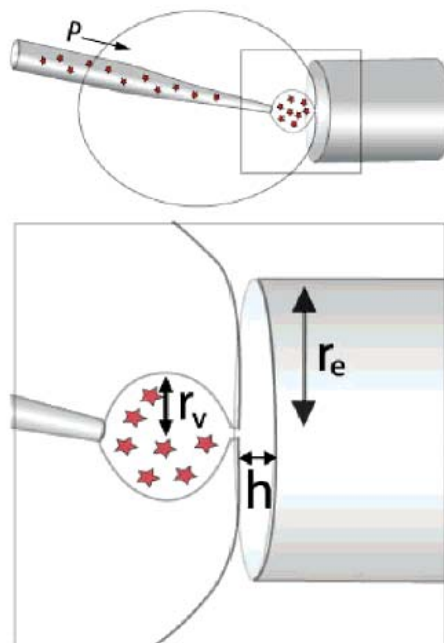


**Figure 2.4.** Simple model of coulometric efficiency for artificial exocytosis. This first-stage model assumes that the efficiency of oxidation for material released is simply the ratio of the membrane-electrode space (calculated as  $\pi r_e^2 h$ ) over the volume of the vesicle ( $4\pi r_v^3/3$ ). This assumes that all the catechol that is present in the membrane-electrode space after exocytosis will be oxidized, but also that only catechol in the solution that fits in this volume will be oxidized. Artwork by Ann-Sofie Cans.

The coulometric efficiency for one set of experimental data has been evaluated by comparing the amount of catechol oxidized at the electrode surface to the amount of catechol in the vesicle. This is plotted in Figure 2.5 and overlaid with the theoretical efficiency expected for a 33- $\mu\text{m}$  electrode. The best fit for the theoretical plot is obtained with a membrane-electrode space of 300 nm. These data are interesting in several

respects. First, it is clear from the fitted curve that a 33- $\mu\text{m}$  electrode used to measure release from a 5- $\mu\text{m}$ -radius vesicle will have an oxidation efficiency that is  $\sim 47\%$ . Thus, the majority of the catechol is escaping the space undetected. Second, the height of the fluid trapped between a membrane and a solid object (the electrode is physically placed on the membrane) appears to be on the order of hundreds of nanometers. Third, transport in this space can be compared to that across a synapse *in vivo*, and thus, the system can be used to model the efficiency of transmitters finding receptors in a synapse and also to model the escape of transmitter from the synapse as discussed with *in vivo* models.<sup>12,14</sup>

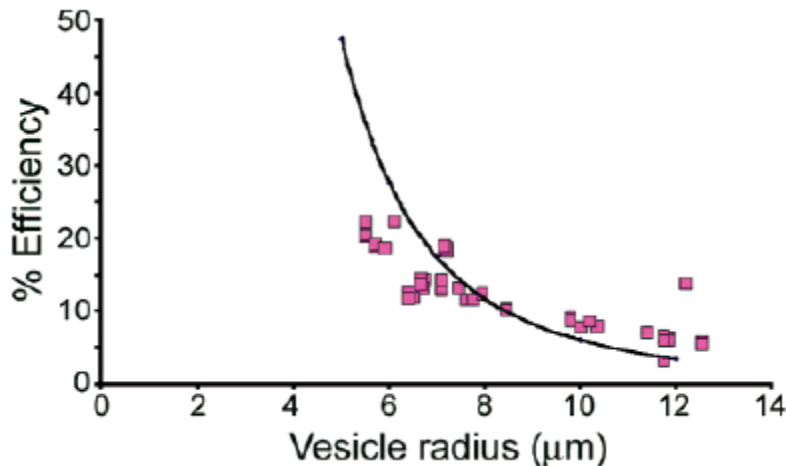


**Figure 2.5.** Coulometric efficiency for one data set obtained with a beveled 33- $\mu\text{m}$  electrode for release measured from a range of vesicle sizes ( $\blacksquare$ ). This is compared to the theoretical coulometric efficiency calculated from the model in Figure 2.4 (line). Data collected by Ann-Sofie Cans.(ref?)

The model presented in Figure 2.4 provides a framework for understanding that transmitter molecules in vesicles with a larger volume than the membrane-electrode space will not be quantitatively detected. However, this model does not provide a close fit to the data shown in Figure 2.5. There are several possible reasons for this. As the vesicle diameter approaches and then becomes larger than that of the electrode, some released transmitter never flows directly past the electrode surface, and thus at

large vesicle diameters, coulometric efficiency will decrease beyond that predicted. In addition, as shown in Figure 2.2, expanding vesicles open in stages and therefore mass transport of transmitter to the electrode needs to be considered for each of these stages.

### **2.3.3 Electrochemical Measurements during Distinct States of Exocytotic Release**

Distinct stages of vesicle expansion occur during full fusion over a finite time that is dependent on the vesicle size (see Figure 2.3C). Thus, a more comprehensive model has been developed to consider vesicle fusion geometry and the effect on the amperometric response. The model is shown in Figure 2.6 as four distinct stages and can be correlated to the images in Figure 2.2. Prior to release in the artificial system, the vesicle is expanding and the lipid nanotube is fully constricted (Figure 2.6A and top of Figure 2.2). At the first stage of expansion, the nanotube has reached a short unstable neck and begins to dilate (Figure 2.6B; this is not clearly observed in Figure 2.2). This is followed in the second stage by a structure that is between a spherical vesicle and a cone (Figure 2.6C and second and third images in Figure 2.2). The vesicle then undergoes a transition to where the membrane is bending outward and at this third stage it looks like a cone or frustum (Figure 2.6D and fourth image in Figure 2.2). Finally, the membrane is fully incorporated into the outer liposome or cell membrane and closes in on itself to leave a nanotube connected to the pipette (Figure 2.6E and fifth and sixth images in Figure 2.2). This presents a multistage view of the release of transmitter during exocytosis during which amperometric detection will have different boundary conditions.

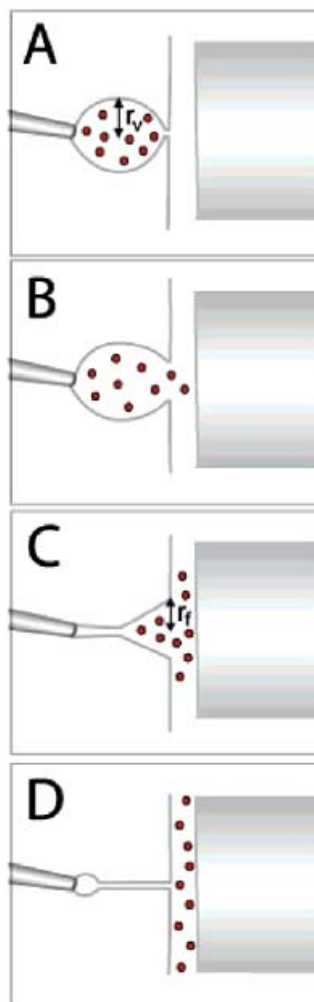


**Figure 2.6.** A more complete model of the release process during exocytosis based on the observations in Figure 2.2. This model assumes that as the vesicle opens, it has a transitory period where mass transport of catechol to the electrode is via diffusion from a frustum with opening  $r_f$  defined the value of  $r_v$  (approximation based on Figure 2.2). Catechol diffusing to the electrode is oxidized. After exocytosis is complete, the membrane- electrode space is filled with solution from the inside of the vesicle and catechol present continues to be oxidized as in the thin-layer representation of Figure 2.4. Artwork by Ann-Sofie Cans

The efficiency of catechol oxidation or “capture” for a set of experiments comparing 5- and 33- $\mu\text{m}$  electrodes to examine release from vesicles of 3.4-9.4- $\mu\text{m}$  radius is plotted in Figure 2.7. The capture rate varied from 9 to 1.7% for the 5- $\mu\text{m}$ -diameter electrode, and the efficiency for capture by the 33- $\mu\text{m}$ -diameter electrode varied from 53 to 23%. It is tempting to consider the final stage of the nanotube opening as the

point at which release truly begins; however, it is clear in Figure 2.2 that transmitter is escaping during the middle stages of expansion and this is significant for developing models of collection efficiency at the electrode and for capture by receptors or transporters in vivo. We have modeled these data by assuming that oxidation occurs during an intermediate stage and that mass transport to the electrode is via diffusion. This occurs when the frustum is present as the vesicle opens. Following full opening of the vesicle, complete oxidation of the remaining unoxidized catechol trapped in the membrane-electrode space occurs. The total charge predicted from this model is plotted in Figure 2.7 for both the 5- and 33- $\mu\text{m}$  electrodes as the ratio over the charge expected if all the catechol in the vesicle is oxidized. The best fit of this theoretical treatment to the data is found when the membrane-electrode space again is 300 nm for both the 5- and the 33- $\mu\text{m}$  electrode.

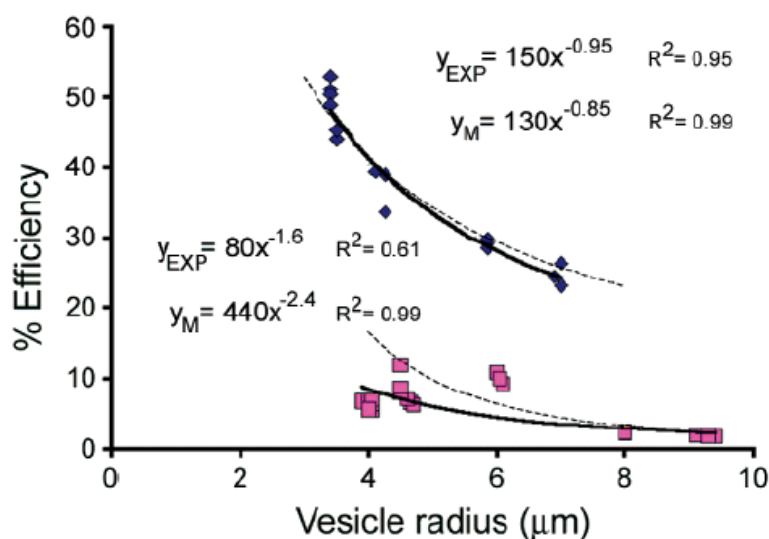


**Figure 2.7.** Coulometric efficiencies for a data set obtained with a beveled 33- $\mu\text{m}$  electrode ( $\blacklozenge$ ) compared to data obtained with a 5- $\mu\text{m}$  electrode ( $\blacksquare$ ) for release measured from a range of vesicle sizes. This is compared to the theoretical coulometric efficiencies for these electrode dimensions calculated with the conditions outlined in Figure 6 and with the model discussed in the text (dashed lines). These are compared to each set of experimental data, which are shown with best-fit equations (thick lines). The equations for all lines, and their correlation coefficients, are given with the symbols  $y_{\text{exp}}$  for

experimental data sets and  $y_m$  for the modeled efficiencies with that for the 5- $\mu\text{m}$  electrode to the left and that for the 33- $\mu\text{m}$  electrode to the right. The experimental best-fit equations are used for the analysis in Table 2.1. Data Collected by Ann-Sofie Cans.

The model used to fit the data in Figure 2.7 has been developed by assuming that oxidation first occurs from material diffusing from the volume of the frustum formed as an intermediate step in the release process followed by complete oxidation of the remaining unoxidized catechol trapped in the membrane-electrode space after full fusion. During the time the frustum is opened (calculated as twice the half-width for each vesicle), the charge passed is estimated from the integrated Cottrell equation

$$Q_{frustum} = \frac{2nFAD^{1/2}C^*t^{1/2}}{\pi^{1/2}} \quad \text{Equation 2-1}$$

where  $n$  is the number of electrons transferred in the electrochemical reaction,  $F$  is Faraday's constant,  $A$  is the effective area of the electrode (the smaller area defined by the frustum or the electrode is used),  $D$  is the diffusion coefficient ( $6 \times 10^{-6} \text{ cm}^2/\text{s}$ ),  $C^*$  is the concentration of catechol in the vesicle, and  $t$  is the time for vesicle release to occur and is taken to be twice the peak half-width. The peak half-width is obtained from the best-fit linear equation for the data in Figure 2.3C. Although the response is not truly linear, it appears so at these larger vesicle sizes and this appears to be a good approximation.

Following full exocytosis, the charge for oxidation of transmitter in the membrane-electrode space is calculated for quantitative oxidation of the catechol in the membrane-electrode space using the equation

$$Q_{space} = nFC_e^2h \quad \text{Equation 2-2}$$

where  $r_e$  is the average radius of the beveled electrode (3.1  $\mu\text{m}$  for the 5- $\mu\text{m}$  carbon fiber electrodes and 20.6  $\mu\text{m}$  for the 33- $\mu\text{m}$  carbon fiber electrodes, each beveled to 45 deg)

and  $h$  is the distance across the space. During this second stage, after full fusion is complete, the concentration of the remaining catechol in the membrane-electrode space is estimated based on the ratio of the volume of this space to that of the vesicle. This is adjusted by subtracting the moles of catechol oxidized during the first stage with the equation

$$C' = \frac{[C^*(V_v + V_{flow}) - 2AD^{1/2}C^*t^{1/2}/\pi^{1/2}]}{V_v + V_{flow}} \quad \text{Equation 2-3}$$

where  $V_v$  is the volume of the vesicle and  $V_{flow}$  is the volume of flow from the pipette during the release event. Remembering that  $N = Q/nF$  from Faraday's law, and from the integrated Cottrell equation,  $Q = 2nFAD^{1/2}C^*t^{1/2}/\pi^{1/2}$ , the number of moles used during the diffusion-limited oxidation of catechol in the frustum stage is given by  $N = 2AD^{1/2}C^*t^{1/2}/\pi^{1/2}$ . In this calculation, the volume of the vesicle is  $4\pi r_v^3/3$ , where  $r_v$  is the radius of the vesicle. Furthermore, the flow during the event is calculated by dividing the vesicle volume by the time between events (the time to fill a vesicle) to get the flow rate (in  $\text{cm}^3/\text{s}$ ) and then multiplying the flow rate times twice the half-width of the amperometric event.

The coulometric charge expected for complete oxidation of the total number of moles of catechol in the vesicle prior to release is calculated with the equation

$$Q_{\max} = nFC^*(V_v + V_{flow}) \quad \text{Equation 2-4}$$

Thus, the predicted coulometric efficiency is the ratio of the charge expected during the first and second stages of vesicle opening over  $Q_{\max}$ . The resulting equation for coulometric efficiency has been adjusted to only use 25% of the Cottrell equation in the first term. This is needed to correct for diminished diffusion from the narrowing frustum,

and although the volume of the frustum to an equivalent cylinder is 0.33, the frustum is only the middle part of this stage consisting of first a prefrustum with a constricted opening and then an opening later that has walls with inward curvature. Without an exact means to describe this, we assumed a smaller fraction of 0.25 for the diffusion-limited current inside the opening frustum. The equation for this model is given as

$$\% \text{ Coulometric Efficiency} = 0.38[(0.25Q_{\text{frustum}} + Q_{\text{space}})/Q_{\text{max}}]100 \quad \text{Equation 2-5}$$

Although this model accurately predicts the shape of the plot of coulometric efficiency at a 33- $\mu\text{m}$  electrode, it predicts an efficiency that is 2.6-fold higher than that observed. Thus, a correction of 0.38 has been used on the theoretical current for both electrodes. Possible reasons for this deviation in magnitude are as follows. First, the measurement is experimentally difficult and the electrode might not be completely centered over the nanotube and release site. Second, it is highly possible that flow of solution is important, leading to loss of material from the electrode surface and the reduced oxidation efficiency. This is especially true during the intermediate frustum stage where the model assumes that mass transport is by diffusion alone. Clearly, the changing membrane geometry is generating a significant solution velocity vector. This flow from a finite volume will reduce the coulometric efficiency as a significant volume of solution will be transported past the electrode without being in the diffusion layer to be oxidized. This has important implications for cellular processes where diffusion is generally considered the dominant factor in transport across synapses.

The deviation from the curvature for the 5- $\mu\text{m}$  electrode is probably due to the fact that the electrode is smaller than the vesicles used. At these small sizes, it is difficult to ensure that the electrode is centered over the release site. Hence, for the smallest

vesicles, it is even more likely that a significant amount of release occurs to one side of the electrode, and thus, the experimentally observed current would be lower than theoretically predicted. Release from larger vesicles is across such a large cross section that the electrode is covered with released solution even if placement is off center.

This theoretical treatment provides a reasonable fit to the experimental data, with the assumption that the vesicle is in a frustum-like state as it opens, leading to a diffusion-based current at the electrode prior to oxidation in the membrane-electrode space. Even with this assumption, the model is not exact and leads to the conclusion that a significant amount of catechol, beyond that expected with simple volume arguments, flows from the space without being exposed to the electrode surface.

#### **2.3.4 Relevance of the Model to Electrochemical Measurements at Cells with Different Vesicle Sizes**

It is important to realize that, in experiments involving living cells, some systems, like the mast cell, release is from fairly large vesicles. Thus, the stages of vesicle opening and the coulometric efficiency of the oxidation reaction can become significant in the quantitative aspects of the measurement. Table 1 compares parameters for several different known cell types having different vesicle diameters. Immediately after a vesicle is incorporated into the cell membrane, the diameter of the area on the cell covered by the vesicle membrane is twice the diameter of the original vesicle.

**Table 2.1**

vesicle/ cell type	vesicle radius (nm)	fraction of 5- $\mu$ m-dia electrode <sup>a</sup>	fraction of 33- $\mu$ m-dia electrode <sup>a</sup>	vol ratio 5- $\mu$ m-dia electrode 300-nm space <sup>b</sup>	vol ratio 33- $\mu$ m-dia electrode 300-nm space <sup>b</sup>	coulometric efficiency 5- $\mu$ m-dia electrode, eq from Figure 7 <sup>c</sup>	coulometric efficiency 33- $\mu$ m-dia electrode, eq from Figure 7 <sup>d</sup>
synaptic	25	$2.6 \times 10^{-4}$	$5.9 \times 10^{-6}$	$7.2 \times 10^{-06}$	$1.6 \times 10^{-07}$	100	100
PC12 cell	99	$4.1 \times 10^{-3}$	$9.2 \times 10^{-5}$	$4.5 \times 10^{-04}$	$1.0 \times 10^{-05}$	100	100
adrenal cells	125	$6.5 \times 10^{-3}$	$1.5 \times 10^{-4}$	$9.0 \times 10^{-04}$	$2.0 \times 10^{-05}$	100	100
mast cells	400	$6.7 \times 10^{-2}$	$1.5 \times 10^{-3}$	$3.0 \times 10^{-02}$	$6.7 \times 10^{-04}$	100	100
BM <sup>e</sup>	1350	0.76	$1.7 \times 10^{-2}$	1.1	$2.6 \times 10^{-02}$	47	100
BM mast, largest	2000	1.7	0.038	3.7	$8.4 \times 10^{-02}$	25	80
liposome, small	3400	4.8	0.11	18	0.41	11	48
liposome, large	9400	37	0.83	380	8.7	2	18

<sup>a</sup> Fraction of electrode is the ratio of the vesicular membrane area on the cell immediately following exocytosis over the total area of the electrode. The radius of the surface covered when a spherical vesicle is incorporated in to the cell membrane is twice that of the original vesicle. <sup>b</sup> Ratio of volume of vesicle to the membrane-electrode space. The volume of the space was calculated with height of 300 nm and the electrode area. <sup>c</sup> Coulometric efficiency,  $80r_v^{-1.6}$ , where  $r_v$  is the vesicle radius. <sup>d</sup> Coulometric efficiency,  $150r_v^{-0.95}$ , where  $r_v$  is the vesicle radius. <sup>e</sup> BM mast, beige mouse cells. <sup>f</sup> Sizes from the literature include the following: PC12 cells,<sup>20</sup> bovine adrenal cells,<sup>4</sup> and mouse mast and beige mouse mast cells.<sup>21</sup>

The cell area that corresponds to incorporated vesicles is compared to the two electrode areas used in this study in Table 2.1. Noting that the membrane surface filled by an expanding vesicle has a radius twice that of the original sphere, a beveled 5- $\mu$ m electrode (average radius of 3.1  $\mu$ m) has an area 3-4 orders of magnitude larger than that produced by a 25-nm radius synaptic vesicle. However, this drops off rapidly as the vesicle size becomes larger in PC12, adrenal, and then mast cells. The largest vesicles in beige mouse mast cells have been reported to be 2  $\mu$ m in radius,<sup>19</sup> and this is almost 1.7 times the area of a beveled 5- $\mu$ m-diameter electrode. The vesicles used in the artificial cell experiments range from 3.4 to 9.4  $\mu$ m in radius and have membrane areas that are 4.8-37 times the area of the 5- $\mu$ m electrode. Vesicles of this size correspond to 11-83% of a 33- $\mu$ m electrode. The areas for the smaller vesicles found in neurons, PC12, and adrenal cells are all at or below 1% of the electrode area. However, most exocytosis measurements at cells have been carried out with the smaller 5- and 10- $\mu$ m electrodes, and it is clear that the relative ratio of the vesicle to electrode area needs to be considered when planning and evaluating data obtained at cells with the larger vesicles.

The disparity in coulometric efficiency is even more apparent when one considers the volume of the space between the electrode and the membrane compared to the volume of a vesicle. This is also presented in Table 2.1. Here the volumes are calculated for spherical vesicles from different cell and artificial cell types, and the electrode-membrane space is calculated using a 300-nm space (based on the model above). The larger the ratio of the vesicle volume to electrode-membrane space, the greater the extent of transmitter that is likely to escape the gap. For the 5- $\mu\text{m}$  electrode, this ratio ranges from  $7.2 \times 10^{-6}$  for a 25-nm synaptic vesicle to 3.7 for the largest mast cell vesicle. Therefore, it is doubtful that measurements of the largest mast cell vesicles are truly quantifiable with an electrode of this size. Interestingly, the volume for a typical adrenal cell vesicle is 0.09%, the volume of this space making those measurements quantifiable. The volume of the electrode-membrane space is much larger when a 33- $\mu\text{m}$  electrode is used. In this case, amperometric measurements at the artificial cells are in the range of efficiencies that are observed for large mast cell vesicles at 5- $\mu\text{m}$  electrodes.

The experimental data from Figure 2.7 has been fitted to a curve and that curve is used to estimate the expected coulometric efficiencies for the vesicles listed in Table 1. This assumes that all vesicles are released in the center of the electrode (an optimistic assumption) and shows that in this case all systems should provide a nearly complete coulometric efficiency with the exception of the artificial cell and the largest mast cell vesicles. It is important to note, however, that the chance of a vesicle being released near the edge of an electrode is larger than in the direct center and thus these estimates are optimistic. More complicated models are needed to provide a final answer to the quantifiability of amperometric measurements of exocytosis.

### 2.3.5 Mass Transport in Small Places: Relevance to Transmission in the Synapse

The data presented in this chapter demonstrate that, under the right conditions, a large amount of transmitter released under an electrode will escape the space between the membrane and the electrode. As mentioned above, this system is a viable model of what takes place at a synapse in vivo where the space is the synaptic cleft, exocytosis releases transmitter on the presynaptic side, and the electrode “captures” transmitter much as a receptor or transporter would on the postsynaptic side. A great deal of recent work with in vivo methods has shown that, at dopamine and serotonin synapses, most of the neurotransmitter escapes the synapse following exocytotic release.<sup>12,14</sup> The model presented here suggests that, in addition to diffusion out of the synapse, some of the transmitter might be physically pumped out by exocytosis when the volume of the vesicle exceeds that of the synapse. If we consider a synapse with a space of 20 nm and an average diameter of the exposed postsynaptic surface of 0.1  $\mu\text{m}$ , then ~70% of the volume of a 100-nm-diameter dopamine vesicle released into the synapse will be pumped directly out into the extrasynaptic space. Thus, the relative volume of the vesicle to the synaptic cleft, the time during which the vesicle is in a partially open frustum-like stage, and the rate of fluid flow during exocytosis are all likely to impact the availability of released transmitters to interact with receptors at the postsynaptic membrane as well as the amount of transmitter that escapes the synapse.

## 2.4 Literature Cited

1. Wightman, R. M.; Jankowski, J. A.; Kennedy, R. T.; Kawagoe, K. T.; Schroeder, T. J.; Leszczyszyn, D. J.; Near, J. A.; Diliberto, E. J., Jr.; Viveros,

- O. H. *Proc. Natl. Acad. Sci. U.S.A.* **1991**, *88*, 10754-10758.
2. Ciolkowski, E. L.; Cooper, B. R.; Jankowski, J. A.; Jorgenson, J. W.; Wightman, R. M. *J. Am. Chem. Soc.* **1992**, *114*, 2815-2821.
  3. Neher, E.; Marty, A. *Proc. Natl. Acad. Sci. U.S.A.* **1982**, *79*, 6712-6716.
  4. Chow, R. H.; von Ruden, L.; Neher, E. *Nature* **1992**, *356*, 60-63.
  5. Smith, C. B.; Betz, W. J. *Nature* **1996**, *380*, 531-534.
  6. Oheim, M.; Loerke, D.; Stuhmer, W.; Chow, R. H. *Eur. Biophys. J.* **1998**, *27*, 83-98.
  7. Steyer, J. A.; Almers, W. *Biophys. J.* **1999**, *76*, 2262-2271.
  8. Zenisek, D.; Steyer, J. A.; Almers, W. *Nature* **2000**, *406*, 849-854.
  9. Schroeder, T. J.; Jankowski, J. A.; Kawagoe, K. T.; Wightman, R. M.; Lefrou, C.; Amatore, C. *Anal. Chem.* **1992**, *64*, 3077-3083.
  10. Anderson, B. B.; Zerby, S. E.; Ewing, A. G. *J. Neurosci. Methods* **1999**, *88*, 163-170.
  11. Anderson, B. B.; Chen, G.; Gutman, D. A.; Ewing, A. G. *J. Neurosci. Methods* **1999**, *88*, 153-161.
  12. Garris, P. A.; Ciolkowski, E. L.; Pastore, P.; Wightman, R. M. *J. Neurosci.* **1994**, *14*, 6084-6093.
  13. Bunin, M. A.; Wightman, R. M. *J. Neurosci.* **1998**, *18*, 4854-4860.
  14. Bunin, M. A.; Wightman, R. M. *Trends Neurosci.* **1999**, *22*, 377-382.
  15. Cans, A. S.; Wittenberg, N.; Karlsson, R.; Sombers, L.; Karlsson, M.; Orwar, O.; Ewing, A. *Proc. Natl. Acad. Sci. U.S.A.* **2003**, *100*, 400-404.
  16. Karlsson, R.; Karlsson, M.; Karlsson, A.; Cans, A.-S.; Bergenholtz, J.; Åkerman, B.; Ewing, A.; Voinova, M.; Orwar, O. *Langmuir* **2002**, *18*, 4186-4190.
  17. Karlsson, M.; Nolkranz, K.; Davidson, M. J.; Stromberg, A.; Ryttsen, F.; Åkerman, B.; Orwar, O. *Anal. Chem.* **2000**, *72*, 5857-5862.
  18. Amatore, C.; Bouret, Y.; Travis, E. R.; Wightman, R. M. *Biochimie* **2000**, *82*, 481-496.
  19. Brodwick, M. S.; Curran, M.; Edwards, C. *J. Membr. Biol.* **1992**, *126*, 159-169.
  20. Colliver, T. L.; Pyott, S. J.; Achalabun, M.; Ewing, A. G. *J. Neurosci.* **2000**, *20*, 5276-5282.
  21. Breckenridge, L. J.; Almers, W. *Proc. Natl. Acad. Sci. U.S.A.* **1987**, *84*, 1945-1949.

## Chapter 3

### Variation in Lipid Headgroup Concentration Alters Release Kinetics in a Liposome Model of Exocytosis as Determined by Electrochemical Detection

#### 3.1 Introduction

Lipids play a vital role in cellular function as precursors for many second messengers in cell signaling cascades, but they also provide scaffolding for the interplay of enzymes and proteins.<sup>1</sup> When lipids are in the appropriate ratios, lipid microdomains have been shown to play a major role in protein recruitment and cell signaling.<sup>2-4</sup> Membrane microdomains are aggregations of lipids in a specific conformation that differs from the lipid composition in its immediate vicinity.<sup>5</sup> These microdomains appear to self assemble and recruit a protein whose function can be altered by the lipid environment.<sup>6-8</sup> Moreover, microdomain formation is dependent on specific lipid compositions.

These microdomains have specific properties that differentiate them from the bulk lipid composition.<sup>1</sup> Microdomain formation is not completely understood but has been shown to be present in various studies when either the head or tail groups vary compared to the majority of the lipids in solution.<sup>9</sup> Another example of lipid microdomains would be a complexation reaction with cholesterol that forms a more stable interaction with one cholesterol and two phosphocholines.<sup>10-12</sup> Since lipids have the ability to diffuse freely in a membrane, spontaneous domain formation is possible. Also, in the absence of cholesterol, lipid domain formation is not common for acyl chains in the medium length range, 16 to 18 carbon chains.<sup>13</sup>

It has been suggested that lipid functionality is linked to molecular shape.<sup>14</sup> Lipid shapes are classified as cylindrical, conical and hexagonal II, or inverse cone based on the relative size of the head group compared to the tail groups.<sup>15</sup> Cylindrical shaped lipids, with headgroups comparable to the size of the tail groups, favor a bilayer orientation, while cone (headgroup smaller than acyl chains) and inverse cone (acyl chains smaller than headgroup) shapes favor non-bilayer configurations.<sup>15</sup> Therefore a mixture of these lipid types in a plasma membrane affects overall membrane curvature and therefore exocytotic dynamics.<sup>16</sup>

Liposomes provide an excellently controlled system in which to analyze the effects of lipid composition on exocytosis. Lentz et al. monitored the fusion of liposomes as a model for exocytosis.<sup>17, 18</sup> Zimmerberg et al. have used liposomes to evaluate lipid fusion in planar bilayer systems.<sup>19</sup> Both Lentz and Zimmerberg required proteins to initiate fusion and therefore were unable to pinpoint the exclusive effects of lipids. Groves and coworkers have utilized liposomes to analyze lipid functionality based on composition in static systems.<sup>20, 21</sup> Kahya et al. examined the relative mobility of fluorescent lipids through various lipid compositions in giant unilamellar liposomes using fluorescence correlation spectroscopy.<sup>22</sup> Here, we have developed a purely lipidic model that represents a dynamic system of exocytosis.<sup>23, 24</sup>

Our liposome model consists of a smaller liposome inside a larger liposome with a lipid nanotube connecting the two. Inflation of the inner liposome, representing a vesicle for a cellular system, leads to a shrinking of the lipid nanotube and its eventual loss resulting in distention of the inner liposome into the outer liposome. By placing electroactive neurotransmitter analogues into the inner liposome, we are able to measure

the kinetics of the release process in this artificial model. Coupled with electrochemical detection, we have shown that membrane mechanics are likely to drive this distention due to the high energy intermediate formed by the nanotube.<sup>23</sup> We have also used this model to better understand the quantification of amperometric experiments and as an artificial synapse.<sup>24</sup>

Lipid curvature should affect the fusion of two opposed membranes, like the fusion of the vesicular and the cellular membrane during exocytosis. A vesicle with a higher degree of curvature is more likely to fuse than one with a lesser amount of curvature. The reason that curvature affects fusion is that a liposome with a high curvature has more potential energy and would be more stable in the plasma membrane.<sup>25</sup> A membrane with a high percentage of cylindrically shaped lipids would exhibit less curvature compared to a membrane with a high percentage of cone shaped lipids. When sizing up these two different lipid shapes, cone shaped lipids have head groups that occupy less space. This allows for tighter packing of the headgroups and therefore a greater amount of curvature. Also the curvature of the membrane depends upon which monolayer the lipid preferentially aggregates. Generally, cone shaped lipids favor the inner monolayer of the cellular bilayer.<sup>15</sup> Cylindrical lipids can function equally well in both layers (inner or outer) and inverse cone shaped lipids favor the outer layer. Due to the nature of lipidic fusion during exocytosis, vesicular membranes are the mirror image of the plasma membrane in which they interact. The lipids contained in the outer leaflet for a vesicle will become the inner leaflet upon fusion with the plasma membrane.

In order to help visualize the orientation of lipids in a section of membrane under high curvature (e.g. a lipid nanotube or exocytosis fusion pore), models of highly curved

pores (or tubes) are shown in Figure 3.1. In the first model (Figure 3.1A), the membrane is enriched with lipids with an inverse cone shape (i.e. lysolipids) and there is a clear increase in space between the tail groups leading to a higher energy state. In the second model (Figure 3.1B), the lipids are all cylindrical in shape and the outer leaflet is overcrowded while the inner leaflet is not completely packed, leading to an intermediate energy state. In the third model (Figure 3.1C), the addition of cone shaped lipids provides a better packing density and the conical lipids fit better in higher numbers in the inner leaflet of the fusion pore or nanotube. Thus, this simple model predicts that all lipids will flow down a lipid nanotube, it is clear that in low numbers, and one type of lipid will be selectively transported to minimize the energy from curvature, for vesicles under one micron.

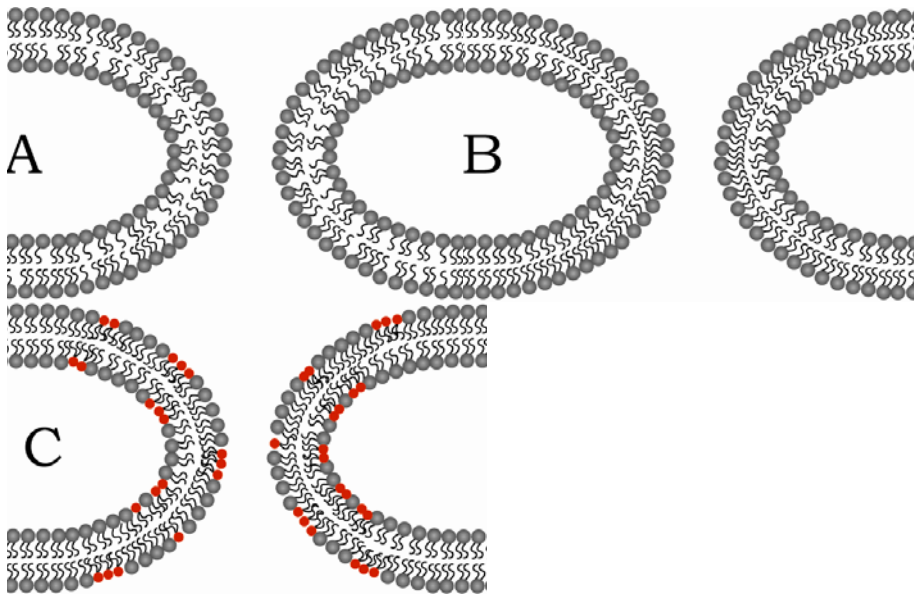


**Figure 3.1** Illustrations of three extremes of lipid composition showing the lipid packing in a lipid nanotube or fusion pore between liposomes. (A) Example showing the packing of the tail groups when an inverted cone shaped lipid is dominant in concentration. (B) Example showing the packing when a purely cylindrical lipid shape is present. (C) Example showing the packing when cone shaped lipids are combined with cylindrical lipids in the region of high curvature.

In this chapter, the phospholipid composition in liposomes has been quantitatively altered and the kinetics of membrane distention during the final stages of exocytosis has been examined. Electroactive catechol loaded into these artificial vesicles has been measured by carbon fiber amperometry and release kinetics has been determined from these data. In addition, fluorescent dyes have been used to measure the extent of lipid transport through the nanotubes during formation of the daughter liposome.

### 3.2 Materials and Methods

Soy polar extract, PLPC (1-palmitoyl-2-linoleoyl-*sn*-glycero-3-phosphocholine), PLPS (1-palmitoyl-2-linoleoyl-*sn*-glycero-3-phosphoserine), Soy PI (phosphatidylinositol), and PLPE (1-palmitoyl-2-linoleoyl-*sn*-glycero-3-phosphoethanolamine) were purchased from Avanti Polar Lipids, Inc. ( Alabaster, AL). DiI was purchased from Invitrogen (Carlsbad, CA). Catechol, ethylenediamine tetraacetic acid (EDTA), potassium phosphate and tris[hydroxymethyl]aminomethane (Trizma base) were purchased from Sigma Chemical Company (St. Louis, MO). Carbon fibers (33  $\mu\text{m}$ ) were purchased from Textron Specialty Materials (Lowell, MA). Pro CFE (Dagan Corp, Minneapolis, MN) were used to fabricate counter electrodes for electroporation. Pipettes were pulled from borosilicate glass capillaries purchased from Harvard Apparatus (i.d. 0.79 mm, o.d. 1 mm Holliston, MA ) and pulled using a commercial glass puller (T-97 Sutter, Novartis, CA) Confocal images were taken on Leica TCS-SP5 Microscope (Wetzlar, Germany).

### 3. 2.1 Liposome Preparation

Surface immobilized unilamellar liposomes were made using soy polar extract and a dehydration/rehydration method described previously.<sup>23</sup> Briefly, a micropipette was inserted into the parent liposome (Figure 3.2A), and then through the other side of the liposome (Figure 3.2B). The pipette was retracted back through the bilayer, where the lipid adheres to the pipette, creating a nanotube (Figure 3.2C). To inflate the inner liposome, pressure was applied to the micropipette by means of a femtojet microinjector (Eppendorf, Germany). After sufficient inflation, the liposome resembled a docked vesicle associated with the larger liposome membrane (Figure 3.2D). At this point the vesicle releases its contents (Figure 3.2E-H). The lipid nanotube remained attached to the pipette tip after release (Figure 3.2H), allowing for repeated measurements from the same liposome system with identical conditions to be carried out.

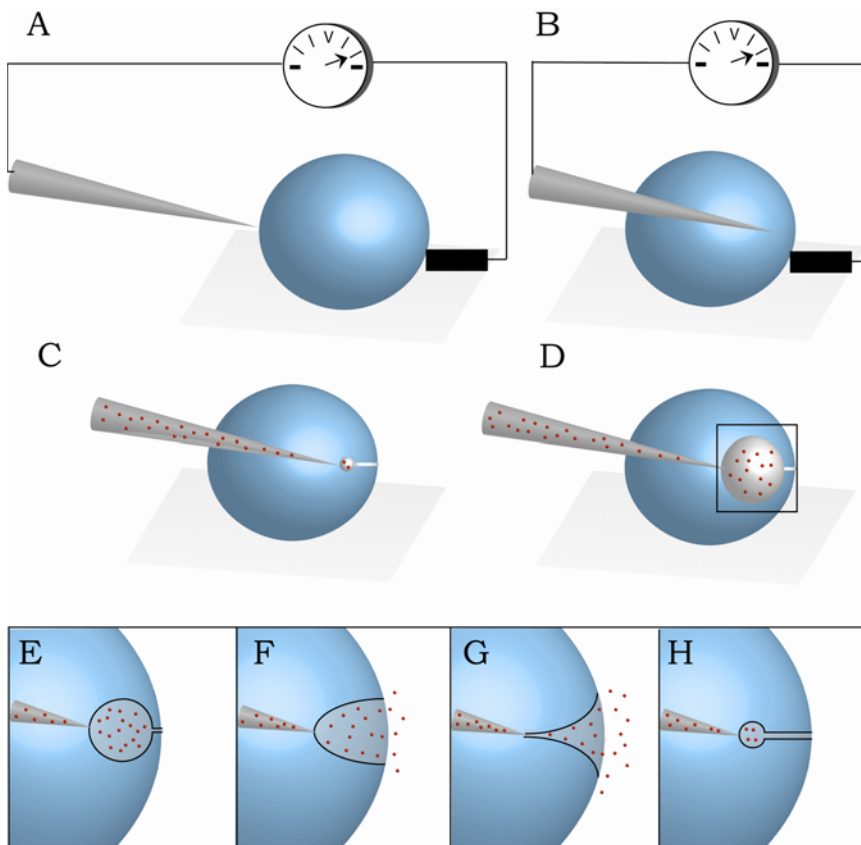


**Figure 3.2** A schematic illustration of the formation of the artificial exocytosis model. (A) A micropipette is inserted into a liposome by means of electroporation. An electrical stimulus disrupts the membrane and allows the pipette into the liposome. (B) The pipette continues through the liposome and upon contact with the other side is again stimulated and passes through the membrane. (C) Then the pipette is drawn back inside the liposome to create a smaller liposome connected by a nanotube. (D) Pressure is applied through the pipette which inflates the small liposome until it reaches fusion with the larger liposome.

The initial polar extract was augmented by the addition of 25 % PLPC, PLPE, Soy PI, or PLPS. It is important to note that the reason for the augmentation of the soy polar extract, in lieu of using pure lipid mixtures (i.e. 100% PLPC), is that a specific liposome configuration, a unilamellar liposome attached to a multilamellar liposome, is necessary for analysis. Pure lipid mixtures do not exhibit this important configuration and therefore, are not able to be used for our experiments. Similarly large deviations from the soy polar extract mixture prevent the necessary liposome complex formation; thus, 25%

was determined to be sufficient to see a change and allow for the necessary complex. Each liposome mixture was manipulated by a glass micropipette to form a liposome inside a liposome connected by a lipid nanotube which constitutes an artificial cell model of exocytosis.

### **3.2.2 Electrochemical Detection**

Electrochemical detection was carried out with a 33- $\mu\text{m}$  carbon fiber electrode placed flush with the larger liposome to monitor release from the smaller vesicle.<sup>23</sup> A solution of 1 mM catechol in 30 mM phosphate buffer (5 mM Trizma base, 30 mM  $\text{K}_3\text{PO}_4$ , 30 mM  $\text{K}_2\text{HPO}_4$ , and 0.5 mM EDTA adjusted to pH 7.4 with  $\text{H}_2\text{SO}_4$ ) was placed in the injection pipette and introduced into the vesicle system.

### **3.2.3 Confocal Imaging of Liposomes**

For confocal imaging, >1% DiI was added to the lipid mixture before removal of chloroform by rotoevaporation. The same protocol was observed for lipid film. Instead of drawing the liposome inside the lipid was pulled outside resulting in a barbell shaped liposome system.

## **3.3 Results and Discussion**

In order to determine the rate of membrane distention during the latter stages of exocytosis, catechol release from the smaller liposomes was measured by amperometric

detection. The data collected from amperometry manifests itself as a current transient (Figure 3.3) defined by the release rate of electroactive agent from the liposome (Figure 3.2F, G). The width of the peak at half of the maximum value (or halfwidth) is used as a measure of release rate. Similarly, halfwidth measurements are used to determine the duration of a fusion event in cell experiment and proves useful when comparing cellular events with this model. By comparing the differences in halfwidths it is possible to determine the effect that each lipid mixture has on the rate of liposome distention. The capability to augment the total lipid headgroup percentage with a non-native lipid added to the system provides the ability to quantitatively examine specifically controlled changes in membrane properties.

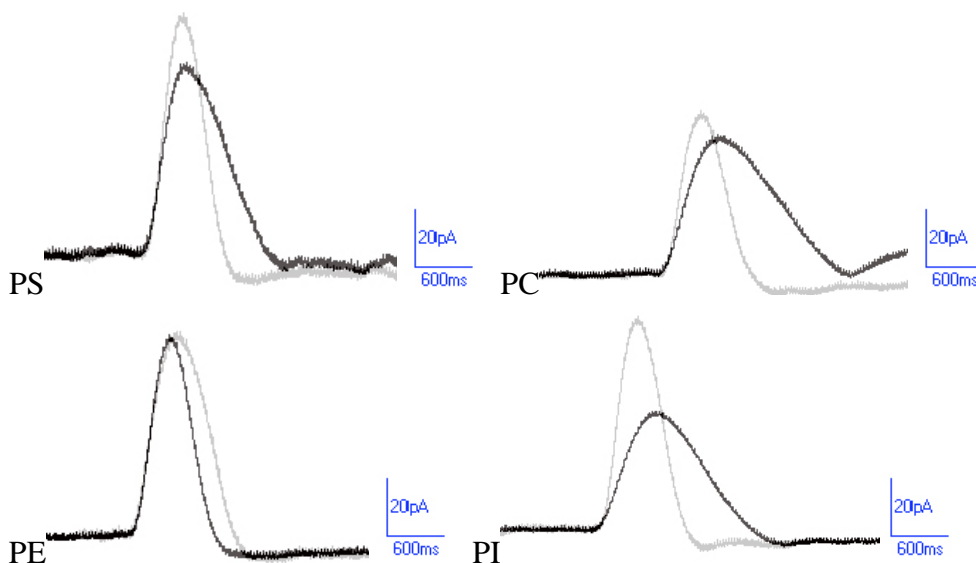


**Figure 3.3** An overlay of two amperometric traces resulting from monitoring release from a control liposome (gray) vs. a phospholipid-enriched liposome (black) of the same size. Enrichment of lipid is by 25 % addition of the labeled lipid to the liposome preparation. The enriched liposome events for PC, PI, and PS are larger due to the slow release brought on by the enrichment of cylindrical shaped lipid.

### 3.3.1 Increasing Phosphatidylserine

We initially supplemented liposomes with phosphatidylserine (PS). In order to diminish changes in release rate due to the variation in the lipid tail groups used in the experiment, the most common tail groups found in soy extract were considered for the supplemental lipids. These fatty acid acyl chains being palmitoyl (16 carbons, saturated) and linoleoyl (18 carbons, two degrees of unsaturation) and the additive lipid was (1-palmitoyl-2-linoleoyl-*sn*-glycero-3-phosphoserine) PLPS.

Upon addition of PLPS, the changes in the amperometric spikes show a distinct increase in halfwidth (Figure 3.3, upper left). As there is essentially no phosphatidylserine in the soy extract, its addition does not affect the relative ratios of the other lipids with respect to each other; however it does decrease their overall amount of soy lipid in the liposomes. The increase in halfwidth confirms that it takes longer for the vesicle to open. Table 3.1 lists the lipid percentages for each altered liposome and compares it to soy and by doing so notice the percentage of cylindrical vs. conical lipids. The PLPS supplemented liposomes have more cylindrical lipids and therefore would be expected to favor a bilayer configuration and when placed in a high curvature intermediate necessary for exocytosis, there is a reduction in release.

	Soy Polar Extract	25% PLPS	25% PLPC	25% PLPE	25% Soy PI
Phosphatidic Acid	6.9	5.18	5.18	5.18	5.18
Phosphatidylcholine	45.7	34.3	59.3	34.3	34.3
Phosphatidylethanolamine	22.1	16.6	16.6	41.6	16.6
Phosphatidylinositol	18.4	13.8	13.8	13.8	38.8
Phosphatidylserine	0	25	0	0	0
Undetermined headgroup	6.9	5.18	5.18	5.18	5.18
Cylindrical lipids	<b>64.1</b>	<b>73.1</b>	<b>73.1</b>	<b>48.1</b>	<b>73.1</b>
Conical lipids	<b>29</b>	<b>21.8</b>	<b>21.8</b>	<b>46.8</b>	<b>21.8</b>

**Table 3.1** Percentage of phospholipid head groups in each sample for analysis.<sup>29</sup>

### 3.3.2 Increasing Phosphatidylcholine

The addition of phosphatidylcholine (PC) to soy-derived liposomes results in a significant increase in the halfwidth of the amperometric transient (Figure 3.3, upper right). This increase in halfwidth is greater than the increase observed for PLPS showing an even greater increase in catechol release time during lipid distention. This is especially significant because PC makes up 45 % of the initial soy mixture and by increasing this already abundant lipid, a larger difference was recorded. In addition, the net effect of adding 25 % PC was to increase the percentage of cylindrical lipids to 73.1 % of the total, identical to that of adding 25 % PS (Table 3.1). Comparison of PS and PC enriched liposomes shows that the changes observed for PC resulted from more than a simple increase in cylindrical shaped lipid. If it were then we would expect to see the same response as with PS. A possible interpretation of the large difference in halfwidth for PC-supplemented liposomes, when compared to PS, is that the large overall percentage of PC increases the likelihood of aggregation of PC around the fusion pore and to predominate throughout the liposome.<sup>26</sup> The absence or reduced availability of conical lipids would further hinder the opening of the vesicle and seems to be manifest here in the PC enhanced liposome.

### 3.3.3 Increasing Phosphatidylethanolamine

Phosphatidylethanolamine is the second most abundant lipid in soy polar extract and it can be inferred that PE plays a significant role in our system. The addition of PLPE to the liposome mixture leads to exocytosis events exhibiting a decrease in halfwidth of

the amperometric spike (Figure 3.3, lower left). As PE is a conically shaped lipid, this result agrees with the established theory of cone shaped lipids increasing bilayer curvature and therefore reducing the energy required for the membrane to transition through the high curvature fusion pore. When compared to the changes observed for the addition of PC or PS (Figure 3.4), the change in peak halfwidth for PE supplemented liposomes is less pronounced. This finding suggests that the rate of the lipid distention is more easily slowed than quickened and may reflect the overall function of a membrane is dictated by the majority of lipids with a specific shape (in this case, there was still a large percentage of cylindrical shaped lipids).

### Soy Polar Extract with 25% Lipid Additives

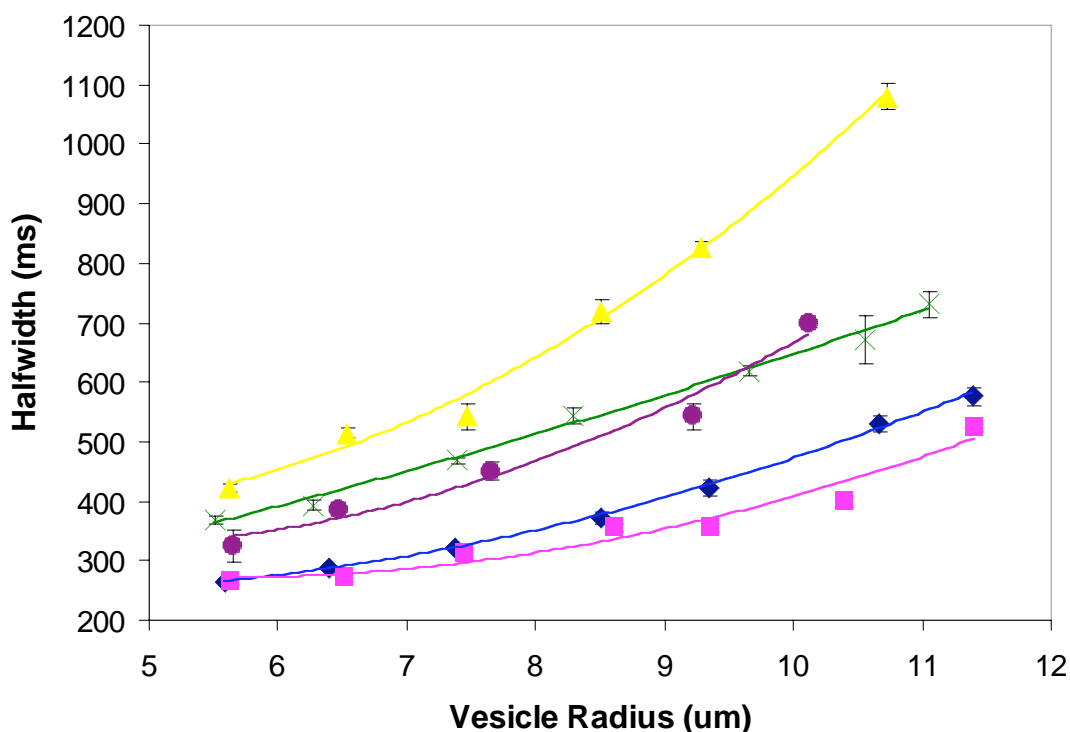


**Figure 3.4** Plot of amperometric current transient halfwidths as a function of varied composition of lipid head groups. (◆) Control (●) PS (▲) PC (■) PE (×) PI Conditions the same as Figure 3.3. Error bars denote standard error of the mean.

### 3.3.4 Increasing Phosphatidylinositol

The final lipid used to alter membrane composition was phosphatidylinositol. Soy PI was used because PLPI was unavailable and because soy PI extract, 80 % of the acyl chains are the same as PLPI.<sup>19</sup> Moreover, the remaining acyl chains in soy PI are what you would find in soy polar extract. The enrichment of soy PI resulted in an increase in halfwidth for the amperometric transients (Figure 3.3, lower left). This result can be attributed to an increase of cylindrical shaped lipids in the membrane or an increase in the positive charge in the membrane. The increase in halfwidth observed was not as dramatic as that observed for PC, yet similar to the result observed for PS suggesting these two lipids have similar shape-based effects on membrane function in our system.

### 3.3.5 Quantitative Comparison of the Effect of Lipid Additives on Release Transients

Examining the data in Figure 3.4, it is apparent that the rate of liposome opening for PE-supplemented liposomes is almost identical to that of control up to 9  $\mu\text{m}$ , but once they achieved a larger radius the differences were more distinct. Yet, the three other additives were distinctly different over the whole range of sizes. When cylindrical shaped lipids are in abundant supply, there is little change in the release characteristic, but if the ratio of conical to cylindrical lipids is reduced the membrane reacts markedly. This result shows the nanotube, our model's fusion pore, as a point of critical importance, since is most likely that this structure in this model is the point that would be most affected by a reduction in conical shaped lipids.

Hamai et al. have shown an increase in PE reduces the ability of small unilamellar liposomes to fuse to a glass surface to form a bilayer.<sup>27</sup> They attribute this finding to an increase of negative curvature that prevents the liposome from making favorable contact with the glass surface. To counteract the negative curvature, they added lysoPC, to change the overall curvature to what would more likely be found in a bilayer, and it was shown that not only did vesicles form bilayers with the addition of lysoPC but the relative lipid mobility increased as well.<sup>27</sup> This suggests that the increase of lipid curvature also limits the mobility of the lipid within a supported bilayer. Keeping this in mind, it can be inferred that increasing membrane curvature slows down the movement of lipids within the bilayer. When PE enriched liposomes adopt a high curvature intermediate, such as a fusion pore, the lipid movement is decreased but the stability is greater due to reduced strain in the bilayer that comes from the additional space created by the smaller headgroup. However, at the smaller sizes, addition of PE does not result in a significant change from control. The liposome-lipid nanotube opening appears to be close to a stable configuration in the original soy membranes and addition of PE has a small effect.

If the highly curved intermediate represented by the nanotube causes a reduction in lipid movement in the bilayer then all of the cylindrical lipid supplementations should exhibit the same behavior. However, there is a disparity in the case of PLPC which displays a greatly increased halfwidth over its PS and PI counterparts. This suggests that nanotube stability is not the only factor involved in controlling this process. The ability of the dominant lipid type, PC, to reduce the overall curvature seems to be significant. So much so that the increase in release time for PC is almost twice that of PI and PS for the larger liposomes. It is highly likely that PC is important in regulating the pore or

nanotube based on a lesser probability to enter and traverse these highly curved structures relative to conical lipids like PE.

One unique feature of our model exocytosis model is that all of the lipid material that the inner “vesicle” (daughter liposome) is comprised of comes from the outside liposome. More specifically it has to travel through a highly curved intermediate in the junction of the nanotube and the outer liposome. As the inner liposome expands under the pressure exerted by the pipette, lipids are transported along the nanotube to accommodate the expanding surface area of the inner liposome. Thus, the relative abundance of non bilayer forming lipids in the inner liposome might increase if the nanotube acts as a selective conduit for conical lipids.<sup>28</sup> This could happen as the lipid nanotube has a smaller sterically strained geometry. Thus, in the case of PE, larger inner liposomes should have a higher abundance of conical lipids and demonstrate a larger effect on the release rate during liposome distention.

In order to investigate the theory that the nanotube acts a lipid gate, confocal microscopy images were obtained of fluorescently labeled soy polar extract liposomes. These liposomes were made by the same procedure as previous soy liposomes with >1% DiI added to the mixture. One liposome was pulled out and allowed to inflate. Once the liposome got to a reasonable size the pressure injection was stopped and fluorescence images were obtained (Figure 3.5A). A line scan was carried out for each liposome to determine the relative intensity of the fluorophore in each liposome and the resultant graph shows a decrease in the amount of intensity for the daughter liposome where the lipid traveled through the nanotube (Figure 3.5B). A total of 7 liposome pairs were examined this way and the average ratio of the fluorescence intensity for the daughter relative to the

parent was  $0.66 \pm 0.05$ . This result supports the idea that the nanotube can gate or exclude specific lipids. DiI has a large head group and would act similarly to a cylindrically shaped lipid and thus would not act to stabilize the nanotube. In this model, the junction between the nanotube and each liposome acts as a congregation point. Low curvature lipids are expected to aggregate here as they are statistically less likely to move through the highest curvature point in the structure, and thus they are transported at slower rates than the high curvature lipids. As the vesicle increases in size so does the amount of conical lipid. This finding leads to the hypothesis that the fusion event in cells might be dependent not only in the lipid in the nanotube but also that differences in the amounts of specific lipids that have passed through the lipid nanotube into a vesicle undergoing release might be important. If the smaller PE is concentrated in the nanotube, it is possible that a liquid ordered domain is formed in the PE-depleted membrane near the nanotube owing to an increase in overall PC in this region. In the liposome model of exocytosis, this might account for the more distinct difference in the release kinetics for the distension of PE-enriched vesicles as the liposome radius increases, and in the cell system it could result in a process for regulating release in neurocommunication.

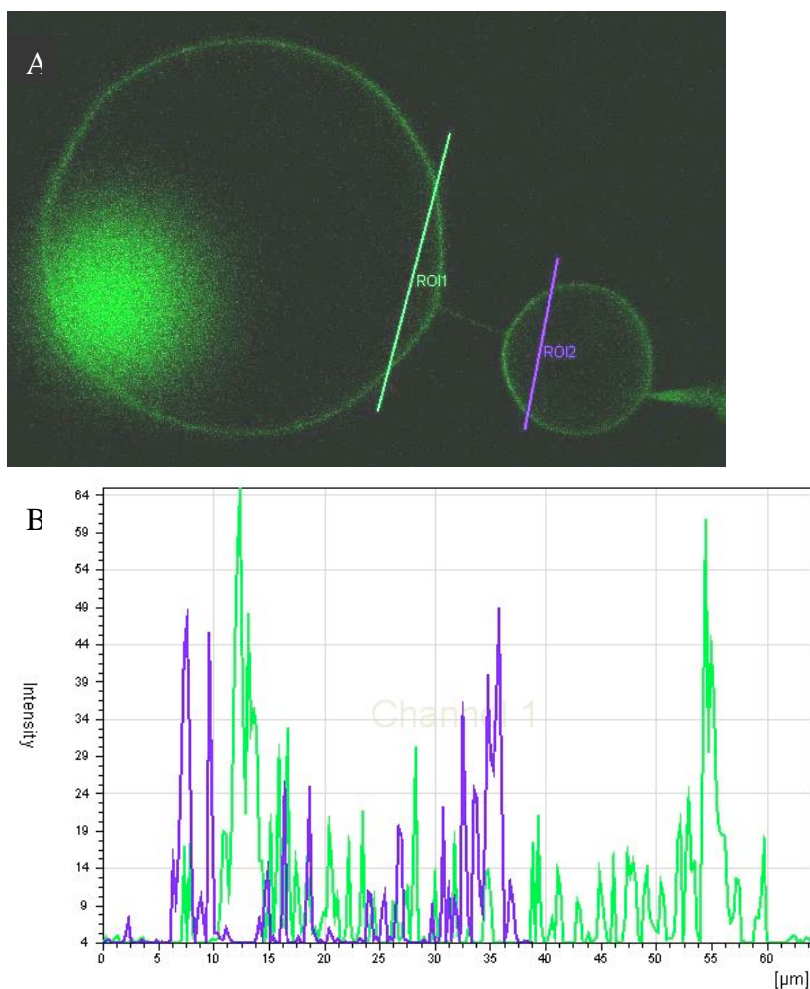


**Figure 3.5** Line scans of two liposomes connected by a nanotube. (A) Confocal image of two liposomes connected a lipid nanotube. DiI is used as a fluorophore added as >1% of the total lipid concentration. The liposome on the right is the daughter liposome which contains lipid material that has passed through the lipid nanotube. (B) Graph of the relative fluorescence intensity of the line scans in A. The overall brightness of the liposome on the right is less than that on the left based. The purple line scan is 39  $\mu\text{m}$ .

### 3.4 Summary of Lipid Additive's Effect on Exocytosis

Changes in lipid composition can facilitate or inhibit the formation or function of the highly curved structures found in dynamic processes such as exocytosis. We have devised a model in which it is possible to show how these changes in lipid composition affect the membrane properties in the later stages of exocytosis. In our model of

exocytosis, cylindrical shaped lipids have a large effect on the release dynamics monitored by amperometry with PC having the greatest effect. Increases in conical shaped lipids like PE reduce release times owing to greater adaptability in high curvature structures such as lipid nanotubes or a fusion pore.

### 3.5 Literature Cited

- (1) Osborne, S. L.; Wen, P. J.; Meunier, F. A. *Journal of Neurochemistry* **2006**, *98*, 336-342.
- (2) Lindquist, J. A.; Simeoni, L.; Schraven, B. *Immunological Reviews* **2003**, *191*, 165-182.
- (3) Israelachvili, J. N.; Mitchell, D. J.; Ninham, B. W. *Biochimica et Biophysica Acta (BBA) - Biomembranes* **1977**, *470*, 185.
- (4) Israelachvili, J. N.; Mitchell, D. J. *Biochimica et Biophysica Acta (BBA) - Biomembranes* **1975**, *389*, 13.
- (5) Edidin, M. *Current Opinion in Structural Biology* **1997**, *7*, 528.
- (6) Raghuvver, P.; Paul, A. C.; Jay, T. G. *Physical Review Letters* **2005**, *95*, 048101.
- (7) Chernomordik, L.; Leikina, E.; Cho, M. S.; Zimmerberg, J. *J. Virol.* **1995**, *69*, 3049-3058.
- (8) Vrljic, M.; Nishimura, S. Y.; Moerner, W. E.; McConnell, H. M. *Biophys. J.* **2005**, *88*, 334-347.
- (9) Nishimura, S. Y.; Vrljic, M.; Klein, L. O.; McConnell, H. M.; Moerner, W. E. *Biophys. J.* **2006**, *90*, 927-938.
- (10) Silvius, J. R. *Biophys. J.* **2003**, *85*, 1034-1045.
- (11) Stottrup, B. L.; Stevens, D. S.; Keller, S. L. *Biophys. J.* **2005**, *88*, 269-276.
- (12) Anderson, T. G.; McConnell, H. M. *Biophys. J.* **2002**, *83*, 2039-2052.
- (13) Feigenson, G. W.; Buboltz, J. T. *Biophys. J.* **2001**, *80*, 2775-2788.
- (14) London, E. *Biochimica et Biophysica Acta (BBA) - Molecular Cell Research* **2005**, *1746*, 203.
- (15) Corda, D.; Hidalgo Carcedo, C.; Bonazzi, M.; Luini, A.; Spano, S. *Cellular and Molecular Life Sciences* **2002**, *59*, 1819-1832.
- (16) Chernomordik, L.; Kozlov, M. M.; Zimmerberg, J. *Journal of Membrane Biology* **1995**, *146*, 1-17.
- (17) Haque, M. E.; McIntosh, T. J.; Lentz, B. R. *Biochemistry* **2001**, *40*, 4340-4348.
- (18) Cutsforth, G. A.; Whitaker, R. N.; Hermans, J.; Lentz, B. R. *Biochemistry* **1989**, *28*, 7453-7461.
- (19) Chanturiya, A.; Chernomordik, L. V.; Zimmerberg, J. *PNAS* **1997**, *94*, 14423-14428.
- (20) Yamazaki, V.; Sirenko, O.; Schafer, R. J.; Groves, J. T. *J. Am. Chem. Soc.* **2005**, *127*, 2826-2827.

- (21) Groves, J. T.; Dustin, M. L. *Journal of Immunological Methods* **2003**, 278, 19.
- (22) Kahya, N.; Scherfeld, D.; Bacia, K.; Schwille, P. *Journal of Structural Biology* **2004**, 147, 77.
- (23) Cans, A.-S.; Wittenberg, N.; Eves, D.; Karlsson, R.; Karlsson, A.; Orwar, O.; Ewing, A. *Anal. Chem.* **2003**, 75, 4168-4175.
- (24) Cans, A.-S.; Wittenberg, N.; Karlsson, R.; Sombers, L.; Karlsson, M.; Orwar, O.; Ewing, A. *PNAS* **2003**, 100, 400-404.
- (25) Israelachvili, J. N. *Biochimica et Biophysica Acta (BBA) - Biomembranes* **1973**, 323, 659.
- (26) Silvius, J. R. *Biochimica et Biophysica Acta (BBA) - Biomembranes* **1986**, 857, 217.
- (27) Hamai, C.; Yang, T.; Kataoka, S.; Cremer, P. S.; Musser, S. M. *Biophys. J.* **2006**, 90, 1241-1248.
- (28) Mui, B. L.; Dobereiner, H. G.; Madden, T. D.; Cullis, P. R. *Biophys. J.* **1995**, 69, 930-941.
- (29) Avanti Polar Lipids Inc. site. <http://www.avantilipids.com/NaturalProducts.asp> (Accessed March 2007)

## Chapter 4

### Steady State Electrochemical Determination of a Lipid Nanotube Diameter

#### 4.1 Introduction

There has been great interest in mimicking important biological systems to study the fundamental interactions of the system. This is especially true for systems on the nanometer scale. For example, an ion channel was made from a gold nanotube in order to monitor ion selectivity.<sup>1</sup> Also, single carbon nanotubes were used to mimic a single pore membrane.<sup>2</sup> These systems allow investigation of nanotube properties without the multitude of complicating factors that often accompany a biological system.

Nanotubes in biological systems have become increasingly apparent. Specifically, nanotubes have been shown to transfer surface proteins between two cells as well as intracellular transport from organelles.<sup>3,4</sup> Lipid nanotubes have been used as templates for nanometer sized optical fibers.<sup>5</sup>

Lipid nanotubes have been characterized using transmission electron microscopy,<sup>6</sup> freeze fracture electron microscopy,<sup>6,7</sup> scanning electron microscopy,<sup>8</sup> atomic force microscopy,<sup>9</sup> a lipid coalescence method,<sup>10,11</sup> and electrical conductance.<sup>11</sup> With these different means of determining the diameter of a nanotube, it would seem that these measurements would be routine. But in all but two methods of measurement; a dry and stable sample must be obtained. In the situation of a fluid system, it is very difficult to obtain a viable sample to measure the dimensions of a nanotube.

Electrochemical characterization seems ideally suited for aqueous systems due to the ability of molecules to diffuse in water. In fact, diffusion of molecules is essential in determining what electroactive species are in solution. One means of electrochemical characterization is steady state electrochemistry. Steady state electrochemistry has been used to characterize a pore leading to a nanometer sized electrode.<sup>12</sup> Also, electrochemistry has been used to measure various nanostructures through impedance measurements.<sup>2</sup>

As described in Chapters 1 - 3, a liposome model of exocytosis has been developed to ascertain the role that lipids in exocytosis.<sup>13, 14</sup> One of the important aspects of this model is the lipid nanotube that connects a small liposome or vesicle to a larger liposome, which acts as a cell membrane. Previous studies had approximated the nanotube created when soy polar extract is used to be in the 100~300 nanometer range.<sup>15</sup> This estimate was based both on video image pixel size and a calculation from a previous work by Evans and Yeung, in which the authors investigated the reaction of a liposome when a tether is pulled out from the side.<sup>16</sup> With these measurements as a basis, a more reliable means of measuring the lipid nanotube was devised.

This Chapter therefore uses steady state amperometry combined with a simple model of diffusional transport to determine the diameter of the nanotube present in the artificial liposome model of exocytosis. This nanotube acts as a fusion pore in the model and a direct comparison to the fusion pore can be made with a known nanotube diameter. To this end, I report the nanotube diameter from the steady state signal acquired by carbon fiber amperometry and some preliminary attempts to change the diameter of the lipid nanotube by altering lipid composition.

## 4.2 Materials and Methods

### 4.2.1 Liposome-Lipid Nanotube Preparation

Surface immobilized liposomes were made from soy polar extract, soy PC and Soy PE (Avanti Polar Lipids, Alabaster, AL) using a dehydration/rehydration method described previously.<sup>13</sup> All liposomes were rehydrated in 30 mM phosphate buffer (5 mM Trizma Base, 30 mM  $K_3PO_4$ , 0.5 mM EDTA adjusted to pH 7.4 with  $H_2SO_4$ ). Rehydration of dried lipid films resulted in a specific lipid conformation, a unilamellar liposome attached to a multilamellar liposome.

Once these lipids were identified a micropipette was inserted into the unilamellar liposome by means of a micromanipulator (Model MHW-3, Narishige, Inc, East Meadow, NY) with the aid of an electroporation voltage pulse, generated by a constant voltage isolated stimulator (DS2A-Mk. II, Digitimer, Inc., Hertfordshire, UK). The counter electrode for electroporation was made from a 5- $\mu$ m ProCFE (Dagan Corp, Minneapolis, MN) which is placed with a micromanipulator (Sutter MP-85, Sutter Instrument Company, Novato, CA) opposite the micropipette. The micropipette was used to inject a buffer solution, by means of a femtojet (Eppendorf / Brinkmann Instruments, Hauppauge, NY); into the unilamellar liposomes and these were inflated to approximately 50  $\mu$ m in diameter. Once the liposome was at a workable size, the liposome was manipulated by the pipette to obtain a small liposome inside the unilamellar liposome connected by a lipid nanotube. The small liposome was filled with solution containing 10 mM catechol in 30 mM phosphate buffer.

### 4.2.2 Electrochemical Recording

Carbon fibers (33  $\mu\text{m}$  diameter) were aspirated into borosilicate glass capillaries (1.2 mm O.D., 0.69 mm I.D., Sutter Instrument Co., Novato, CA) and the capillaries were pulled to tip with a commercial micropipette puller (Model P-97, Sutter Instrument Co., Novato, CA) and sealed with epoxy (Epoxy Technology, Billerica, MA). After beveling (model BV-10, Sutter Instrument Co, Novato, CA) at 85 degrees and testing in 0.1 mM catechol electrodes were placed against the liposome-nanotube junction with a micromanipulator (Model MHW-3, Narishige, Inc, East Meadow, NY). Current was held constant at 700 mV against a Ag/AgCl reference electrode with an Ensmann Instruments EI-400 potentiostat. Electrochemical data were collected at 1 kHz with a Digidata model 1322A interface and recorded with Axoscope 8.1 software (Axon Instruments, Foster City, CA).

With the nanotube in place, the 33- $\mu\text{m}$  carbon fiber electrode was placed at the nanotube-liposome junction (Figure 4.1) and was allowed to rest until the current detected by the electrode reaches a stable baseline. The baseline is recorded for one minute and at the end of one minute the small liposome was maneuvered adjacent to the larger unilamellar liposome to expel the catechol and an electrical pulse was applied to the system to remove the lipid material from the pipette. Then the pipette was returned to its previous position and once a stable baseline was obtained when the current is measured for another minute. In order to determine the amount of catechol that reaches the electrode through the lipid nanotube, the baseline from the control system was subtracted from the nanotube baseline and the difference was used to compute the diameter of the liposome.

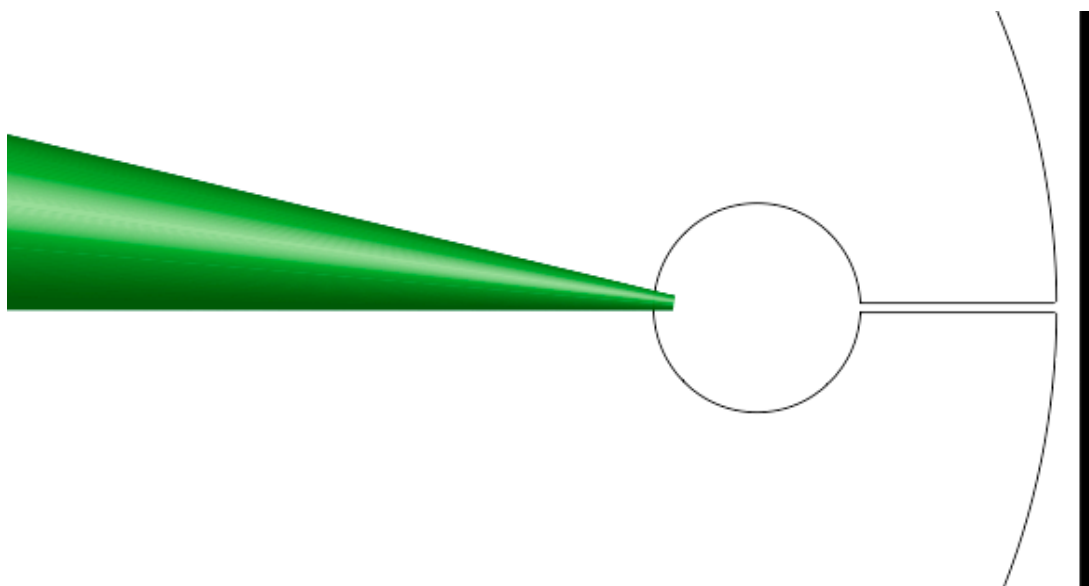


**Figure 4.1** The experimental setup for steady state electrochemical measurement of a lipid nanotube. A pipette was used to create a liposome within a liposome connected by a nanotube. Catechol diffusion was measured by a carbon fiber electrode placed at the nanotube junction with the outer vesicle. When the electrode was placed adjacent to the outside liposome intermolecular forces and the liquid double layer resulted in a 300 nm space between the electrode and the liposome. This was apparently due, in part, to the hydration of the headgroups of the lipid bilayer.

#### 4.2.3 Microscopy and Digital Video Recording

Liposome experiments were monitored using an Olympus IX-70 microscope (Olympus America, Melville, NY) with a 20x objective using differential interference contrast (DIC) polarization of the light to give a three pseudo-three dimensional appearance to the liposome. Experiments were recorded using a Sony DXC-C33 ExwaveHAD 3CCD color video camera on a Macintosh G5 personal computer (Apple Inc. Cupertino, CA) with iMovie software. Nanotube lengths were measured from digital images using Image J software (NIH, Bethesda, MD).

## 4.3 Results and Discussion

### 4.3.1 Initial Nanotube Measurements

Using a steady state amperometric measurement allows the both the nanotube diameter and effect that nanotube length has on its diameter to be determined. If it assumed that the concentration gradient of catechol is linear through the nanotube and that the effective concentration at the outer end of the nanotube is zero as it is oxidized by the electrode, then the flux of catechol through the tube is a solvable problem. By Fick's first law of diffusion (Equation 4.1) the radius of the nanotube can be determined by steady state amperometry.

$$-J(x,t) = D_R \frac{\partial C_R(x,t)}{\partial x} \quad \text{Equation 4-1}$$

In this equation,  $J$  is the molecular flux;  $D_R$  is the diffusion coefficient of the redox molecule of interest, catechol,  $\partial C_R$  is the change in concentration and  $\partial x$  the change in distance from the electrode. Assuming that the concentration gradient in the nanotube is linear then we can write Fick's first law as:

$$\frac{i}{nFA} = D \left[ \frac{dC}{dx} \right]_{x=0} \quad \text{Equation 4-2}$$

The new terms introduced into the equation are  $i$ , the current measured in the experiment,  $n$  is the number of electrons per equivalent in the oxidation of catechol,  $F$  is the Faraday constant at 96,485 coulombs/mol and  $A$  is the cross-sectional area of the electrode at the nanotube where the electrode surface is located. This assumes that the area of the electrode is the same as the cross-sectional area of the nanotube. This assumption works since the electrode is pressed in close proximity to the membrane so material eluting from the nanotube should be immediately oxidized at the electrode region closest to the

membrane. If some material diffuses radially as it elutes, then the drop in current from dilution will offset the larger apparent area making the equivalent area assumption still valid. Given this assumption, the equation can be written in terms of cross-sectional area of the nanotube and the condition of  $x=0$  (electrode surface) is dropped and we obtain equation 4.3.

$$\frac{i}{nF\pi r^2} = D \left[ \frac{dc}{dx} \right] \quad \text{Equation 4-3}$$

Solving for the radius results in equation 4.4.

$$r = \left( \frac{i}{nF\pi D \left[ \frac{dC}{dx} \right]} \right)^{\frac{1}{2}} \quad \text{Equation 4-4}$$

Equation 4.4 directly relates the radius (or diameter) of the nanotube to the current observed at an electrode placed at the nanotube when we can determine the concentration gradient and measure the oxidation current. In order to determine the current for the nanotube, the baseline or background current when no nanotube is present is subtracted from the current in the presence of the nanotube with catechol in the inner liposome. The resulting current comes only from the catechol diffusing out of the nanotube. The value  $n$  for catechol is 2, its diffusion coefficient is  $6 \times 10^{-6} \text{ cm}^2/\text{s}$  and the change in concentration over distance is determined by the catechol concentration divided by the nanotube length. These are all known constants of easily controlled parameters.

Figure 4.2 is a plot of nanotube diameter vs. tube length. The trend in the data suggests that as the length of the nanotube decreases the radius also decreases. The average tube diameter for tubes of  $4.3 \mu\text{m}$  length is  $46 \pm 12 \text{ nm}$ . This is considerably

smaller than earlier predictions. This result is important as it suggests that for situations like that in exocytosis; the artificial liposome model might be a better approximation of a fusion pore diameter than previously thought.

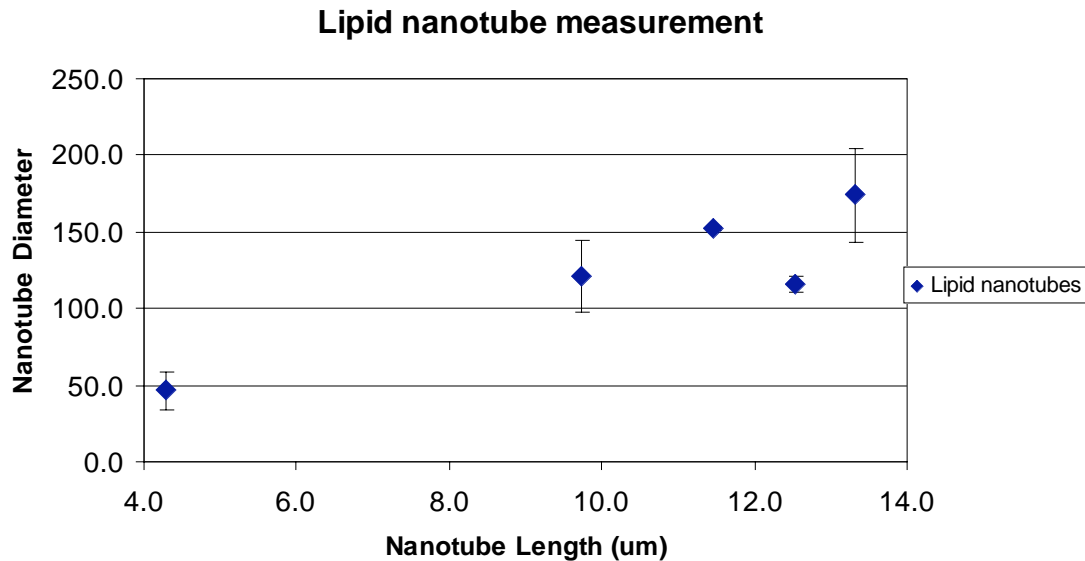


**Figure 4.2** A plot of the measured nanotube diameter vs. the nanotube length and as the length of the nanotube increase so does the diameter of the tube. The diameter of the tube seems to be dependant upon the total length of the tube.  $n = 3$

In order to better understand the forces at work within the artificial liposome model it is important to know the diameter of the lipid nanotube. As the nanotube length decreases due to vesicle swelling, it becomes a more perfect mimic of the fusion pore. On some occasions the fusion pore is stable enough to allow neurotransmitter out of the fusion pore before a full fusion takes place. This has been recorded by amperometry and manifests itself a small plateau, termed a “foot,”<sup>17-19</sup> just prior to a full fusion event. Also, in a static state our model is similar to “kiss and run” exocytosis, a naturally occurring event.<sup>19, 20</sup> This event entails a fusion pore forming between a vesicle and the plasma membrane and neurotransmitter being forced of the fusion pore. Before the vesicle can

fully fuse with the membrane the fusion pore closes. The liposome model can mimic these situations and with the nanotube dimensions make direct comparisons with biological systems.

### **4.3.2 Effect of Changing Liposome Composition on Nanotube Diameter**

As has been shown in Chapter 3, changes in lipid composition change the overall behavior of a membrane in terms of the rate of exocytosis. Using the results presented in the previous chapter as a guideline, the soy liposomes were augmented with 25 % soy PC or 25 % soy PE and the experiment to determine nanotube diameter carried out. Changing the headgroup composition of the liposome resulted in a definite difference in release characteristics as measured by amperometry (Chapter 3), so I predicted that the diameter of the nanotube would change with the different headgroups. With this in mind, steady state amperometric measurements were carried out at both the PC and PE enriched liposomes. As PC prefers structures with less curvature, it was expected that an increase in PC would result in a larger nanotube diameter. Conversely, an increase in PE was expected to result in a smaller diameter nanotube as PE prefers more highly curved structures. However, when plotting the results with the previous control experiments, there is no clear trend observed (Figure 4.3) for the different composition membranes. These data make it appear that if there are differences, they are too small to be quantified within experimental error.

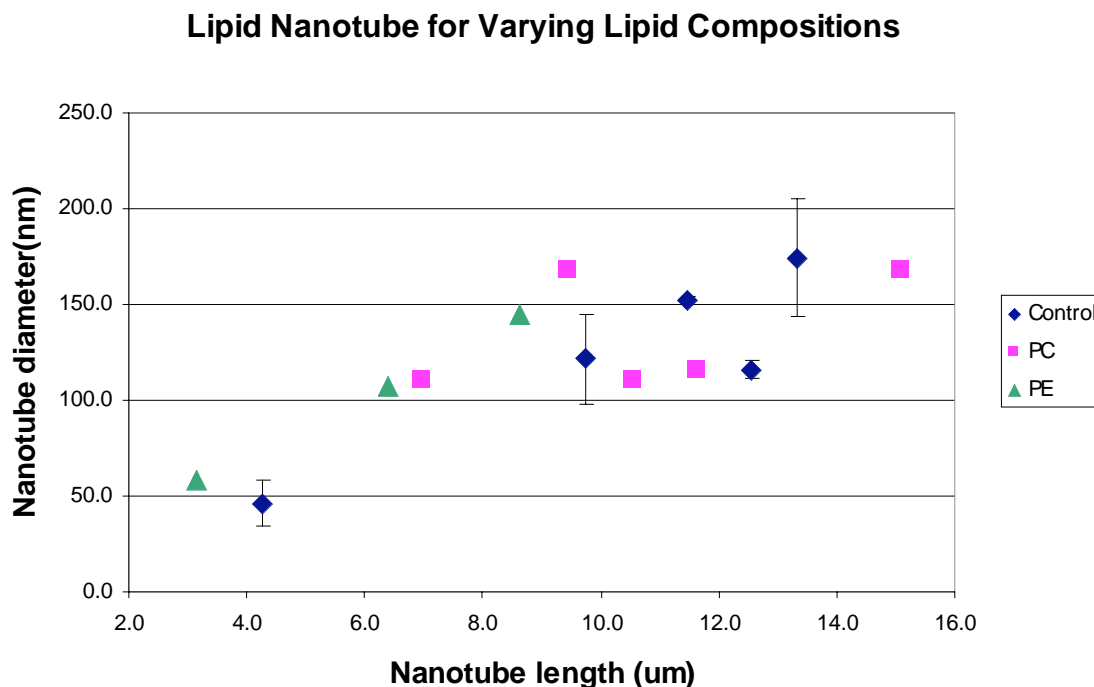


**Figure 4.3** Graph of various lipid compositions and the measured diameters. No noticeable difference is seen between the different compositions.  $n$  for control = 3 and  $n$  for PC and PE = 1.

With the implications that nanotube size is independent of lipid composition, it stands to reason that there are other factors which govern the diameter. It is possible that the constraints of system allow for little variation in the composition of the nanotube, or that the small size lacks the necessary amount of material to have a noticeable change in diameter. It appears from these data that nanotube length has a larger effect on the diameter than lipid composition. It is possible that the composition of the nanotube is different than the bulk liposome composition and this might be dictated by the length and diameter. Thus the tube might draw in the right proportion of lipids to meet the diameter. This could be tested with liposomes completely lacking PE or PC, but these liposomes are difficult to make and have not yet been shown to make liposome-nanotube networks.

#### 4.4 Conclusions about Lipid Nanotube Measurements

In this Chapter I have presented a method to electrochemically measure the inner radius (diameter) of lipid nanotubes in the artificial liposome model of exocytosis. For short nanotubes, the diameter is on the order of 50 nm. This should allow us to develop a better understanding of the forces that are at work in the lipid system. Experiments to this point to try to determine the extent to which lipid composition controls the diameter of the tube have shown that large changes (25 %) in composition do not appear to have a significant effect. Overall, these results lay the groundwork for future experiments to understand the parameters controlling release of neurotransmitters through a small lipid pore that is similar to the fusion pore formed between the vesicle and the cell membrane during the early stages of exocytosis.

#### 4.5 Literature Cited

- (1) Harrell, C. C.; Kohli, P.; Siwy, Z.; Martin, C. R. *J. Am. Chem. Soc.* **2004**, *126*, 15646-15647.
- (2) Sun, L.; Crooks, R. M. *J. Am. Chem. Soc.* **2000**, *122*, 12340-12345.
- (3) Onfelt, B.; Nedvetzki, S.; Yanagi, K.; Davis, D. M. *J Immunol* **2004**, *173*, 1511-1513.
- (4) Polishchuk, E. V.; Di Pentima, A.; Luini, A.; Polishchuk, R. S. *Mol. Biol. Cell* **2003**, *14*, 4470-4485.
- (5) Gopakumar Gopalakrishnan, J.-M. S. D. S. C. G. M. G. R. H. K. J. S. P. A. S. H. V. *Angewandte Chemie International Edition* **2005**, *44*, 4957-4960.
- (6) Polidori, A.; Michel, N.; Fabiano, A. S.; Pucci, B. *Chemistry and Physics of Lipids* **2005**, *136*, 23.
- (7) Ulrike Lauf, A. F. K. W. A. S. U. *ChemPhysChem* **2004**, *5*, 1246-1249.
- (8) Brazhnik, K. P.; Vreeland, W. N.; Hutchison, J. B.; Kishore, R.; Wells, J.; Helmerson, K.; Locascio, L. E. *Langmuir* **2005**, *21*, 10814-10817.
- (9) Kameta, N.; Masuda, M.; Minamikawa, H.; Shimizu, T. *Langmuir* **2007**, *23*, 4634-4641.

- (10) Cuvelier, D.; Derenyi, I.; Bassereau, P.; Nassoy, P. *Biophys. J.* **2005**, *88*, 2714-2726.
- (11) Tokarz, M.; Hakonen, B.; Dommersnes, P.; Orwar, O.; Akerman, B. *Langmuir* **2007**, *23*, 7652-7658.
- (12) Zhang, B.; Zhang, Y.; White, H. S. *Anal. Chem.* **2006**, *78*, 477-483.
- (13) Cans, A.-S.; Wittenberg, N.; Karlsson, R.; Sombers, L.; Karlsson, M.; Orwar, O.; Ewing, A. *PNAS* **2003**, *100*, 400-404.
- (14) Cans, A. S.; Wittenberg, N.; Eves, D.; Karlsson, R.; Karlsson, A.; Orwar, O.; Ewing, A. *Anal. Chem.* **2003**, *75*, 4168-4175.
- (15) Karlsson, M.; Sott, K.; Cans, A. S.; Karlsson, A.; Karlsson, R.; Orwar, O. *Langmuir* **2001**, *17*, 6754-6758.
- (16) Evans, E.; Yeung, A. *Chemistry and Physics of Lipids* **1994**, *73*, 39.
- (17) Chow, R. H.; von Ruden, L.; Neher, E. *Nature* **1992**, *356*, 60.
- (18) Sombers, L. A.; Hanchar, H. J.; Colliver, T. L.; Wittenberg, N.; Cans, A.; Arbault, S.; Amatore, C.; Ewing, A. G. *J. Neurosci.* **2004**, *24*, 303-309.
- (19) Staal, R. G. W.; Mosharov, E. V.; Sulzer, D. *Nature Neuroscience* **2004**, *7*, 341 - 346.
- (20) Burgoyne, R. D.; Fisher, R. J.; Graham, M. E.; Haynes, L. P.; Morgan, A. *Biochem. Soc. Trans.* **2001**, *29*, 467-472.
- (21) Anderson, B. B.; Zerby, S. E.; Ewing, A. G. *Journal of Neuroscience Methods* **1999**, *88*, 163.

## Chapter 5

### Fabrication and Characterization of Carbon Fiber Microelectrode Arrays

#### 5.1 Introduction

Fabrication and characterizations of a carbon fiber multi-electrode array (MEA) has been undertaken. Carbon fiber MEAs are comprised of multiple microdisk electrodes embedded in multiple glass capillaries, the radii of each microdisk being  $2.5\ \mu\text{m}$  (Figure 5.1). The diameter of the whole electrode array ranges from  $10\ \mu\text{m}$  to  $20\ \mu\text{m}$ , depending on the number of microelectrodes in the array.

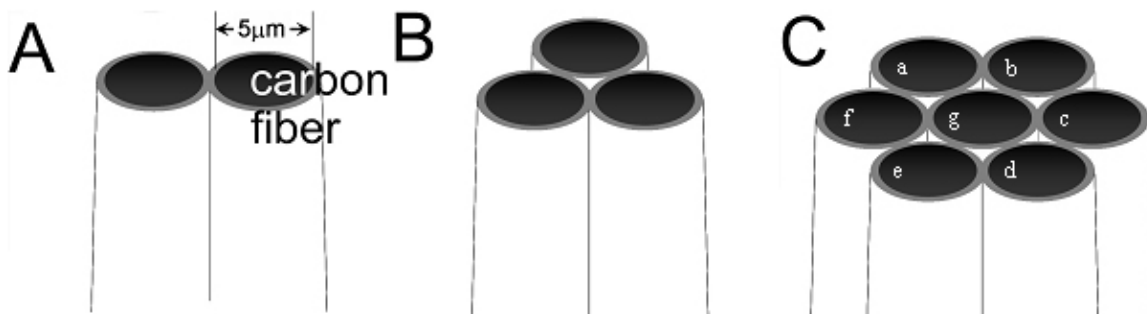


**Figure 5.1** A schematic drawing of the carbon fiber MEAs containing two (A), three (B), and seven (C) microdisks.

There has long been interest in constructing ultra-small electrochemical sensors to study chemical and biochemical processes in space-limited environments.<sup>1-5</sup> A typical experiment monitors the exocytotic release from single neuronal cells.<sup>6-16</sup> Previous studies of cell-secretion focused on a single carbon fiber electrode, which possesses a zepto-molar limit of detection and gives kinetic information about single exocytotic events due to its sub-millisecond time resolution. However, it is difficult to obtain sub-

cellular spatial information using a single electrochemical probe. The study of sub-cellular distribution of exocytotic events can, however, be facilitated by simultaneous amperometric recording from multiple electrochemical sensors placed on the cell. Array-based ultra-micro electrochemical sensors offer great promise for this type of application.<sup>17, 18</sup>

MEAs have been intensely studied in the past two decades not only for chemical information,<sup>19</sup> but also to probe neuronal communications in a brain or a tissue slice,<sup>20, 21</sup> and in cultured networks of neuronal cells.<sup>22, 23</sup> MEAs have also been used in a variety of studies, including drug discovery,<sup>24, 25</sup> diffusion of chemical species in solid electrolyte and electrolyte solutions,<sup>26, 27</sup> and chemical and biochemical sensing.<sup>28-34</sup> Micro-fabrication technologies have been widely applied in the fabrication of MEAs.<sup>35-47</sup> Alternative techniques have also been developed to construct electrochemical sensors in an array format. Examples include chemical or electrochemical deposition of metals in nanoporous or microporous materials (polymers<sup>48-52</sup> or glass<sup>53, 54</sup>), chemical etching<sup>55, 56</sup> or micro-patterning<sup>57</sup> on metal-supported self-assembled monolayers (SAMs), and chemically attaching metal nanoparticles onto SAMs at the electrode surface.<sup>58</sup>

Individually addressable microelectrode arrays offer many advantages compared to their counter parts, such as high spatial resolution, multiple analyte detection and probing signal transmissions in a network of biological cells. The Michael group reported a method of constructing two or four individually addressable carbon ultra-microelectrodes (radii  $\sim 1 \mu\text{m}$ ) separated by a distance  $\sim 15 \mu\text{m}$ .<sup>59</sup> Each carbon fiber was etched into a sharp tip and then electrically separated by coating the tip with poly (allylphenol). The electrochemical sensor arrays were applied to probe dopamine release

from the brain at multiple sites. The Lindau group recently reported the use of a microfabricated chip containing an array of four metal-film electrodes to probe exocytosis from single chromaffin cells.<sup>17, 18</sup> The adjacent electrodes were  $\sim 2 \mu\text{m}$  apart with a  $\sim 5 \mu\text{m}$  circular empty space in the center of the array.

Herein is presented the fabrication and characterizations of micrometer-sized electrochemical probes containing closely-packed arrays of carbon microdisk electrodes, comparable in size to individual neuronal cells (10-20  $\mu\text{m}$ ). The fabrication of MEAs containing two, three and seven carbon fibers were demonstrated as well as microscopic and electrochemical characterization. The steady-state voltammetric response and numerical simulations were compared using two-fiber MEAs to study the overlap of diffusion profiles between adjacent microelectrodes and the effect of this overlap on the measurements at individual microelectrodes. Electrodes were also characterized with flow analysis to determine the response of each microelectrode in the array to transient changes in local concentration of chemical species. This work was carried out as a collaboration with an electrochemistry postdoc in the lab, Bo Zhang.

## 5.2 Materials and Methods

### 5.2.1 Chemicals

KCl (99.9% Aldrich) and Ferrocene Methanol ( $\text{FcCH}_2\text{OH}$ , 100%, Aldrich) were used as received. All solutions were made using 18  $\text{M}\Omega\cdot\text{cm}$  from a Millipore water purification system.

### 5.2.2 Fabrication of Carbon Fiber MEAs

Fabrication of carbon fiber MEAs was adapted from the construction of single carbon fiber microelectrodes.<sup>60-62</sup> A single 5- $\mu\text{m}$ -diameter carbon fiber (Amoco, Greenville, SC) was inserted into each barrel of a multi-barrel glass capillary (2B150F-4, 3B120F-4, 7B100F-4, World Precision Instruments). Multiple 12-cm-long pieces of 5- $\mu\text{m}$  carbon fiber were isolated from a bundle and laid on a piece of white paper with one end immobilized with Scotch tape. One of them, from the free end, was then aspirated into a home-pulled thin glass capillary ( $\sim 0.4$  mm o.d.,  $\sim 30$  cm long) connected to an in-house vacuum, which was pre-inserted into one barrel of the multi-barrel glass capillary. The thin glass capillary was then pulled back with the fiber left in the multi-barrel glass capillary. This step was repeated until each barrel was filled with a single carbon fiber.

The multi-barrel glass capillary was then pulled using a commercial glass puller (P-97, Sutter Instrument). The pulled electrode tip was checked under an optical microscope to ensure the fibers were uniform inside the pulled glass tip. To ensure a good seal between the glass and fiber, the pulled electrode was dipped into a freshly made epoxy (Epo-Tek, Epoxy Technology, Billerica, MA) for  $\sim 5$  min and cured in an oven ( $100$  °C) for  $>24$  hours. The electrode tip was cut and polished on an abrasive surface (BV-10, Sutter). Each barrel was then back-filled with silver paint (SPI Inc.) and an electrical connection was made using a tungsten microrod placed in each barrel. Epoxy was applied to secure the tungsten rods to the glass.

### **5.2.3 Electrochemical Apparatus**

A one-compartment, two-electrode cell was employed with the cell and preamplifier in a homebuilt Faraday cage. A Ag/AgCl electrode was used as the reference/auxiliary electrode. Four bipotentiostats (EI-400, Ensmann) were used for multi-channel voltammetric measurements: The triangle wave signal was applied from one potentiostat and this potentiostat had its ground connected to the other three potentiostats. The potentiostats were interfaced to a PC through a multi-channel data acquisition system (Digidata 1440A, Molecular Devices). Voltammetric responses were plotted using Origin<sup>®</sup> 7.5 (OriginLab<sup>®</sup>).

### **5.2.4 Scanning Electron Microscopy**

SEM images of the carbon fiber MEAs were obtained using a FEI Quanta 3D 200 FIB/SEM at the PennState Nanofabrication facility.

### **5.2.5 Finite-Element Simulations**

The steady-state voltammetric response of a double-fiber-array microelectrode was simulated using Comsol software (Comsol, Inc.) on a PC.

## 5.3 Results and Discussion

### 5.3.1 Fabrication of Carbon Fiber MEAs

As illustrated in Figure 5.1, the carbon fiber MEAs are arrays of closely-packed carbon microdisk electrodes insulated in thin glass. The geometry of the electrode is determined by four important processes in the preparation of carbon fiber MEAs: multi-barrel glass capillary selection, carbon micro-fiber size, cutting and polishing the electrode.

The fabrication of carbon fiber MEAs is initialized by choosing a multi-barrel glass capillary. The number and the arrangement of the microelectrode included in the array are pre-selected by using different multi-barrel glass capillaries. The commercially available products are limited to two, three, five, and seven-barrel glass capillaries. Thus, the number of microelectrodes one can make in a carbon fiber MEA is typically 2, 3, 5, or 7. The MEAs fabricated in the present research contain exclusively 5- $\mu\text{m}$ -diameter carbon fibers. However, other carbon fibers can also be used to generate MEAs of different size.

The control of the distance between different electrodes is important for the preparation of MEAs.<sup>60-65</sup> Due to the conical or tapered shape of the pulled electrode tip, this inter-electrode separation (center-center) can be precisely controlled during electrode polishing. The more the overall electrode material is beveled away, the larger the inter-electrode distance. Thus, MEAs with inter-electrode distance from 6 to 100  $\mu\text{m}$  have been constructed. Good insulation is maintained with adjacent fibers separated by sub-

$\mu\text{m}$ -thick glass due to the ultra-high resistivity of the glass material ( $> 10^{14} \Omega\cdot\text{m}$  for borosilicate glass).<sup>66</sup>

### 5.3.2 Scanning Electron Microscopy.

Figure 5.2A-C show SEM images of a two-fiber, three-fiber, and seven-fiber MEA, respectively. From the images, it is apparent that the electrodes are structurally well defined. The pattern of the carbon microdisks in the 2-D array copies the pattern of the multi-barrel glass capillaries. The  $2.5\text{-}\mu\text{m}$ -radius carbon disks are tightly packed together and surrounded by thin glass, on the order of  $1 \mu\text{m}$ . One can estimate from the images that the diameter of the three-fiber and seven-fiber arrays is in the range of  $15\text{-}20\mu\text{m}$ , close to the size of the single neuronal-like PC12 cells that will be the eventual target of these electrochemical probes. Another interesting property is that the electrode surface area is  $>60\%$  of the total area in the 2-D array.

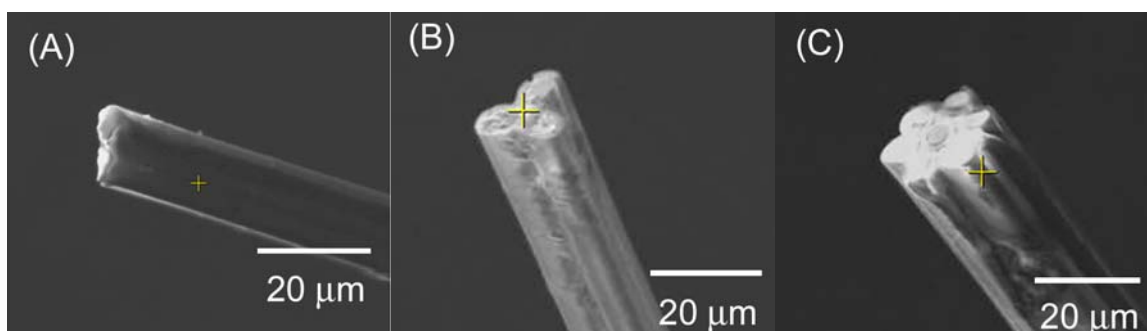


**Figure 5.2** Scanning Electron Microscopy of carbon fiber MEAs having two (A), three (B), and seven (C) microdisks. Data collected by Bo Zhang.

### 5.3.3 Steady-State Voltammetric Response of the Two-Fiber MEAs

Figure 5.3 shows the steady-state voltammetric response at 10 mV/s of a double microelectrode array in an aqueous solution containing 1 mM FcCH<sub>2</sub>OH and 0.2 M KCl. The radius of the carbon fiber disk is 2.5- $\mu$ m, with an inter-electrode distance (center-center),  $d = \sim 6.5 \mu\text{m}$ . Figure 5.3A and 5.3A display the individually measured voltammetric response of the two microelectrodes, A and B, respectively. Only one electrode is measured at a time, the other being unconnected. Figure 5.3C shows the steady-state voltammetric response when both electrodes are connected together.

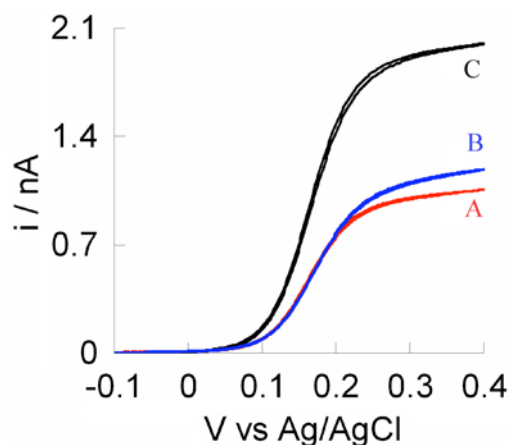


**Figure 5.3** Steady-state voltammetric response at 10 mV/s of a two-fiber MEA in 1 mM FcCH<sub>2</sub>OH containing 0.2 M KCl. (A) and (B) show the voltammetric response of individual microelectrode 1 and 2, respectively, and (C) is the voltammetric response of the two microelectrodes together. Specific data in this figure collected by Bo Zhang

For a disk-shape microelectrode embedded in an infinite thick insulating material, the steady-state limiting current,  $i_d$ , is described using the following equation,<sup>67</sup>

$$i_d = 4nFDC^*a$$

Equation 5-1

where  $n$  is the number of electrons transferred per molecule,  $F$  is the Faraday constant,  $D$  is the diffusion coefficient,  $C^*$  and  $a$  are bulk concentration of the redox molecule and the radius of the microelectrode, respectively. In the case of carbon fiber MEAs, the glass thickness is less than the radius of each carbon fiber microelectrode. The measured steady-state limiting current is in fact much larger than predicted using Equation 1. The predicted limiting current,  $i_d$ , using Equation 1, is 753 pA for a 2.5- $\mu\text{m}$ -radius disk microelectrode in 1 mM FcCH<sub>2</sub>OH when a diffusion coefficient of  $D = 7.8 \times 10^{-6} \text{ cm}^2/\text{s}$  is used in the calculation.<sup>68</sup>

However, the measured limiting currents are 1100 and 1020 pA for electrode A and B, respectively, which are ~46% and ~35% larger than predicted. Since the glass is much thinner than the dimension of the electrode, we believe that the difference in limiting current is due to the underestimated diffusive flux of redox molecule from the bulk to the electrode, including solution from behind the plane of the electrode. In this perspective, the steady-state voltammetric response of a carbon fiber microelectrode is better described using the equation for a hemispherical microelectrode<sup>69</sup>

$$i_d = 2\pi n F D C^* a \quad \text{Equation 5-2}$$

where the only difference is a larger constant,  $2\pi$ , as compared to 4 in equation 1. The computed limiting current,  $i_d$ , is 1180 pA using equation 2, in good agreement with what is measured at each carbon microelectrode.<sup>70</sup>

Figure 5.3C shows the overall steady-state voltammetric response of the two carbon fibers measured when they are connected together. The limiting current in Figure

5.3C is in fact ~15% smaller than the sum of the limiting currents of the two fibers measured one at a time. Experiments and numerical simulations have shown that the voltammetric response of a 2-D microdisk electrode array is largely affected by their inter-electrode distances: when microdisks are well separated, they behave like individual electrodes; when they are too close to each other, their diffusion profiles overlap and they exhibit behavior similar to a macroelectrode.<sup>60-65</sup>

The effect of inter-electrode distance,  $d$ , on the steady-state limiting current of a two-fiber MEA is quantitatively understood by both steady-state electrochemical measurements and numerical simulations. Table 5.1 lists the reduction of steady-state limiting current at a two-fiber MEA as a function of inter-electrode distance,  $d$ , where  $d$  has been normalized with the radius of the microdisk electrode. All the voltammetric responses were obtained in 1 mM FcCH<sub>2</sub>OH and 0.2 M KCl, using a sweep rate  $v = 10$  mV/s. The normalized inter-electrode spacing,  $d/a$ , has been varied from 2.4 (2 is the theoretical minimum of  $d/a$ ) to 28. The limiting current measured at a single carbon fiber disk (e.g.,  $i_A$  or  $i_B$ ) varies among different electrodes. Specifically, it decreases when inter-electrode distance is increased. The decrease in limiting current is ascribed to the hindered diffusion of redox molecules as the thickness of the insulating material is increased. The overall limiting current at the two-fiber MEA is normalized by the sum of the individually measured limiting current. Also listed in Table 5.1 are the results from numerical simulations. Details of the simulation are given below.

**Table 5.1 Steady-State Limiting Current at a two-Fiber MEA as a Function of the Inter-Electrode Spacing.**

Experimental Data

$d / \mu\text{m}^a$	$d / a$	$i_A / \text{nA}^b$	$i_B / \text{nA}^c$	$(i_A + i_B) / \text{nA}^d$	$i_{AB} / \text{nA}^e$	$i_{AB} / (i_A + i_B)$
6.0	2.4	1.20	1.06	2.26	2.00	0.88
10.0	4.0	0.94	1.00	1.94	1.78	0.92
13.0	5.2	0.82	0.87	1.69	1.60	0.95
20.0	8.0	0.80	0.68	1.48	1.44	0.97
30.0	12.0	0.70	0.69	1.39	1.37	0.98
70.0	28.0	0.82	0.85	1.67	1.66	0.99

Numerical Simulation

6.0	2.4	0.83	0.83	1.66	1.39	0.84
10.07.0	4.02.8	0.830.83	0.840.83	1.671.66	1.501.44	0.900.87
15.010.0	6.04.0	0.840.83	0.840.84	1.681.67	1.581.50	0.940.90
25.015.0	10.06.0	0.840.84	0.840.84	1.681.68	1.621.58	0.970.94
55.025.0	22.010.0	0.840.84	0.840.84	1.681.68	1.641.62	0.980.97
55.0	22.0	0.84	0.84	1.68	1.64	0.98

<sup>a</sup>  $d$  is the inter-electrode distance. <sup>b, c</sup>  $i_A$ ,  $i_B$  are the steady-state limiting currents at electrode A and B measured one at a time, respectively. <sup>d</sup> The sum of limiting current at each electrode A and B. <sup>e</sup> The total limiting current at the two-fiber array electrode. Data collected by Bo Zhang.

### 5.3.4 Finite-Element Simulation of Steady-State Limiting Current at a Two-Fiber MEA.

The numerical simulation of limiting current was accomplished in 3-D using a pure diffusion model (using Comsol software Ver. 3.2, Comsol Inc.). In the simulation, the radii ( $a = 2.5 \mu\text{m}$ ) and the length ( $100 \mu\text{m}$ , 40x larger than  $a$ ) of the microdisk electrodes were held constant. The inter-electrode distance was varied. A  $500 \mu\text{m}$  (200x larger than  $a$ ) cubic box was assumed as the electrochemical cell, in which the

concentration of redox species at the surface of cubic box (1 mM) and at the electrode surface (0 mM) were held constant. For simplicity, the thicknesses of the insulation material surrounding and between the two microdisks were not considered, which might give a slightly larger simulated current. However, it appears that this will not greatly affect the analysis of the crosstalk between the two microelectrodes. The steady-state limiting current was simulated as a function of the normalized distance,  $d/a$ .

The simulated current is in fair agreement with the experimental result. Table 5.1 shows that in each case the simulated steady-state limiting current at each individual microdisk is about 75% of its corresponding experimental value. The reason for the smaller simulated values could be attributed to mesh size in the simulation. The mesh is the software convention of breaking up the area of analysis into smaller pieces. The software is solving the Navier-Stokes equation for the simulation and it is easier for the software to solve the equation with small finite areas or meshes. As the mesh size decreases the approximation is better but also the amount of memory required for the calculation increases. The minimum mesh size at the electrode surface was about 3-10% the size of the electrode and a smaller simulation mesh was not possible due to insufficient memory.

The normalized steady-state current from the simulation is in agreement with the experimental data. Figure 5.4 shows a comparison of the experimental and the simulated data of the normalized steady-state limiting current at a 5- $\mu\text{m}$  two-fiber MEA,  $i_{AB} / (i_A + i_B)$ , as a function of the normalized inter-electrode distance,  $d/a$ , in 1 mM FcCH<sub>2</sub>OH and 0.2 M KCl. In Figure 5.4,  $i_{AB}$ ,  $i_A$ , and  $i_B$  are the steady-state limiting current at the two carbon fiber microdisks connected together, at electrode A (B not connected), and at

electrode B (A not connected), respectively. The blue triangles are experimental data and the red diamonds are from numerical simulations. A line is drawn through the diamonds to best fit the simulated data and it is apparent that as the inter-electrode distance is increased, the normalized current goes to unity. The simulation and experiment both show that when  $d/a$  is  $\sim 5$ , or the inter-electrode distance is 5 times larger than the radius of the electrode, the limiting current at the two-fiber MEA is about 95% of the total current of the two individual electrodes. In other words, when the distance between two microdisk electrodes is  $>5$  times of the radii of the electrodes, they behave independently. This result can be used to predict the minimum inter-electrode distance in an array of carbon fiber microdisk electrodes needed to acquire independent steady-state electrochemical behavior.

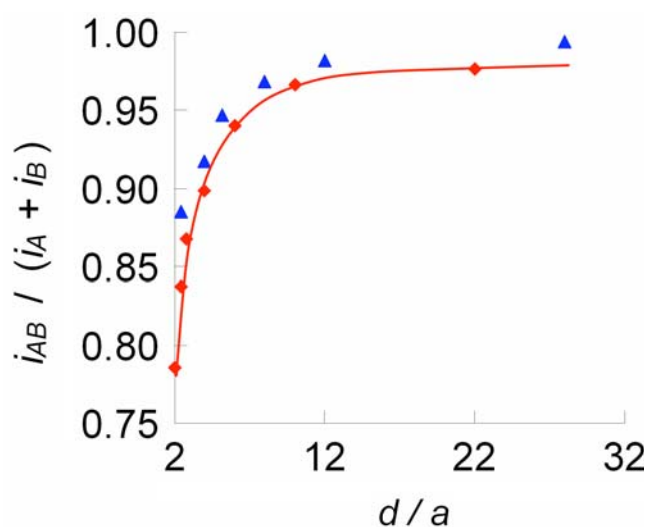


**Figure 5.4** The ratio of the steady-state limiting current of two microelectrodes measured together and the sum of each individually-measured limiting current of the two-fiber MEA as a function of the normalized inter-electrode distance,  $d/a$ . Data collected by Bo Zhang.

Cross talk between adjacent electrodes can be qualitatively understood with computer simulations of the spatial distribution of redox flux as well. Figure 5.5 displays the simulated cross-sectional distribution of the steady-state flux of the redox molecules

(1 mM FcCH<sub>2</sub>OH) near the electrode surface. Figure 5.5A-D shows the distribution of steady-state flux as a function of the inter-electrode distance. The overlap of the flux of redox molecules from bulk solution to the two microdisks is clearly observed when  $d$  is small compared to the radius of the electrode ( $d/a = 2.4$ ), as shown in Figure 5.5A. It is small but still noticeable when  $d/a$  is 4, as shown in 5.5B. However, when  $d$  becomes even larger, as displayed in Figure 5.5C and 5.5D, there is no overlap shown in the simulated data. And the steady-state electrochemical behaviors of the two microelectrodes are unaffected by each other, as shown in Figure 5.4.

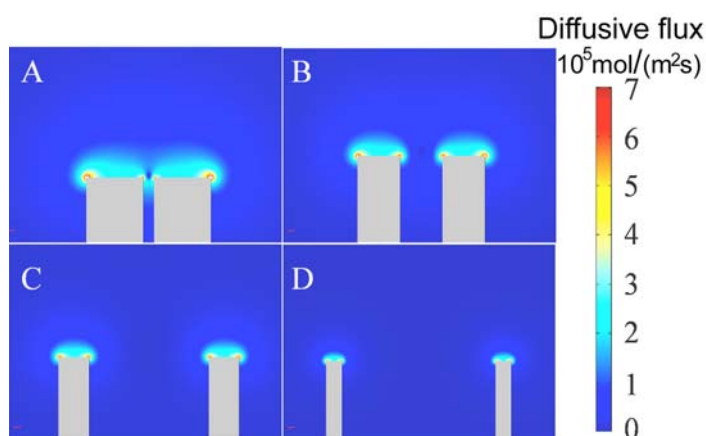


**Figure 5.5** Simulated distribution of steady-state diffusive flux at the cross section of a 5- $\mu\text{m}$  two-fiber MEA as a function of the inter-electrode distance. The distances are (A) 6, (B) 10, (C) 25, and (D) 50  $\mu\text{m}$ , respectively. Data collected by Bo Zhang.

### 5.3.5 Voltammetric Response of the Seven-Fiber MEA

Steady-state and fast-scan voltammetry were applied to characterize a seven-fiber MEA. From an optical microscopy image (not shown) it was determined that the electrode has a  $\sim 20 \mu\text{m}$  total diameter which is consistent with an inter-electrode distance of  $\sim 7 \mu\text{m}$ . Figure 5.6A-G shows the steady-state voltammetric response of each carbon

fiber (refer to Figure 5.1 C for the relative position of each microfiber in the array) measured simultaneously at 20 mV/s in 1 mM FcCH<sub>2</sub>OH and 0.2 M KCl. Each voltammetric response is well defined and has an ideal sigmoidal shape at this scan rate. The steady-state limiting current at each microfiber is about the same, except for the center fiber (Figure 5.6G). Close inspection of Figure 5.6 indicates that the diffusion limited steady-state current at the center fiber is ~40% smaller than that of the microfibers at the edge, and the limiting current at the edge fibers is ~610 pA, which is 48% smaller than what is predicted using Equation 2. This result shows a strong overlapping of the diffusion profile for this electrode with the surrounding electrodes as expected.

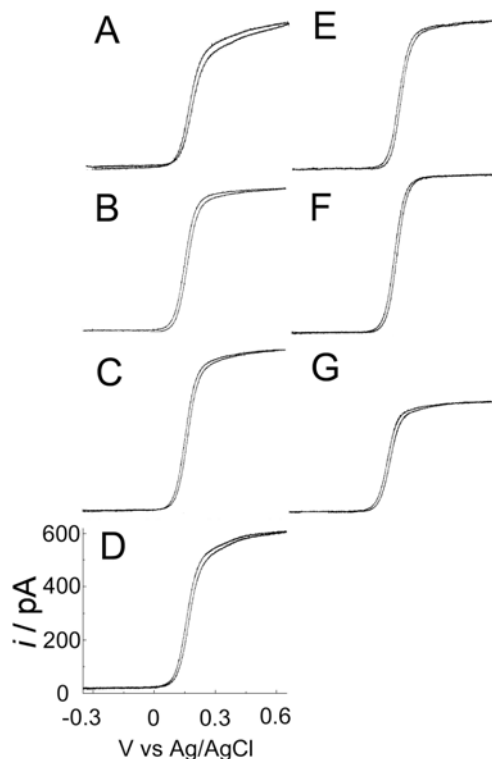


**Figure 5.6** Steady-state voltammetric response at 20 mV/s of a seven-fiber MEA in 1 mM FcCH<sub>2</sub>OH and 0.2 M KCl. (A) through (G) are the voltammetric response of individual microelectrodes A through G. Data collected by Bo Zhang.

Figure 5.7A-G shows the fast-scan voltammetric response of the same seven-fiber MEA at 300 V/s in 1 mM FcCH<sub>2</sub>OH and 0.2 M KCl. On top of the capacitive charging current are two peaks corresponding to oxidation and reduction of the redox molecules, FcCH<sub>2</sub>OH and FcCH<sub>2</sub>OH<sup>+</sup>, respectively. The averaged double-layer charging current is ~3 nA, which corresponds to a double-layer capacitance ~10 pF on each fiber disk (~51 μF/cm<sup>2</sup>). Inspection of Figure 5.7A through 5.7G reveals that the peak currents for electrode A through G are approximately the same, ~3 nA. No significant difference is found in the fast-scan voltammetric response at the center carbon microdisk (e.g., Figure 5.7 G) since the voltammetric current is mainly due to the molecules adjacent to the electrode surfaces at this scan rate and diffusion from the edge is not significant.<sup>70</sup>

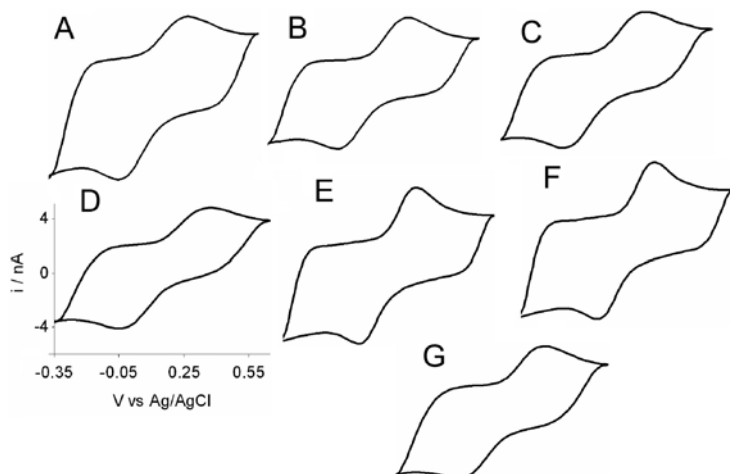


**Figure 5.7** Fast-scan voltammetric response at 300 V/s of the same seven-fiber MEA in 1 mM FcCH<sub>2</sub>OH and 0.2 M KCl. (A) through (G) are the voltammetric response of individual microelectrodes A through G. No background subtraction was applied. Data collected by Bo Zhang.

### 5.3.6 Flow-Cell Characterization of the Triple MEA

Some analytical applications require that the microsensors respond to multiple transient signals. Examples include fast-scan voltammetric detection and amperometric

sensing of neuronal transmitters from single biological cells and cells in a network and the electrochemical detection of easily oxidizable/reducible molecules in chemical separations. The individual addressability and long term stability of the sensor arrays are both important in those applications.

The three-fiber MEAs were characterized using a flow-cell type experiment, as illustrated in Figure 5.8A. A  $\sim 5 \mu\text{m}$  micropipette containing 1 mM FcCH<sub>2</sub>OH and 0.2 M KCl was perpendicularly positioned in a close proximity to the electrode tip of a triple MEA held in a 0.2 M KCl solution. A constant potential ( $V_{app} = 500 \text{ mV}$ ) was applied at each microelectrode using three potentiostats. A microinjector (Picospitzer III, Genral Valve) was used to apply a short term pulse of redox solution to the electrode surface, which was then electrochemically detected at each carbon fiber. A schematic drawing of the current-time response at each electrode is given in Figure 5.8B.  $\tau$  is the time period of the application of flux which was varied from 1 to 5 s. The injection velocity under the experimental conditions has been estimated to be  $\sim 10 \text{ nL/s}$ .

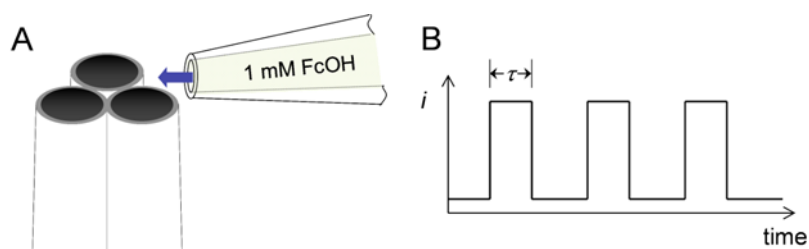


**Figure 5.8** (A) Schematic depiction of the flow-cell characterization of the three-fiber MEA. A constant potential (400 mV vs Ag/AgCl) is applied on each individual microelectrode. A glass micropipette is held perpendicular to the microelectrode tip and is applied to inject solution (1 mM FcCH<sub>2</sub>OH) onto the electrode for a period of time,  $\tau$ . (B) A schematic drawing of the current-time response at each microelectrode as a function of the application of transient injection of redox solution. Artwork by Bo Zhang.

Figure 5.9A through 5.9C show a series of representative amperometric responses of the flux of FcCH<sub>2</sub>OH at the three-fiber MEA when  $\tau$  was 1, 2, 5 s, respectively. Figure

5.D shows the response from the same electrode when  $\tau$  was varied consecutively in one recording. Each pulse of redox solution gives a square pulse of oxidation current at each microelectrode. The length of the current pulse is approximately the same as the length of time period that the solution is injected. The results show that each microelectrode in the MEAs is individually addressable and responds to the transient change in the concentration of the oxidizable/reducible species.

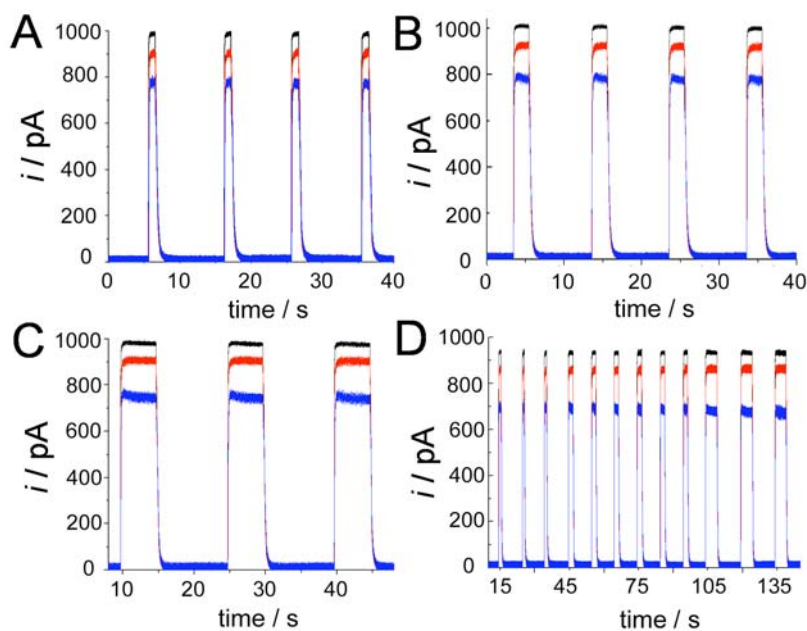


**Figure 5.9** Amperometric response at each microelectrode of a three-fiber MEA after multiple injections of 1 mM FcCH<sub>2</sub>OH solution onto the electrode. (A)  $\tau = 1$  s, (B)  $\tau = 2$  s, (C)  $\tau = 5$  s, and (D)  $\tau$  is varied from 1 to 5 s in one experiment. Data collected by Bo Zhang.

Close inspection of Figure 5.9 shows that the current pulse at one electrode is smaller than the other two. This might be caused by either different electrode activity or by further dilution of redox solution. The current at each electrode increases at almost the same time as the redox pulse. However, the smallest pulse increases at a slightly later time ( $\sim 0.1$  s) than the other higher pulses indicating that it is placed further away from the injection pipette.

#### 5.4 Summary for Carbon Fiber Multi Electrode Arrays

Carbon fiber MEAs have been fabricated that are potentially applicable for probing chemical changes in tight spaces, such as studying exocytosis from single biological cells and chemical detection inside ultra-small glass capillaries. Electron microscopic characterization show that these micro-sensor arrays are geometrically well-defined, on the order of 20  $\mu\text{m}$ .

Two-fiber MEAs were applied to quantitatively study the “cross-talk” between adjacent electrodes. The steady-state voltammetric response from both experiments and numerical simulations shows that the normalized limiting current depends largely on the normalized inter-electrode distance,  $d/a$ , and, it increases rapidly when  $d/a$  is between 2 and 5, and almost reaches unity when  $d/a$  is larger than 5. Steady-state and fast-scan voltammetric responses demonstrate that the MEAs have well-defined electrochemical behavior and that each microelectrode can be individually addressed. Flow-cell characterizations show that these microdisk arrays are suitable for detecting transient chemical changes in confined spaces.

#### 5.5 Literature Cited

- (1) Kim, Y. T.; Scarnulis, D. M.; Ewing, A. G. *Anal. Chem.* **1986**, *58*, 1282.
- (2) Strein, T. G.; Ewing, A. G. *Anal. Chem.* **1992**, *64*, 1369.
- (3) Clark, R. A.; Beyer Hietpas, P.; Ewing, A. G. *Anal. Chem.* **1997**, *69*, 259.
- (4) Clark, R. A.; Ewing, A. G.; *Anal. Chem.* **1998**, *70*, 1119.
- (5) Meyerhoff, J. B.; Ewing, M. A.; Ewing, A. G. *Electroanalysis* **1999**, *11*, 308.
- (6) Chen, T. K.; Lau, Y. Y.; Wong, D. K. Y.; Ewing, A. G. *Anal. Chem.* **1992**, *64*, 1264.
- (7) Lau, Y. Y.; Abe, T.; Ewing, A. G. *Anal. Chem.* **1992**, *64*, 1702.
- (8) Abe, T.; Lau, Y. Y.; Ewing, A. G. *Anal. Chem.* **1992**, *64*, 2149.
- (9) Ewing, A. G.; Strein, T. G.; Lau, Y. Y. *Acc. Chem. Res.* **1992**, *25*, 440.

- (10) Chen, T. K.; Luo, G.; Ewing, A. G. *Anal. Chem.* **1994**, *66*, 3031.
- (11) Chen, G.; Gavin, P. F.; Luo, G.; Ewing, A. G. *J. Neurosci.* **1995**, *15*, 7747.
- (12) Zerby, S. E.; Ewing, A. G. *Brain Res.* **1996**, *712*, 1.
- (13) Colliver, T. L.; Hess, E. J.; Ewing, A. G. *J. Neurosci. Methd.* **2001**, *105*, 95.
- (14) Sombers, L. A.; Hanchar, H. J.; Colliver, T. L.; Wittenberg, N.; Cans, A. –S.; Arbault, S.; Amatore, C.; Ewing, A. G. *J. Neurosci.* **2004**, *24*, 303.
- (15) Uchiyama, Y.; Maxson, M. M.; Sawada, T.; Nakano, A.; Ewing, A. G. *Brain Res.* **2007**, *1115*, 46.
- (16) Sombers, L. A.; Maxson, M. M.; Ewing, A. G. *Cell. Molec. Neurobio.* **2007**, *27*, 681.
- (17) Dias, A. F.; Dernick, G.; Valero, V.; Yong, M. G.; James, C. D.; Craighead, H. G.; Lindau, M. *Nanotechnology* **2002**, *13*, 285.
- (18) Hafez, I.; Kisler, K.; Berberian, K.; Dernick, G.; Valero, V.; Yong, M. G.; Craighead, H. G.; Lindau, M. *Proc. Natl. Acad. Sci. USA* **2005**, *102*, 13879.
- (19) Stefan, R. I.; Staden, J. F. V.; Aboul-Ensin, H. Y. *Crit. Rev. Anal. Chem.* **1999**, *29*, 133.
- (20) Droge, M. H.; Gross, G. W.; Hightower, M. G.; Czisny, L. E. *J. Neurosci.* **1986**, *6*, 1583.
- (21) Wilson, M. (2006) [*Multiple-Electrode Recordings of Neuronal Ensemble Activity*] In: *Visualizing Large-Scale Patterns of Activity in the Brain: Optical and Electrical Signals*. (Buzsaki G, ed) pp. [9-16]. Atlanta, GA: Society for Neuroscience.
- (22) Maher, M. P.; Pine, J.; Wright, J.; Tai, Y. C. *J. Neurosci. Meth.* **1999**, *87*, 45.
- (23) Suzuki, I.; Sugio, Y.; Jimbo, Y.; Yasuda, K. *Lab Chip* **2005**, *5*, 241.
- (24) Yeung, C. K.; Sommerhage, F.; Wrobel, G.; Offenhausser, A.; Chan, M.; Ingebrandt, S. *Anal. Bioanal. Chem.* **2007**, *387*, 2673.
- (25) Stett, A.; Egert, U.; Guenther, E.; Hofmann, F.; Meyer, T.; Nisch, W.; Haemmerle, H. *Anal. Bioanal. Chem.* **2003**, *377*, 486.
- (26) Licht, S.; Cammarata, V.; Wrighton, M. S. *Science* **1989**, *243*, 1176.
- (27) Cammarata, V.; Talham, D. R.; Crooks, R. M.; Wrighton, M. S. *J. Phys. Chem.* **1990**, *94*, 2680.
- (28) Gavin, P. F.; Ewing, A. G. *J. Am. Chem. Soc.* **1996**, *118*, 8932.
- (29) Gavin, P. F.; Ewing, A. G. *Anal. Chem.* **1997**, *69*, 3838.
- (30) Belmont-Hebert, C.; Tercier, M. L.; Buffle, J.; Fiaccabrino, C. C.; De Rooij, N. F.; Koudelka-Hep, M. *Anal. Chem.* **1998**, *70*, 2949.
- (31) Feeney, R.; Kounaves, S. P.; *Anal. Chem.* **2000**, *72*, 2222.
- (32) Wang, J.; Chen, Q. *Anal. Chem.* **1994**, *66*, 1007.
- (33) Niwa, O.; Xu, Y.; Halsall, H. B.; Heineman, W. R. *Anal. Chem.* **1993**, *65*, 1559.
- (34) Fan, Y.; Chen, X.; Trigg, A. D.; Tung, C. H.; Kong, J.; Gao, Z. *J. Am. Chem. Soc.* **2007**, *129*, 5437.
- (35) Lanyon, Y. H.; Arrigan, D. W. M. *Sens. Actuators, B* **2007**, *121*, 341.
- (36) Sandison, M. E.; Cooper, J. M. *Lab Chip* **2006**, *6*, 1020.
- (37) Nolan, M. A.; Kounaves, S. P. *Anal. Chem.* **1999**, *71*, 3567.
- (38) Feeney, R.; Kounaves, S. P. *Electroanalysis* **2000**, *12*, 677.
- (39) Nagale, M. P.; Fritsch, I. *Anal. Chem.* **1998**, *70*, 2902.
- (40) Nagale, M. P.; Fritsch, I. *Anal. Chem.* **1998**, *70*, 2908.

- (41) Sandison, M. E.; Anicet, N.; Glidle, A.; Cooper, J. M. *Anal. Chem.* **2002**, *74*, 5717.
- (42) Li, J.; Ng, H. T.; Cassell, A.; Fan, W.; Chen, H.; Ye, Q.; Koehne, J.; Han, J.; Meyyappan, M. *Nano Lett.* **2003**, *3*, 597.
- (43) Sreenivas, G.; Ang, S. S.; Fritsch, I.; Brown, W. D.; Greg, A. G.; Woodward, D. J. *Anal. Chem.* **1996**, *68*, 1858.
- (44) Wang, K.; Fishman, H. A.; Dai, H. J.; Harris, J. S. *Nano Lett.* **2006**, *6*, 2043.
- (45) Li, X.; Zhou, Y.; Sutherland, T. C.; Baker, B.; Lee, J. S.; Kraatz, H. B. *Anal. Chem.* **2005**, *77*, 5766.
- (46) Zoski, C. G.; Yang, N.; He, P.; Berdondini, L.; Koudelka-Hep, M. *Anal. Chem.* **2007**, *79*, 1474.
- (47) Zoski, C. G.; Simjee, N.; Guenat, O.; Koudelka-Hep, M. *Anal. Chem.* **2004**, *76*, 62.
- (48) Menon, V. P.; Martin, C. R. *Anal. Chem.* **1995**, *67*, 1920.
- (49) Ugo, P.; Moretto, L. M.; Bellomi, S.; Menon, V. P.; Martin, C. R. *Anal. Chem.* **1996**, *68*, 4160.
- (50) Martin, C. R. *Science* **1994**, *266*, 1961.
- (51) Cepak, V. M.; Hulteen, J. C.; Che, G.; Jirage, K. B.; Lakshmi, B. B.; Fisher, E. R.; Martin, C. R.; Yoneyhama, H. *Chem. Mater.* **1997**, *9*, 1065.
- (52) Krishnamoorthy, K.; Zoski, C. G. *Anal. Chem.* **2005**, *77*, 5068.
- (53) Merritt, C. D.; Justus, B. L. *Chem. Mater.* **2003**, *15*, 2520.
- (54) Szunerits, S.; Walt, D. R. *Anal. Chem.* **2002**, *74*, 1718.
- (55) Baker, W. S.; Crooks, R. M. *J. Phys. Chem. B* **1998**, *102*, 10041.
- (56) Crooks, R. M.; Ricco, A. J. *Acc. Chem. Res.* **1998**, *31*, 219.
- (57) He, H. X.; Li, Q. G.; Zhou, Z. Y.; Zhang, H.; Li, S. F. Y.; Liu, Z. F. *Langmuir* **2000**, *16*, 9683.
- (58) Cheng, W.; Dong, S.; Wang, E. *Anal. Chem.* **2002**, *74*, 3599.
- (59) Dressman, S. F.; Peters, J. L.; Michael, A. C. *J. Neurosci. Methd.* **2002**, *119*, 75.
- (60) Sandison, M. E.; Anicet, N.; Glidle, A.; Cooper, J. M. *Anal. Chem.* **2002**, *74*, 5717.
- (61) Lee, H. J.; Beriet, C.; Ferrigno, R.; Girault, H. H. *J. Electroanal. Chem.* **2001**, *502*, 138.
- (62) Beriet, C.; Ferrigno, R.; Girault, H. H. *J. Electroanal. Chem.* **2000**, *486*, 56.
- (63) Morf, W. E. *Anal. Chim. Acta* **1996**, *330*, 139.
- (64) Morf, W. E. *Anal. Chim. Acta* **1997**, *341*, 121.
- (65) Morf, W. E.; Rooij, N. F. *Sensors Actuators B* **1997**, *44*, 538.
- (66) Harper, C. A., Ed. *Handbook of Ceramics Glasses, and Diamonds*; McGraw-Hill: New York, **2001**.
- (67) Saito, Y. *Rev. Polarog. (Japan)* **1968**, *15*, 177.
- (68) Miao, W.; Ding, Z.; Bard, A. J. *J. Phys. Chem. B* **2002**, *106*, 1392.
- (69) Bard, A. J.; Faulkner, L. R. *Electrochemical Methods*. 2<sup>nd</sup> ed. John Wiley & Sons: New York, **2001**.
- (70) Szabo, A. *J. Phys. Chem.* **1987**, *91*, 3108-3111.
- (71) The distance that the redox molecule diffuses,  $\delta = (2Dt_{\text{expt}})^{0.5}$ , at the time of the voltammetric experiment ( $t_{\text{expt}} = RT/vF$ ), is  $\sim 0.3$

## Chapter 6

### Modeling Membrane Disruption by Pyridinium Polymers in Artificial Lipid Vesicle Systems

#### 6.1 Introduction

It is well known that the antibacterial activity of pyridinium polymers is closely linked to polymer structure. These amphiphilic polycations also believed to kill bacteria by disrupting their lipid membranes.<sup>1</sup> Several factors such as the amount of positive charge, degree of hydrophobicity, structure of the pendant alkyl tail and the charge/tail spatial positioning determine whether the amphiphilic polycation can kill a cell by membrane disruption.<sup>2,3,4</sup> Therefore understanding the process of membrane disruption is important in designing more powerful antimicrobial polymers. Additionally, understanding lipid membrane-polycation interactions may have implications in interesting phenomenon like transmembrane delivery of material such as DNA, RNA, or drugs.

The length of the alkyl tail on the pyridinium unit of the polymer determines the antibacterial potency of the polymer. Pyridinium polymers with medium sized tails (3-6 carbons) are more potent than polymers with shorter (1-2 carbons) and longer (8-16 carbons) alkyl chains.<sup>4</sup> The reason for this effect is not completely understood, although it has been suggested that an optimum tail length must be used in conjunction with a positive charge, supplied by nitrogen or phosphorus, to disrupt the lipid membrane.<sup>2</sup> Hence, it would be interesting to study the effect pyridinium polymers containing different length alkyl tails would have on lipid membranes in a tightly controlled artificial model systems.

Artificial lipid vesicles consisting of lipid bilayer membranes are suitable model systems to study membrane interactions with biologically relevant species like polymers, proteins and drugs. Lipid vesicles have been widely studied and their size, shape, and lipid composition can be tightly regulated.<sup>5,6</sup> Artificial vesicles have a well-defined outer lipid membrane that can be tailored to mimic the cell membrane of a variety of biological cells.

A number of methods have been used to investigate membrane disruption by polycations in artificial model systems consisting of small and large lipid vesicles. Some of these methods include monitoring polymer induced fluorescent leakage;<sup>7,8</sup> observing phase transitions of lipid-polymer interactions by differential scanning calorimetry;<sup>9</sup> studying polycation induced hole formation by atomic force microscopy;<sup>10</sup> and examining membrane-polymer interaction by optical microscopy.<sup>11,12</sup>

In this chapter, I describe a real-time optical method to study lipid membrane disruption in model systems consisting of giant unilamellar vesicles (GUV) by cationic polymers. GUVs act as effective cell membrane mimics, and have been used by other researchers in mimicking exocytosis of neurotransmitter release.<sup>14</sup> A series of different water-soluble pyridinium polymers were administered near the model GUV and the effect on the morphology of the vesicle was optically observed in real time. The effect of polymer structure on GUV membrane disruption was compared to the observed antibacterial properties exhibited towards gram-negative *E. coli*. This work was done as a collaborative project with Dr. Aysuman Sen's research group in the Department of Chemistry at Penn State.

## 6.2 Materials and Methods

### 6.2.1 Materials and Instrumentation

Polyvinylpyridine (MW, 60,000 and 160,000 Da), was purchased from Aldrich. Iodomethane, 1-iodoethane (99+%), 1-iodopropane (99+%), 1-iodobutane (99+%) and 1-iodopentane (99+%) were purchased from Aldrich and used as received. Methanol and nitromethane (both ACS grade) were purchased from Acros Organics. Bacterial growth media and agar were purchased from Difco. Phospholipids were purchased from Avanti Polar Lipids.  $^1\text{H}$  and  $^{13}\text{C}$  NMR spectra were recorded on a Bruker DPX-300 or Bruker CDPX-360. An Olympus IX-70 inverted microscope equipped with a Sony DXC-C33 ExwaveHAD 3CCD video camera was used for vesicle visualization. An Eppendorf femtojet was used for injecting various solutions into the GUV.

### 6.2.2 Synthesis of Pyridinium Polymers

Various pyridinium polymers were synthesized by heating ~ 1g of poly (4-vinylpyridine) in 10 mL nitromethane with excess of the alkyl iodide at 65 °C for 24 h. The polymer was isolated by precipitation in diethyl ether and was dried under vacuum for 3 days. The degree of N-alkylation was determined using  $^1\text{H}$  NMR peak integration ratios. Polymers were purified by dialyzing in water/methanol for 3 days. Polymers were finally freeze dried and were tested for antibacterial and vesicle disruption activity. A representative  $^1\text{H}$  NMR spectrum of  $\text{C}_3$  polymers is given in (Figure 6.1) below.

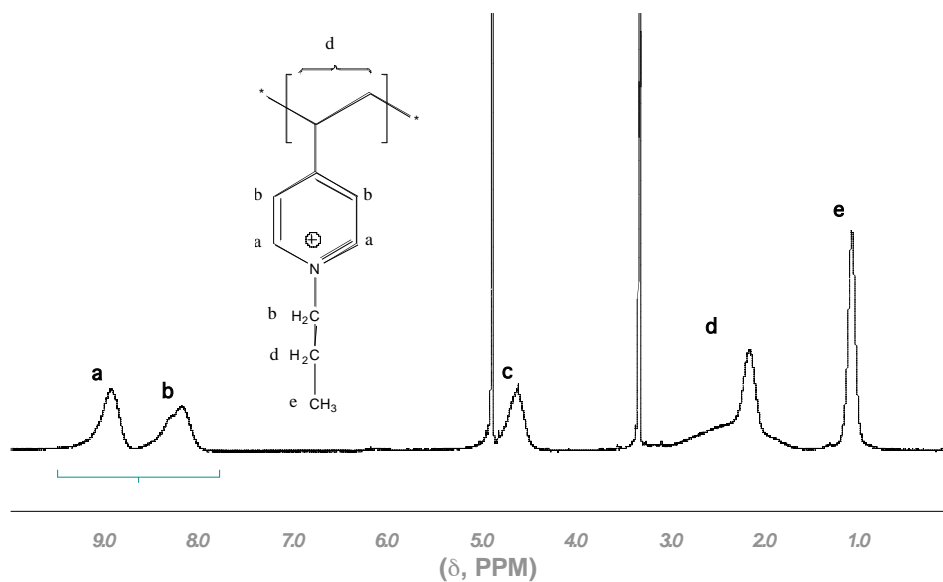


**Figure 6.1**  $^1\text{H}$  NMR spectrum (300 MHz,  $\text{MeOH-d}_4$ , ppm) of  $\text{C}_3$  polymer. Data collected by Varun Sambhy

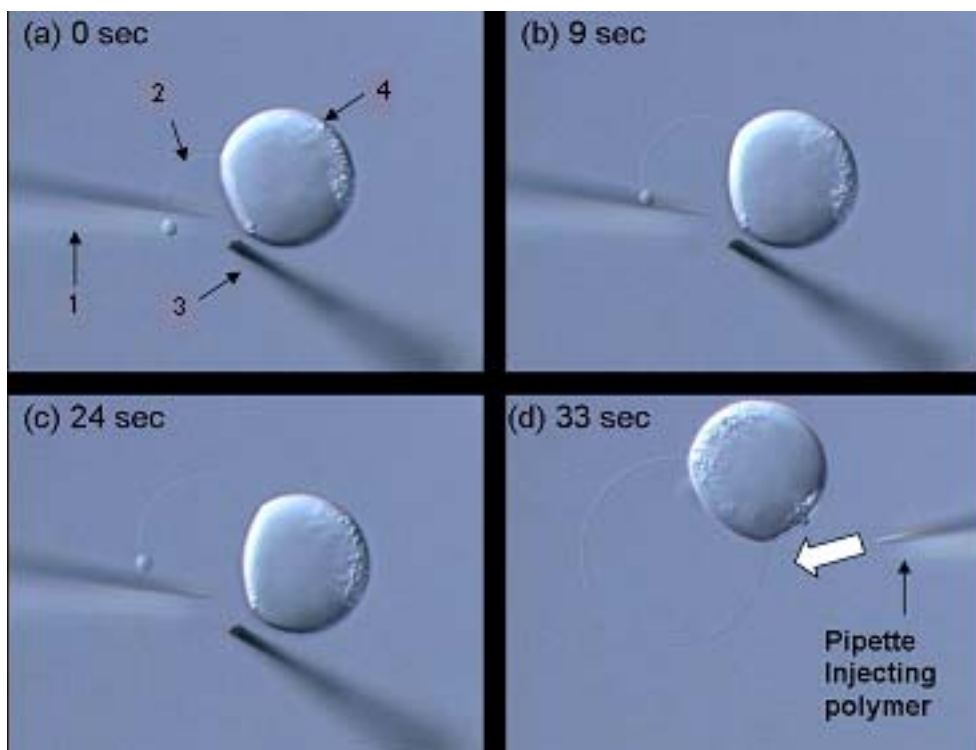
### 6.2.3 Preparation of Surface Bound Liposomes and Polymer Injection

Surface immobilized GUVs were prepared using a 75-25 wt% mixture of soy polar extract and *E. coli* polar lipid extract. Liposomes were created using a dehydration/rehydration process in phosphate buffer (pH 7.4).<sup>13,14</sup> GUVs bud out from dense multilamellar lipid vesicles, which are affixed to the surface of the glass slide. These dense multilamellar lipid vesicles also act as lipid reservoirs, allowing for the inflation of vesicles with buffer solution by providing lipid molecules needed for membrane expansion.

Surface immobilized GUVs are easily manipulated as to allow for inflation and polymer injection. An electroporation/inflation technique<sup>13</sup> was used to inflate the GUVs to the required size. In the electroporation / inflation technique, a glass micropipette with an electrical contact and a carbon fiber counter electrode are used in conjunction to

transiently disrupt the GUV membrane and allow for easy penetration of the glass pipette into the vesicle. Upon penetration, the GUVs are inflated with buffer solution injected into the vesicle via the glass pipette connected to an Eppendorf femtojet. (Figure 6.2) Upon completion of inflation, the glass pipette and the carbon counter electrode are withdrawn.

A second glass micropipette containing a polymer solution was then placed approximately 40 microns away from the liposome. A second femtojet was used to inject the polymer solution (~ 12 nanoliters) near the GUV membrane (5 s injection at 1500 hPa). The changes in membrane morphology were then monitored for 120 s. If after 120 s the liposome was intact, another polymer injection was applied, and the results were monitored for an additional two min. The process was repeated until the liposome ruptured or 10 min had elapsed.



Frame size =  $240 \times 180 \mu\text{m}$ .

**Figure 6.2** Setup for GUV formation by electroporation/inflation technique. A glass micropipette (labeled 1 in (A)) is used to penetrate and inflate the GUV (2) with buffer solution. A carbon fiber counter-electrode (3) completes the circuit. The attached multilamellar lipid vesicle (4) serves as a reservoir for supplying lipid molecules needed for GUV membrane expansion. (A) Start of inflation. (B) and (C) GUV being inflated to the required size, and (D) Setup ready for polymer injection by a second glass micropipette.

#### 6.2.4 Antibacterial Testing

*Escherichia coli* DH5- $\alpha$  (Clontech) were grown at  $37^\circ\text{C}$  and maintained on LB plates (Luria-Bertani broth, Lennox modification, with 1.5% agar). The relation between absorbance at 590 nm ( $\text{OD}_{590}$ ) and colony forming units (CFU) per mL was determined using the plate count method. Polymer stock solutions were prepared in 80% methanol-20% water to a concentration of 1 mg/300  $\mu\text{L}$ . Calculated volumes (30-250  $\mu\text{L}$ ) of polymer solutions were then pipetted into 15mL Falcon tubes. Methanol was evaporated

to yield solid polymer. *E. coli* suspension ( $5 \times 10^5$  CFU/mL) in LB broth was then added to each tube containing various polymers at concentrations of 100-2500  $\mu\text{g/mL}$ . A negative control contained only inoculated broth. The tubes were incubated at 37 °C with shaking at 250 rpm for 18-20 h. The visual turbidity of the tubes was noted both before and after incubation. Turbidity after incubation indicated bacterial growth. Aliquots (100  $\mu\text{L}$ ) from tubes, including those that showed no turbidity (little or no cell growth) were plated on LB agar plates to distinguish between bacteriostatic or bactericidal effects. These plates were incubated at 37 °C for 16-20 h and colonies were counted.

## 6.3 Results and Discussion

### 6.3.1 Synthesis of Pyridinium Polymer Library

Four pyridinium polymers poly(4-vinyl-N-alkylpyridinium iodide) polymers with methyl, ethyl, propyl and butyl alkyl tails were prepared as shown in Figure 6.3. Poly (4-vinylpyridine) (MW, 60,000 Da) was heated with excess of the respective 1-iodoalkane to N-alkylate all the nitrogens. This yielded a library of different pyridinium polymers: C<sub>1</sub>, C<sub>2</sub>, C<sub>3</sub> and C<sub>4</sub> differing only in the length of the pendant alkyl tail. The polymers were characterized by <sup>1</sup>H and <sup>13</sup>C NMR, which indicated complete N- alkylation with the respective alkyl iodide. Polymers were purified by dialyzing in water/methanol for 3 days, and were finally freeze dried before being tested for antibacterial and vesicle disruption activity.

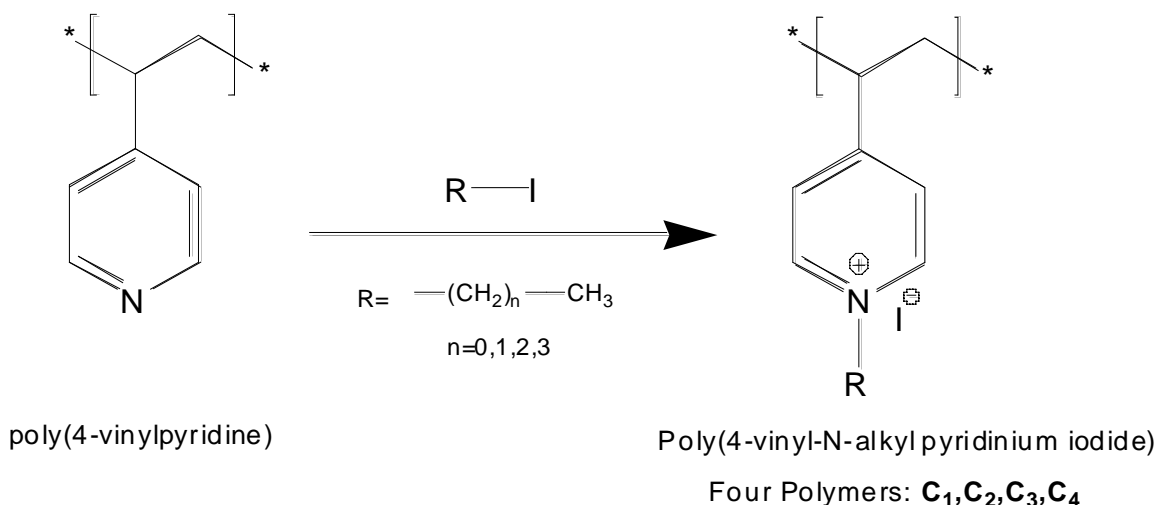


**Figure 6.3** Synthesis of poly (4-vinyl-N-alkylpyridinium iodide) polymers with different tail lengths.

### 6.3.2 Antibacterial Activity of Pyridinium Polymers

The antibacterial activity of the polymers towards gram negative *E. coli* was evaluated using the minimum inhibitory concentration (MIC) method. The antibacterial activity (Table 6.1) increased (lower MIC values) as the alkyl tail length increased from 1 carbon to 4 carbons i.e.  $C_1 > C_2 > C_3 > C_4$ . This trend was expected as it is known that pyridinium polymers with medium sized tails ( $C_3$  to  $C_5$ ) are more potent than polymers with smaller sized tails ( $C_1$  and  $C_2$ ).<sup>2</sup> With the antibacterial activity trend established, it was then decided to study the activity of these polymers in disrupting artificial lipid membrane systems. Initially I expected the vesicle disruption results to mirror antibacterial activity results, i.e. finding that polymer  $C_4$  would disrupt membrane faster producing rupture times for  $C_4 < C_3 < C_2 < C_1$ .

**Table 6.1** Antibacterial activity (MIC values) of the synthesized pyridinium polymers towards *E. coli*. *BS* designates that the samples prevented bacterial growth (bacteriostatic), but did not kill the cells.

Polymer	MIC value ( $\mu\text{g/mL}$ )
C <sub>1</sub>	1300 <sup>BS</sup>
C <sub>2</sub>	1000 <sup>BS</sup>
C <sub>3</sub>	200
C <sub>4</sub>	100

Data collected by Varun Sambhy

### 6.3.3 GUV Formation and Polymer Injection Protocol

Various polymer solutions (0.0021M) were prepared in phosphate buffer (pH 7.4). The polymer testing protocol is schematically depicted in Figure 6.4 below. In the first step, surface immobilized GUVs were formed in phosphate buffer (pH 7.4) and were inflated with to a constant size of  $\sim 40\text{-}60\ \mu\text{m}$  for each test. Then an Eppendorf femtojet attached to a micropipette was used to inject various polymer solutions near the GUV membrane. Identical volumes of different polymer solutions ( $\sim 12$  nanoliters) were injected at approximately the same distance ( $\sim 30\text{-}40\ \mu\text{m}$ ) away from the vesicle membrane. After injection, the vesicle morphology and membrane integrity were observed in real time by differential interference contrast imaging (DIC). A CCD video camera attached to the microscope was used to record real time videos of the experiments.

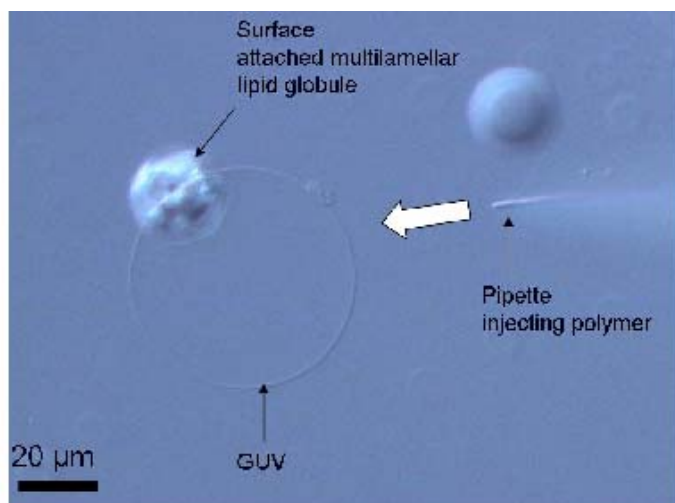


**Figure 6.4** Schematic of direct real-time observation of membrane-polymer interaction in giant unilamellar vesicles (GUVs).

### 6.3.4 Effect of Tail Length on the Time of Vesicle Rupture

Solutions of different pyridinium polymers were injected near the GUV membrane and morphological changes in the vesicle structure were recorded and analyzed. Each polymer was tested 5 times to ensure reproducibility. The time of the first injection of the polymer (each injection approximately ~ 12 nanoliters) was recorded as  $t=0$ . Following polymer injection, distinct morphological changes in the membrane structure were observed; including formation of polymer-lipid agglomerates, membrane folding and eventual GUV rupture. The time after the first injection at which the vesicle ruptured was recorded as  $t_r$ . Comparing rupture times gives a qualitative idea of the polymer's ability to disrupt the vesicle membrane. Depending on the polymer being tested, it took up to 3-4 injections each to obtain complete vesicle rupture.

Since the vesicle size, distance from the injecting micropipette, volume, and injected polymer solution concentrations were similar, any difference in morphological

changes in membrane structure should be attributed to the structure of the polymer, for example the length of alkyl tail. The ability of different polymers to cause GUV rupture was observed to be:  $C_1 > C_2 > C_3 > C_4$ . Surprisingly, this result was completely opposite to the observed antibacterial activity towards, *E. coli*,  $C_4 > C_3 > C_2 > C_1$ . The average rupture time ( $t_r$ ), and the number of injections required by a particular polymer to cause complete GUV rupture are given in Table 6.2.

**Table 6.2** Average GUV rupture time ( $t_r$ ), and the number of injections needed to completely disrupt the vesicle.

<b>Polymer</b>	<b>Average <math>t_r</math> (s)</b>	<b>Standard deviation <math>n = 5</math></b>	<b>Average number of polymer injections needed to rupture GUV</b>
<b>C<sub>1</sub></b>	14.04	5.07	1
<b>C<sub>2</sub></b>	23.90	15.56	1
<b>C<sub>3</sub></b>	126.47	57.22	2.1
<b>C<sub>4</sub></b>	153.95	48.33	2.3

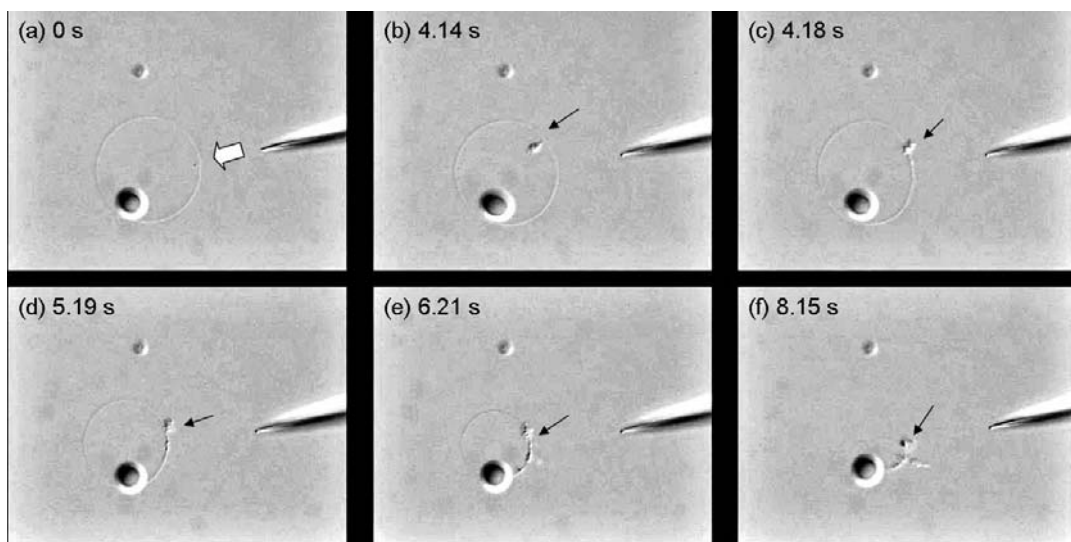
As shown in Table 6.2,  $t_r$  and the number of injections required to rupture the vesicle increased as the tail length increased from 1 to 4 carbons. Short tail polymers, ( $C_1$  and  $C_2$ ) were most effective in disrupting the vesicle membrane, requiring only one injection to produce complete membrane disruption. Longer tail polymers like  $C_3$  and  $C_4$  took subsequent injections and more time to completely rupture the vesicle.

No membrane disruption or any visible morphological changes were observed with multiple injections of 0.1 M solution of the corresponding small molecules i.e. N-methylpyridinium iodide, N-ethylpyridinium iodide, etc (data not shown). Multiple injections of other negative controls like uncharged polymers (0.1M polyethyleneglycol or 0.1M polyvinylimidazole), or an anionic polymer (0.1M sodium polyacrylate) also failed to have any visible effect on the GUVs (data not shown). No effect on the GUV structure was observed after multiple injections of 0.3M KBr, clearly ruling out osmotic

imbalance as a cause for vesicle rupture (data not shown). Therefore membrane disruption is clearly due to the polycationic species itself and is not an artifact of other processes.

### **6.3.5 Morphological Changes in GUV Membrane Structure**

When  $C_1$  polymer solution was injected in vicinity of the vesicle, rapid rupture of the GUV was observed within 8.15 s as shown in Figure 6.5. As soon as the polymer solution was injected, I observed movement in the lipid bilayer leading to an agglomerate formation on the surface of the membrane. Polycations like poly-L-lysine are known to induce lipid domain formation in GUV by binding with the anionic lipids in the membrane.<sup>11</sup> Hence these agglomerates probably consisted of polymer-lipid complexes formed due to electrostatic binding between the polycation and the negatively-charged lipid molecules. The removal of lipid molecules from the bilayer structure by the polycation resulted in the destabilization of the membrane, which ultimately lead to vesicle rupture. I also observed a general migration of lipids from the multilamellar lipid globule to the GUV, indicating that some compensation of the lost lipids was occurring.

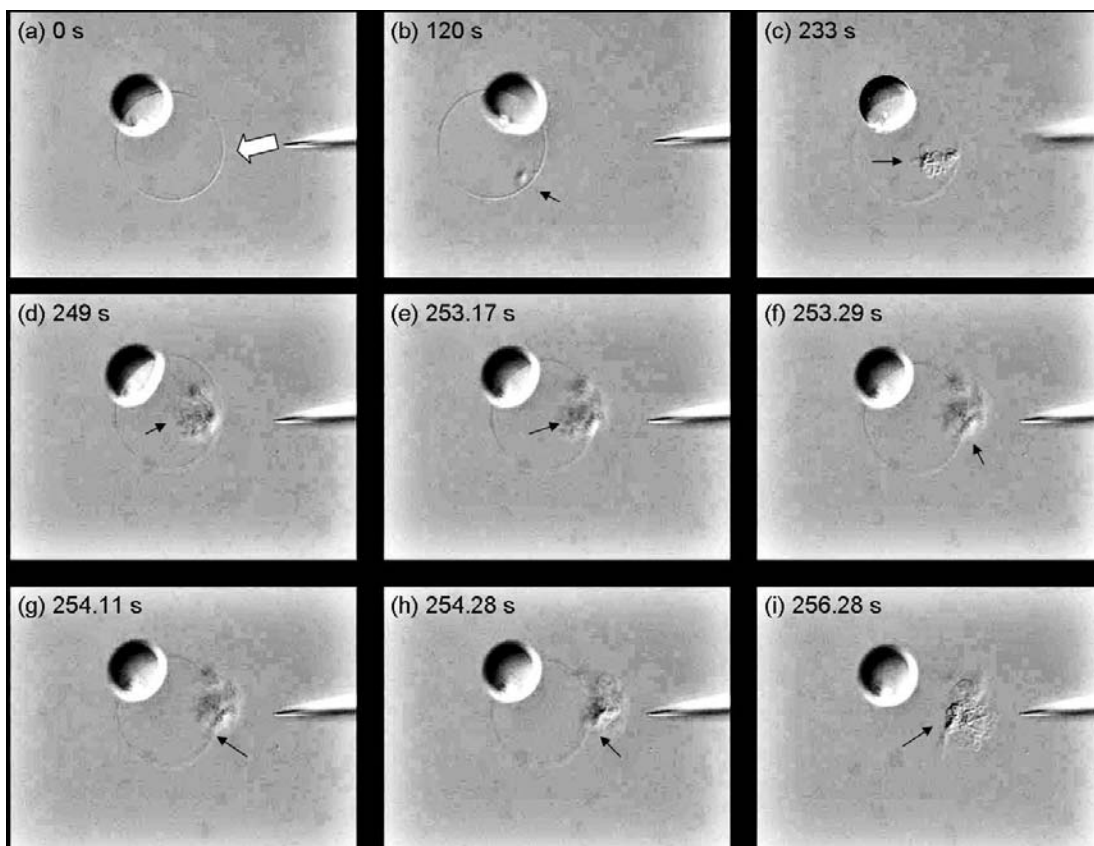


Frame size =  $240 \times 180 \mu\text{m}$ .

**Figure 6.5** Differential interference contrast (DIC) snapshots of video recording of GUV membrane disruption by  $C_1$  polymer. Fast vesicle bursting was observed with just 1 injection of polymer. (A) polymer injected at 0 s, (B) and (C) polymer-lipid agglomerations seen on the surface of the GUV membrane, (D) and (E) shrinkage of the diameter of the GUV membrane with concomitant increase in the size of agglomeration, and (F) GUV finally ruptures after 8 s.

As mentioned earlier, as the length of the alkyl tail on the pyridinium polymer is increased ( $C_3$  and  $C_4$ ), the time required to disrupt the membrane also increased (Table 6.2). With the  $C_3$  polymer the vesicle took nearly nine times longer to burst. Upon injection of  $C_3$ , dense agglomerations formed on the GUV membrane. These polymer-lipid agglomerations eventually moved into the vesicle (Figure 6.6). After more injections of  $C_3$  polymer, the size of these agglomerations increased, and the vesicle eventually ruptured after releasing the agglomerations. An interesting observation made was that the vesicle always broke from the inside rather than collapsing. Since the polymer was being applied to the outside of the liposome, it seems natural that the lipid would fold inward but instead the liposome would burst outward. Another important difference between the short tail polymers  $C_1$  and  $C_2$ , and longer tail  $C_3$  and  $C_4$  polymers was that the lipid polymer agglomerations formed by long tail polymers could span the

transmembrane boundary. Lipid-polymer aggregates ( $C_3$  and  $C_4$ ) formed initially on the surface of the membrane and then gradually moved into the vesicle (Figure 6.6). After additional polymer injections, these aggregates spanned the transmembrane boundary once again, moving outwards and being released right before vesicle rupture.



Frame size =  $240 \times 180 \mu\text{m}$ .

**Figure 6.6** Differential interference contrast (DIC) snapshots of video recording of GUV membrane disruption by  $C_3$  polymer. (A) Polymer injected at 0 s, (B) small lipid-polymer agglomerations observed on the vesicle surface right before the second polymer injection, (C) agglomerations increased in size after the second injection and moved inside the GUV (D) and (E) agglomerations further increased in size after the third polymer injection at 240 s. Agglomerations are clearly inside the vesicle, (F) and (G) agglomerations move from inside the vesicle to the outside by spanning the vesicle membrane boundary, (H) agglomerations are mostly on the *outer* surface of the membrane, and (I) vesicle ruptures finally after 3 polymer injections and 256 s.

Other interesting morphological changes in the membrane were also observed with long tail polymers. With the  $C_3$  polymer, the agglomerations that formed had

morphology similar to that of tangled ropes (Figure 6.7). These agglomerations, which were probably made up of polymer-lipid complexes, were completely inside the vesicle boundary indicating they could cross the lipid membrane. I then decided to test the effect of increasing the tail length beyond four carbons to examine the ability of the polymer to enter the liposome. Pyridinium polymer with pentyl tails ( $C_5$ ) was synthesized. Solution of  $C_5$  polymer was injected onto the vesicle membrane and the changes in membrane morphology were recorded. Interestingly, with  $C_5$  polymer, the GUV did not rupture at all even after 4 polymer injections. The firm and spherically shaped membrane appeared to fold and distort after coming in contact with the polymer (Figure 6.7). Also, no transmembrane migration of the polymer-lipid agglomerates was observed. I also hypothesize that as the tail size increases; hydrophobicity of the polymer also increases. This causes the polymer to intercalate into the bilayer because the hydrophobic tails of  $C_5$  polymer mesh with/into the inner hydrophobic leaflet of the lipid bilayer. This intercalation causes an expansion in the bilayer resulting in the fold and distortion seen in Figure 6.7. The GUV exposed to  $C_5$  was filled with an inert dye, Fast Green FCF, to visualize any leakage due to defects in the membrane. Very little leakage of dye from within the GUV was seen, indicating the  $C_5$  polymer intercalated into the bilayer efficiently without forming any large defects or holes.

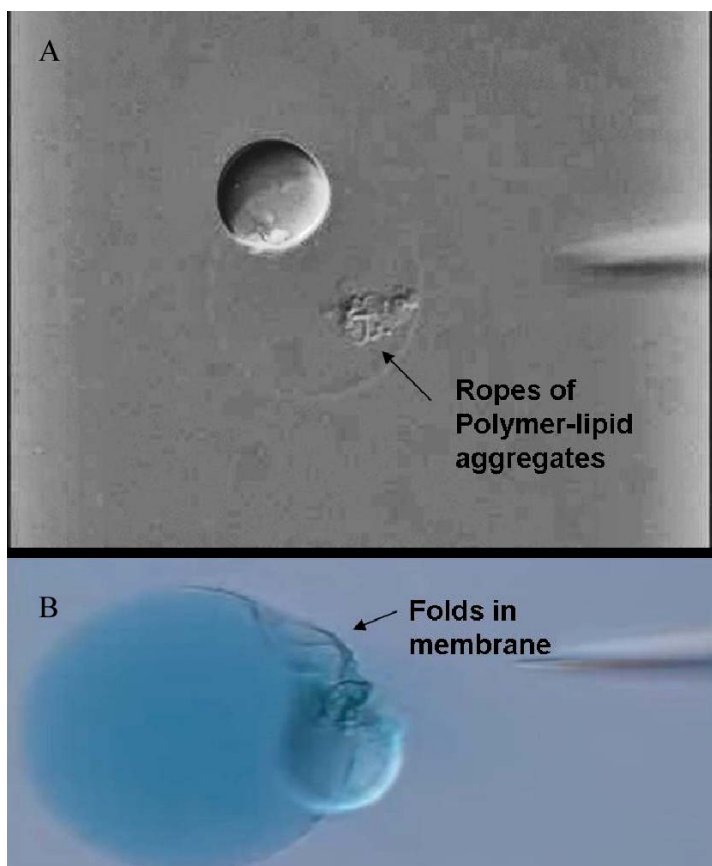


**Figure 6.7** Different morphological changes observed in the vesicle membrane structure after injection of the longer tail  $C_3$  (A) and  $C_5$  (B) polymer. (A) Tangled rope like polymer-lipid aggregates seen inside the vesicle after injection of  $C_3$  polymer, and (B) folding of the membrane structure was observed after injection of  $C_5$  polymer. No vesicle bursting or dye leakage was observed for  $C_5$  polymer.

Important differences in the ability of the polymers to mediate transmembrane permeation of the polymer-lipid aggregates were observed with direct visualization of liposomes. Use of cationic pyridinium polymers with very small tails ( $C_1$  and  $C_2$ ) causes vesicles to rupture so fast that only a little visible transmembrane permeation of the polymer-lipid aggregates can be visualized. With pyridinium polymers with a longer tail ( $C_5$ ), the polymer-lipid aggregates remained on the surface and did not move inside the vesicle. The increased hydrophobicity of the  $C_5$  polymer led to the intercalation of the amphiphilic polymer in the lipid bilayer. Only the medium tail polymer  $C_3$  affected unambiguous transmembrane permeation of the polymer-lipid aggregates. This

transmembrane migration of polymers and molecules could have application in DNA transfection and drug delivery.<sup>15</sup> A major problem with delivery agents, however, is that they generally kill the target cell. The data presented here may help guide the design of polymers and molecules which are able to migrate across the membrane without causing such damaging effects.

### 6.3.6 Effect of Polymer Molecular Weight on Vesicle Rupture

The effect of polymer molecular weight on its ability to disrupt the vesicle membrane was also studied. C<sub>1</sub> and C<sub>3</sub> polymers having a higher molecular weight (increasing from 60,000 to 160,000 Da) were synthesized by starting with poly(4-vinylpyridine). Polymers were purified as described previously and were injected near the GUV. It was observed that higher molecular weight polymers took slightly longer times as compared to lower molecular weight polymers to completely rupture the GUV membrane (Table 6.3). A possible explanation may involve the slower diffusion rate of the much larger polymer molecules as they move to the lipid membrane surface. The difference in membrane disruption time, however, was not very pronounced and was not statistically significant. This result was not unexpected because it has been reported that antibacterial activity of amphiphilic polymers remains constant over a broad range of molecular weights.<sup>8,16</sup>

**Table 6.3** Average GUV rupture time  $t_r$  of higher molecular weight polymers. The standard error of the mean is reported for each polymer type.  $n = 3$ .

Molecular Weight	Average vesicle rupture time $t_r$ (s)	
	C <sub>1</sub>	C <sub>3</sub>
60,000 Da	14.04 ± 5.07	126.47 ± 57.22
160,000 Da	27.68 ± 19.79	198.85 ± 54.85

### 6.3.7 Effect of Intra-Vesicular Polyanion on Vesicle Rupture

To investigate the observed difference in the antibacterial activity and the membrane disrupting activity of the pyridinium polymers, I carried out a series of membrane disrupting experiments with GUV inflated and filled with a polyanion sodium polyacrylate (PAA). It was hypothesized that a presence of negatively charged macromolecules like DNA, RNA or proteins both inside cells and within the extracellular medium affects how a polycation binds to and disrupts the lipid membrane. Polyanions might bind to short tail pyridinium polymers ( $C_1$ ) more strongly than the longer tail polymers ( $C_3$ ), due to steric effects of the pendant alkyl tail. Hence, the presence of these polycation-polyanion interactions should decrease the membrane disrupting activity of the short tail polymers more than that of the long tail polymer.

Polyanion filled GUVs were formed by inflating the liposome with a 0.03 M solution of PAA in phosphate buffer (pH 7.4). Polymer solutions  $C_1$  and  $C_3$  (0.0021M) were then injected near the GUV membrane and polymer-membrane interaction was observed. A total of 3 polymer injections of 12 nanoliters each were needed to completely disrupt the vesicles. The average rupture time, needed to rupture polyanion and buffer filled vesicles is given in Table 6.4.

**Table 6.4** Average GUV rupture time  $t_r$  for  $C_1$  and  $C_3$  polymers towards GUV filled with buffer and anionic polyacrylic acid. The standard deviations are reported in parenthesis.  $n = 3$

Polymer	Average vesicle rupture time $t_r$ (s)	
	Buffer	PAA
$C_1$	$14 \pm 5$	$327 \pm 80$
$C_3$	$127 \pm 57$	$371 \pm 122$

As hypothesized, the presence of negatively charged polyanion inside the GUV dramatically increased the time and the amount of polymer needed to disrupt the vesicle. It took 3 injections of polymer solution to completely disrupt the vesicle. Moreover, this effect was much more pronounced for short tail  $C_1$  polymer, than for longer tail  $C_3$  polymer.  $C_1$  took a 23 times longer to disrupt GUVs filled with PAA than GUVs filled with only buffer. On the other hand,  $C_3$  took only three times as long to disrupt PAA filled vesicles than buffer filled vesicles. A reason for the observed difference in antibacterial activity and membrane disrupting activity could be the deactivation of short tail polymers by polyanions present in the cells and medium. In the GUV model, the addition of PAA increased the number of negatively charged ions available to interact with the polymer solution. When the polymer causes a rupture in the liposome wall, it is plausible that the PAA rushes out of the hole and passivates the positive charge on the polymer, thus reducing its efficacy.

## 6.4 Conclusions

A novel method to study the fundamental aspects of interaction between polycations and lipid membranes in artificial membrane model systems was developed. Real time observation of changes in membrane morphology upon polymer exposure were recorded and analyzed. Interesting morphological changes like agglomerate formations, rope like morphologies and transmembrane migration of aggregates were observed. Contrary to the hypothesis based on antibacterial activity, it was observed that pyridinium polymers with shorter alkyl tails ( $C_1$  and  $C_2$ ) were more effective in disrupting the model lipid membrane than polymers with longer alkyl tails ( $C_3$ ,  $C_4$ , and  $C_5$ ). Therefore, it

seems that factors other than membrane disruption are involved in determining how effective a polymer is in killing bacteria under physiological conditions. This method may help in understanding what structural difference is crucial to allowing a polymer migrate across the lipid membrane and not destroy it, thus aiding in the design of polymers able to facilitate transmembrane delivery of biologically relevant species such as drugs, DNA, RNA and proteins.

### 6.5 Literature Cited

- (1) Tashiro, T. *Macromol. Mater. Eng.* **2001**, 286, 63.
- (2) Lewis, K., Klibanov, A. M. *Trends Biotechnol.* **2005** 23(7), 343-348.
- (3) Lin, J., Qiu, S., Lewis, K., Klibanov, A. *Biotechnol. Prog.* **2002**, 18, 1082-1086.
- (4) Tiller, J. C.; Liao, C. J.; Lewis, K.; Klibanov, A. M. *Proc. Natl. Acad. Sci. USA* **2001**, 98, 5981-5985.
- (5) Busquets, M. A.; Alsina, M. Asuncion; Haro, I. *Current Drug Targets* **2003**, 4, 633.
- (6) Tsogas, I.; Tsiourvas, D.; Nounesis, G.; Paleos, C. M. *Langmuir* **2006**, 22, 11322-11328.
- (7) Hara, M., Miyake, M., Iijima, S., Yang, Q., Arai, T., Yuan, H., Miyake, J. *Supramolecular Science* 1998, 5, 777-781.
- (8) Ilker, M. F.; Nüsslein, K.; Tew, G. N.; Coughlin, B. E. *J. Am. Chem. Soc.* **2004**, 126, 15870-15875.
- (9) Kawakami, K., Nishihara, Y., Hirano, K. *J. Phys. Chem. B* **2001**, 105, 2374-285.
- (10) Mecke, A.; Srinivas, U.; Sassanella, T. M.; Lee, D-K.; Ramamoorthy, A.; Baker, J. R. Jr.; Orr, B. G.; Holl, M. M. B. *Chem. Phy. Lipids.* **2004**, 132, 3-14.
- (11) Menger, F. M.; Seredyuk, V. A.; Kitaeva, M. V.; Yaroslavov, A. M.; Melik-Nubarov, N. S. *J. Am. Chem. Soc.* **2003**, 125, 2846-2847.
- (12) Hristova, N. I.; Angelova, M. I.; Tsoneva, I.; *Bioelectrochemistry* **2002**, 58(1), 65-73.
- (13) Cans A. S., Wittenberg, N., Karlsson, R., Sombers, L., Karlsson, M., Orwar, O., Ewing, A. *Proc. Natl. Acad. Sci. USA* **2003**, 100, 400-404.
- (14) Cans A. S., Wittenberg, N., Eves, D., Karlsson, R., Karlsson, A., Orwar, O., Ewing, A. *Anal Chem* **2003**, 75, 4168-4175.
- (15) Li, W.; Nicol, F.; Szoka, F. C. *Advanced Drug Delivery Reviews* **2004**, 56, 967
- (16) Ikeda, I., Hirayama, H., Yamaguchi, H., Tazuke, S., Watanabe, M. *Antimicrob. Agents Chemother.* **1986**, 30, 132.

## **Chapter 7**

### **Future Directions of Modeling Exocytosis**

#### **7.1 Introduction**

This dissertation has explored the physical restraints of the lipids involved in exocytosis. Due to the complex nature of exocytosis, it is important to identify the contributions of each component part. The research outlined in this dissertation has characterized a liposome model of exocytosis, both the measurement of release and the physical restraints of the system, and shown how this system can be manipulated to give information pertinent to changes that occur in lipid membranes. Also a new electrode array was designed and assembled to increase the amount of information gained from monitoring individual release events in exocytosis. Also a novel model for monitoring membrane disruption by antibacterial polymers was devised and tested to study the effect of polymer tail length on a membrane. These advances in understanding membrane dynamics can be used to further elucidate the role of lipids in exocytosis. With the liposome model of exocytosis as a basis, it is possible to study the individual components and how they interact with one another. Simplifying the system will help to clarify the role that each component part has on the overall system. The following are some ways to clarify how the liposome model of exocytosis can explain how these component parts interact.

## 7.2 Free Fusion

In the artificial model of exocytosis a glass pipette delivers the electroactive agent into the liposome before it fuses. The flow of solution out of the pipette exerts pressure onto the liposome and thus affects the relative speed of release of material from the liposome. By removing the pipette from the liposome and allowing the lipid to release its contents it would be possible to determine how much of an effect the pipette has on release dynamics.

In order to pursue this dimension of analysis, it became important to find a way to remove the pipette from the liposome. One method I devised was to apply a short electrical pulse to the pipette tip to coax the liposome off of the pipette. A problem with this method was that the application of the pulse registered in the electrical recording and sometimes masked the signal produced from the oxidation of catechol during release. A second problem was that once the liposome was released the trajectory of release was never constant. Some times the liposome would release its contents to the left or right of the electrode, thus effectively reducing the efficacy of detecting release. Some preliminary results were gathered and showed little correlation in the release characteristics for the control and free fusion (Figure 7.1). If another method of removing the glass pipette from the liposome could be devised it would be possible to determine the effect of the fluid flow has on the overall release kinetics in the exocytosis system. This would allow a better understanding of the forces involved in the artificial model and help to compare the results with that found in cells.

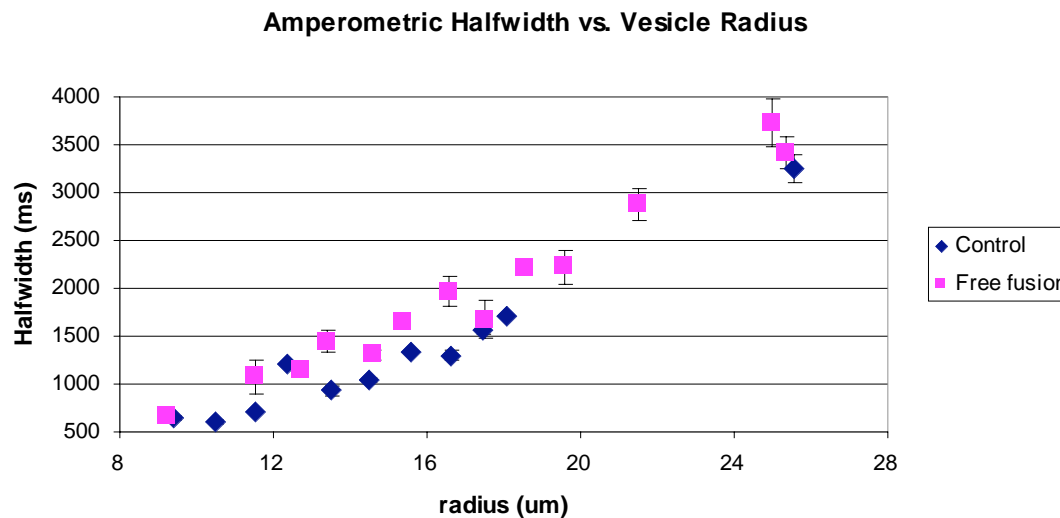


**Figure 7.1** A graph showing vesicle radius versus halfwidth of the amperometric spikes for artificial exocytosis with the pipette removed from the inner vesicle. As vesicle size increases so does the time required for full release of catechol. Error bars show standard error of the mean.

### 7.3 Cholesterol

The addition of cholesterol to soy polar extract would further change the membrane in the liposome model of exocytosis. Specifically, incorporation of cholesterol would increase rigidity of the membrane and slow catechol release from the liposome.<sup>1,2</sup> Release from the liposome should change based upon total cholesterol, or in other words as the cholesterol increases so does the time for full release. Also with addition of cholesterol, the possibility of microdomain formation increases. The overall homogeneity of the lipid sample would decrease with an increase in cholesterol due to the microdomains selectively sequestering lipids and spawn regions of increase rigidity.

Ultimately, the liposome model offers a unique opportunity to isolate the effect of cholesterol on a purely lipidic model of the latter stages of exocytosis.

Once cholesterol is incorporated into the liposome, it would be interesting to see what effect a cholesterol specific agent, like methyl- $\beta$ -cyclodextrin, would do to the release characteristics of the liposome model. Cyclodextrin selectively chelates cholesterol and removes it from the membrane.<sup>3-5</sup> Removal of cholesterol by application of cyclodextrin would also make it possible to devise protocols to compare the same liposome a reduce some of the variability in data analysis.

#### **7.4 Protein Additives**

The relative simplicity of the liposome model of exocytosis should allow exploration of the role that lipids play in the expelling of electroactive material from a vesicle. With such a stripped down model of exocytosis, changes in membrane composition have been examined but in our attempts to molecularly understand exocytosis it would also be beneficial to examine how membrane properties change in the presence of specific proteins. For initial experiments, it will be important to choose a protein with an ability to recruit specific lipids so that a local change in membrane composition may be ascertained.

Towards this goal, it would be interesting to look at how annexin II would change the membrane properties of the liposome model. Annexin II selectively binds cholesterol and would cause the cholesterol in a liposome to aggregate around the protein thus effectively removing some of the cholesterol from the rest of the membrane.<sup>6,7</sup> In doing preparation work for this study it would be important to also consider what effects

physiological concentrations of  $\text{Ca}^{2+}$  would have on the liposome system as  $\text{Ca}^{2+}$  increases the binding affinity of annexin II.<sup>7</sup> This experiment would be dependent on the results from the previous section as any effects from annexin II on cholesterol would need to be compared to how cholesterol alone affects catechol release as a control. It would be interesting to see if annexin II would be able to restore rate of release to the cholesterol free situation if cholesterol slows it down as predicted.

Another protein of interest would be dynamin. This protein has been linked to the pinching off of vesicles in the process of endocytosis.<sup>8</sup> The use of this protein is different from that of membrane bound proteins, dynamin binds to the lipid neck of an endocytosing vesicle, oligamerizes and wraps around it to pinch off the lipid neck. A temperature sensitive dynamin (shibire) could be used in the liposome model of exocytosis to monitor the formation of dynamin by its ability to pinch off the lipid nanotube (Figure 7.2). Injecting a solution of dynamin inside the vesicle at  $29^{\circ}\text{C}$  and then using a pipette to form a liposome inside the vesicle would be one approach to this experiment. Dynamin at  $29^{\circ}\text{C}$  would be in the solution between the inner and outer vesicle in the model. The overall solution could then be cooled and the release from the liposome would be predicted to stop at a temperature when dynamin begins to oligomerize. Due to the sensitive nature of electrochemical measurements it might even be possible to measure the diameter of the liposome as the dynamin pinches it off.

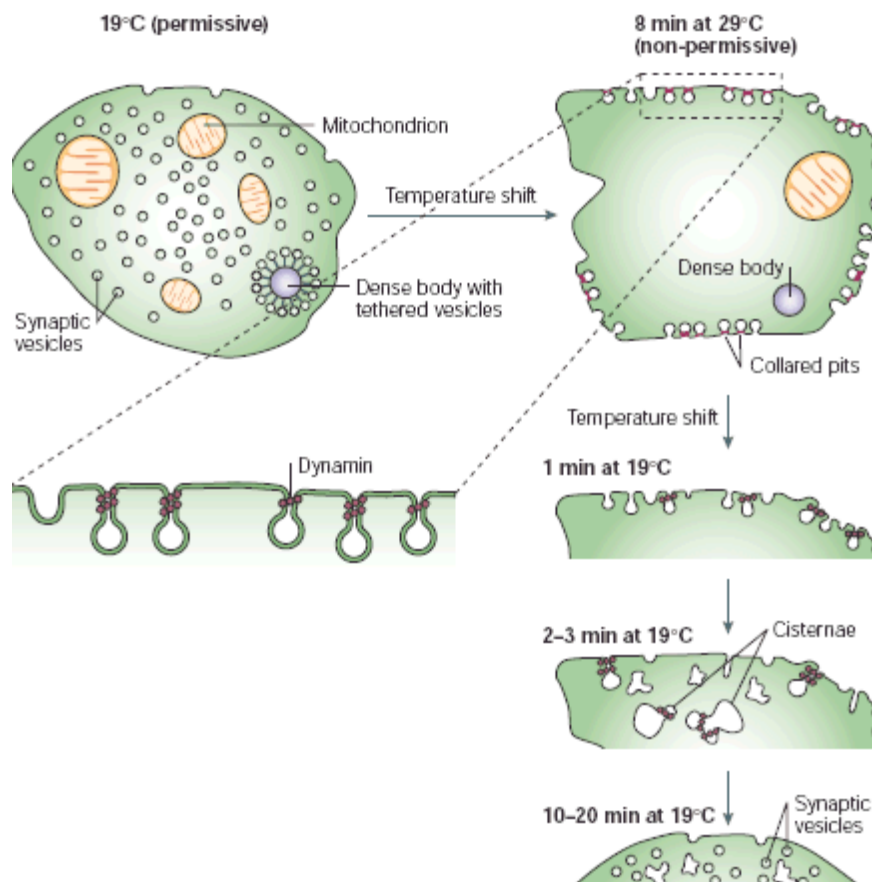


**Figure 7.2** Schematic of Shibire form of dynamin. At higher temperatures 29°C dynamin is inactivated but when the temperature is reduced then dynamin is active and can resume pinching off endocytosis vesicles. (Adapted from reference 8)

### 7.5 Changing Acyl Chain Composition

As noted in the previous work of chapter 3 of this dissertation, changes in the headgroup composition of liposomes had a great effect upon the release characteristics exhibited in exocytosis. In a follow-up experiment to that study, it would be beneficial to ascertain what changes in release dynamics would be generated by a change in the relative tail group concentrations of the liposome. I have carried out some preliminary experiments in this area and have been able to show a change in lipid acyl chain composition also has an effect on the membrane properties. Using the same tail groups

that are present in the soy polar extract, namely the eighteen carbon acyl chains, it was shown that adding 25% of a specific tail group lipid was sufficient to show a difference. Phosphatidylcholine was chosen as the headgroup for this study because commercially available reagents provide the widest variety of acyl chains for PC. Acyl Chains with eighteen carbons in the chain were examined because they were the most abundant acyl chains in soy polar extract. In Figure 7.3 the two acyl chains compared are the 18:1 (DOPC) and 18:2 (DLPC). At small vesicle radii, enrichment with DLPC shows an interesting trend towards events having a larger halfwidth than events for vesicles enriched with DOPC but this appears to not be so clear for events from vesicles of larger radius. The variance in the data is large and thus no definite trends are apparent for the larger vesicle sizes with DLPC or DOPC enriched vesicles. The results are nevertheless encouraging that with the right experimental design the effect of tail group on the kinetics of release might be observed.

## Tail Group Analysis

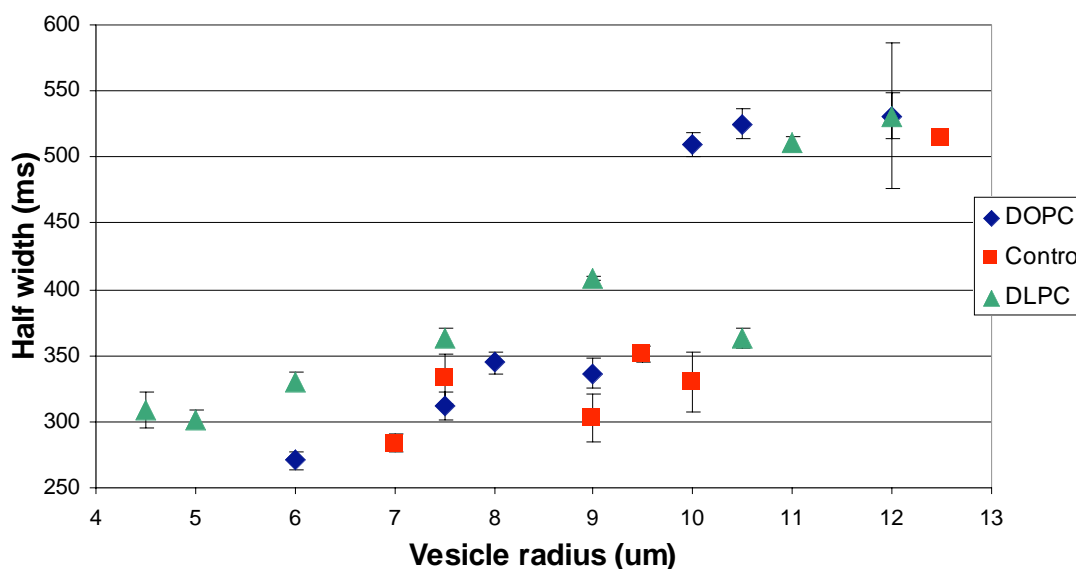


**Figure 7.3** Analysis of two tail group additives compared with soy polar extract. A slight difference in the two tail groups is visible but variance of the data makes it hard to see a clear trend. The head group on each of these acyl chains is PC.

## 7.6 Conclusion

The liposome model of exocytosis offers a unique avenue to examine the role that lipids play in exocytosis. The ability to add small changes to the system is very appealing as it allow for observation of how these components can affect the process of exocytosis. Once the basic physical parameters of the system have been quantified the liposome model will allow direct comparison to cellular systems and can be used to determine possible mechanisms for a lipids role in exocytosis. By further studying these avenues the long-term goal is to use this system to help us better understand the molecular mechanism of exocytosis, what controls and regulates the process, and thus neuronal communication.

## 7.7 Literature Cited

- (1) Edidin, M. *Current Opinion in Structural Biology* 1997, 7, 528.
- (2) Stottrup, B. L.; Stevens, D. S.; Keller, S. L. *Biophys. J.* 2005, 88, 269-276.
- (3) Bacia, K.; Scherfeld, D.; Kahya, N.; Schwille, P. *Biophys. J.* 2004, 87, 1034-1043.
- (4) Chintagari, N. R.; Jin, N.; Wang, P.; Narasaraju, T. A.; Chen, J.; Liu, L. *Am. J. Respir. Cell Mol. Biol.* 2006, 34, 677-687.
- (5) Hatzi, P.; Mourtas, S.; G. Klepetsanis, P.; Antimisiaris, S. G. *International Journal of Pharmaceutics* 2007, 333, 167.
- (6) Ayala-Sanmartin, J. *Biochemical and Biophysical Research Communications* 2001, 283, 72.
- (7) Ayala-Sanmartin, J.; Henry, J.-P.; Pradel, L.-A. *Biochimica et Biophysica Acta (BBA) - Biomembranes* 2001, 1510, 18.
- (8) Praefcke, G. J. K.; McMahon, H. T. *Nature Reviews Molecular Cell Biology* 2004, 5, 133.

## Vita

Daniel J. Eves

### Education

Ph.D. Chemistry The Pennsylvania State University December 2007

B.S. Chemistry Southern Utah University May 2001

### Awards

Department Travel Award 2005

Benjamin C. Morrell Memorial Endowment Scholarship 1999 – 2000

Qwest Physical Science Departmental Scholarship 2000 – 2001

### Publications

***Variation in Lipid Headgroup Concentration Alters Catechol Release in a Liposome Model of Exocytosis*** Daniel J. Eves, Edward T. Phillip and Andrew G. Ewing in preparation.

***Electrochemistry at the Cell Membrane/Solution Interface***, N. Wittenberg, M. Maxson, D. Eves, A.-S. Cans, A.G. Ewing, in *Electrochemical Methods for Neuroscience*, A.M. Michael and L.M. Borland, Eds., in press.

***Electrochemistry inside and outside of single cells*** Eves, D.; Ewing, A. in *Ultrasensitive Analysis of Biomolecules and Single Living Cells*, Xiaochong Nancy Xu Ed., in press.

***Amperometric Detection of Exocytosis in an Artificial Synapse*** Cans, A.-S.; Wittenberg, N.; Eves, D.; Karlsson, R.; Karlsson, A.; Orwar, O.; Ewing, A.; *Anal. Chem.*; **2003**; 75(16); 4168-4175